UNIVERSITA' DEGLI STUDI DI PAVIA
Dottorato di Ricerca in Bioingegneria e Bioinformatica
Dipartimento di Ingegneria Industriale e dell'Informazione

Diffusion tensor imaging: study of white matter connection and advanced MRI sequence development.

Tutor: Prof. Giovanni Magenes
PhD Program Chair: Prof. Riccardo Bellazzi

PhD Thesis by
Andrea De Rinaldis

Abstract

Magnetic resonance imaging (MRI) is an imaging technique able to produce high quality images of the human body without ionizing radiation. Over years, MRI has been constantly improved, and advanced MRI techniques able to investigate structure and physiology of the human body have been developed. In particular, diffusion MRI is an advanced technique, which, sensing water molecules movement and its direction, provides quantitative information about microstructural properties of fiber bundles in white matter (WM). All projects developed in this thesis were focused on diffusion MRI and consequently on the study of WM organization.

The first project was focused on investigating WM differences between healthy subjects, patients affected by Vascular Dementia (VaD) and Alzheimer disease (AD). Since VaD and AD neuropsychological profiles often overlap and anatomical changes do not always correlate with a specific type of dementia, differentiating between them results difficult. Therefore, in order to provide quantitative imaging biomarkers specifically sensitive to AD or VaD, a voxel wise analysis on the whole WM was performed on a total of 93 subjects (31 AD, 27 VaD and 35 healthy control). WM alteration patterns considered useful in distinguishing between VaD and AD emerged from the analysis. In particular, parahippocampal gyri and corpus callosum showed different anterior/posterior alteration patterns specific to pathology, while thalamic radiation impairment seemed to be characteristic of VaD, because these patients showed alterations in this area compared both to AD and HC but no alterations were found in AD. Altogether these findings revealed an impairment in WM bundles involved in cognition and in the cerebro-cerebellar connectivity.

In the second project, cerebro-cerebellar connectivity was studied with the aim of clarifying cerebellar involvement in cognition and describing cerebro-cerebellar loop structure. Advanced MRI tractography was used to reconstruct and quantitatively describe the cortico-ponto-cerebellar (CPC) pathway in human in vivo. From the analysis emerged that the CPC pathway is mainly involved in the connection of cognitive cerebral and cerebellar areas. Furthermore, in order to study the whole cerebro-cerebellar loop, which is composed of the CPC and the cerebello-thalamo-cortical (CTC) pathway, these results were compared with the ones already obtained in a previous study focused on CTC. Both pathways resulted to be interested in connecting cognitive areas. A difference in terms of cerebral areas reached by the two pathways suggests an asymmetry of the cerebro-cerebellar loop regarding cognitive tasks. Whereas findings during motor tasks suggest a symmetrical communication between the cerebrum and the cerebellum.

Even though results obtained from post processing of diffusion data revealed important information, DTI suffers from resolution issues due to the trade off between voxel size and SNR, with voxel dimension in the order of important details in the structure of the addressed WM bundles. Therefore, diffusion analysis would benefit from higher resolution data. Here, in order to partially resolve the resolution problem, a sequence able to acquire high-resolution images using non-coplanar radio frequency pulses, was developed. Data acquired with this sequence showed good signal-to-noise ratio values and an anatomically reliable reconstruction of color-coded maps of fractional anisotropy.

All these projects gave interesting information about WM structure, along with new advanced investigation tools. Further experiments where all the techniques, here applied separately, can be applied together, would be useful in order to improve results quality and perform new hypothesis about WM structure and properties.

Index

Introduction

Magnetic resonance imaging (MRI) is an imaging technique able to produce high-resolution images of the human body. Since magnetic resonance is modestly invasive, by the use of no ionizing radiation, and allows to produce images from almost all body regions, it has become an important tool of radiology. Over years, MRI potential has been continuously improved, giving to this technique an important role not only in clinical applications but also in research. Despite all MRI applications and improvements, there are still many unresolved questions about brain structure and physiology. It is therefore necessary to perform new studies and to improve acquisition techniques in order to move further MR technology and brain knowledge.

In this thesis, diffusion MRI was used to study white matter (WM) connectivity and properties, with particular attention to cerebro-cerebellar connectivity. Diffusion MRI is based on water molecular movement and provides structural information about WM architecture. Its main applications are structural reconstruction of WM bundles and quantitative investigation of WM properties in terms of diffusion derived parameters.

All projects described in this thesis were born in junction between the Department of Electrical, Computer and Biomedical Engineering (University of Pavia, Pavia) and the Brain Connectivity Center (C. Mondino National Neurological Institute, Pavia). In particular, the project described in chapter five was carried out at the Max Planck Institute (Tubingen, Germany) during a 7 months period as visiting PhD student.

The first project described in this thesis concerns the study of the whole WM in terms of diffusion derived parameters. This investigation was performed with the aim of finding differences in the WM between healthy controls, patients affected by Vascular Dementia (VaD) and Alzheimer's disease (AD). Since their neuropsychological profiles often overlap and anatomical changes do not always correlate with a specific type of dementia, quantitative biomarkers specifically sensitive to VaD or AD would be desirable.

In the successive chapter, is described a tractographic reconstruction and a quantitative description, of a pathway (cortico-ponto-cerebellar) connecting the cerebral cortex with the cerebellum. The pathway reconstruction was accomplished by using two advanced diffusion techniques: constraint spherical deconvolution and track-density imaging. The former is useful to model multiple fiber populations within a voxel and to resolve the decussation of trans-

hemispheric connections, while the latter provides super-resolution maps useful to place seed and target regions of interest. The aim of this reconstruction is to clarify cerebellar involvement in cognition and to verify if cerebro-cerebellar ”communication” involves serial processing steps between multiple cerebral cortical modules before information is sent back to the cerebellum via the cortico-ponto-cerebellar pathway.

Even if post processing methods are useful tools to perform analysis and provide promising results, diffusion imaging suffers from resolution issues, due to the trade off between voxel size and SNR. Despite all post processing techniques that give the chance to improve resolution and perform detailed analyses, brain investigation would benefit from higher resolution acquisition. Even if it is impossible to reach resolution comparable with fiber dimensions with the actual technology, a sequence able to acquire diffusion data in a small field of view with a high resolution was developed in this thesis which partially solves the resolution problem.

This thesis is composed of six chapters:

Chapter 1 gives an overview about the basic principles of magnetic resonance. The main physics concepts that lay in the basis of magnetic resonance are explained. MRI sequences for basic image acquisition are described together with an overview of advanced MRI techniques.

Chapter 2 is focused on diffusion MRI. The difference between diffusion weighted imaging and diffusion tensor imaging is explained together with the different parameters that can be obtained with these techniques. Theory behind tractography is also described.

Chapter 3 reports the voxel wise analysis of the whole WM, performed in order to find differences, in terms of diffusion derived parameters, among AD, VaD patients and healthy subjects. WM bundles obtained from the analysis as altered by pathology are discussed in relationship with their utility in differentiating between dementia.

In chapter 4 is explained the tractographic reconstruction of the cortico-ponto-cerebellar pathway. The obtained results and hypotheses about cerebral and cerebellar areas connected by this pathway are discussed. An hypothesis about the reconstruction in humans in vivo of the whole cerebro-cerebellar loop is given at the end of the chapter.

In chapter 5 the theory and the development of the diffusion sequence able to acquire a reduced field of view with a higher resolution is described. Sequence performance is evaluated

in comparison with a sequence that reaches the same results using a different theory. Preliminary data acquired with a 9.4T scanner are reported at the end of the chapter.

In chapter 6 general conclusions about all the projects are drawn. The main findings of each study are summarized with attention to future applications. In particular it is highlighted how the projects separately described in this thesis, could find a common meeting point in future studies of both healthy and pathological subjects.

Chapter 1: Introduction to magnetic resonance

In this chapter a general overview about the basic principles of magnetic resonance is given. Due to the wide dimension of the topic, only the main information necessary to understand the studies explained in the following chapters is summarized. Anyway, for further explanations a complete list of references is reported at the end. In this chapter a brief description is reported covering the physics of magnetic resonance, the image acquisition principles and the basic and advanced sequences.

1.1 Opportunity in MRI

MRI is an imaging technique able to produce high-resolution images of various regions of the human body. The basis of MRI lay on nuclear magnetic resonance (NMR), a spectroscopic technique used to investigate microscopic molecules properties.

In 1946 magnetic resonance phenomenon was discovered by Felix Bloch and Edward Purcell independently. Later on, between 1950 and 1970, molecular analysis was performed using NMR. In 1975 Richard Ernst introduced the use of frequency encoding, and the Fourier Transform laying the basis of the current MRI techniques. In 1977 Peter Mansfield developed the echo planar imaging technique.

From that time MRI techniques have been constantly improved, reaching shorter acquisition time and higher resolution along with a wide range of contrasts. MRI has become one of the most important tool of radiology, thanks to its ability to produce medical images from almost all body regions and to its safety for the patients due to the use of no ionizing radiations.

Such important role of MRI has been reflected not only in clinical applications but also in research. Along with classical, also other advanced MRI techniques have been and still are developed. Therefore, MRI is now used not only for clinical scopes, but also for a wide range of research projects. There are indeed a lot of studies where MRI has been used to investigate brain morphology along with cognitive and functional implications of several brain diseases.

1.2 Physics of MRI

As explained above, the scope of this chapter is to give a general overview about main MRI concepts. Here only the main formulas and physics effects related to MRI are reported for the sake

of brevity. For an accurate explanation please refer to references (Kuperman, 2000; McRobbie *et al.*, 2007; Branca, 2008; Brown and Semelka, 2011; Hashemi *et al.*, 2012).

Proton is an electric charged mass rounding around its axis, such characteristic is represented by the spin angular moment:

$$P = h/2\pi\sqrt{I(I+1)}$$

where is the Planck constant (h = 6.626x10^{-34} J s) and I represents the possible state of the spin. The Hydrogen (H) proton has only two states of the spin (I = ± ½), consequently the H proton can round only on two directions.

Since proton is an electric charge in movement it has a magnetic dipole moment:

$$\mu = \gamma P$$

where ɣ is the gyromagnetic ratio (for H, ɣ = 42.58 MHz / T).

Without an external magnetic field each spin magnetic moment is randomly oriented. If placed in an external magnetic field of strength B_0, the spin vector of the particle will tend to align with or opposite to the direction of applied magnetic field. These two states are known as “spin up” and “spin down,” respectively. By absorbing energy a spin-up nuclei can transit to a spin down and a spin down nuclei can give up energy and transition to spin-up. The energy difference between these two states is:

$$\Delta E = \frac{h}{2\pi}\gamma B_0$$

The population distribution (spin up, spin down) in these two energy state is governed by thermal equilibrium described by the Boltzman distribution:

$$\frac{N_-}{N_+} = e^{-\Delta E/kT}$$

where N_+ represents the higher energy state (spin-down), N_- be the lower energy state (spin up), k is the Boltzmann’s constant (1.38e-23 J/K) and T the temperature.

Independently from his orientation each spin will precess around B_0 axis with a frequency of:

$$\omega = \gamma B_0$$

where ω is called Larmor frequency. Therefore if protons are placed in an external magnetic field they all precess at the same Larmor frequency.

In order to go ahead with MRI physics it is useful to move from a microscopic to a macroscopic scale. This means to consider not a single spin (proton) but a group of spins experiencing the same external magnetic field.

At any instant in time, the magnetic field due to the spins in each spin packet can be represented by a magnetization vector.

$$M = \frac{1}{V}\sum \mu_i$$

where V represents the volume.

If there is no external magnetic field the magnetization vector is equal to zero because each proton rounds in its own direction. Once B_0 is applied the net magnetization vector lies along B_0 direction (with an orientation given by N_-/N_+ proportion) and M ≠ 0. From this point onward this condition of magnetization is considered as the equilibrium (M_0).

Supposing that B_0 is applied along the Z axis, the Z component of M (M_Z) is maximum and equal to M_o. M_Z is referred as the longitudinal magnetization. In this condition, there are no components of M in the xy plane. It is possible to change the net magnetization direction by exposing the nuclear spin system to a radiofrequency (RF) magnetic field oscillating at the Larmor frequency.

$$B_1(t) = B_1 \cos(\omega t)$$

If the RF pulse (usually applied in the xy plane) is oscillating at the Larmor frequency for a sufficient time, the net magnetization will precess and lay completely to a perpendicular plane with respect to Z axis (fig. 1). At this point M_z = 0 while M_{XY} = M_o. M_{xy} is referred to as the transverse magnetization.

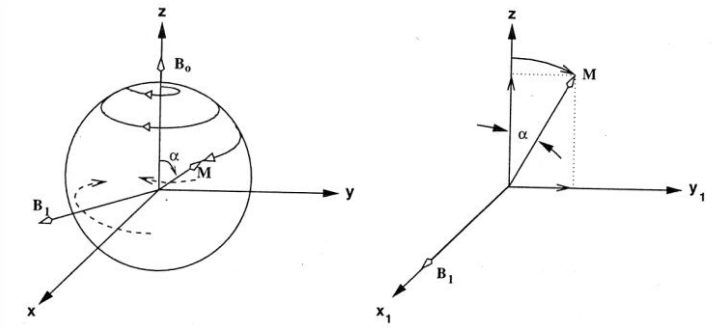

a b

Figure 1 Representation of the net magnetization precession from z to xy plane in a fixed reference system (a). Looking at the same phenomenon in a reference system rotating at Larmor frequency the net magnetization tilt from z to xy plane (b).

Considering to look the net magnetization movement in a plane rotating at the Larmor frequency, the net magnetization does not precess but just tilts from z axis to xy plane. The tilt angle is the amount of "movement" that the net magnetization experiences during the RF pulse. The tilt angle is also called flip angle and is given by:

$$\alpha = \gamma B_1 \tau$$

where B_1 is the strength of the RF field and τ is the pulse duration. Depending of the sequence (see paragraph 1.5 for sequence description) the flip angle can have different values. For the basic sequences α is usually equal to 90° or 180°, therefore the RF pulse is called 90°/180° RF pulse. Once the RF pulse is switched off, only B_0 affects protons. At this point, the net magnetization vector will come back to the equilibrium and M_z returns to be equal to M_0 and $M_{xy} = 0$.

Two time constants describe the net magnetization movement from the xy plane to the z axis(fig. 2). One describes how M_Z returns to equilibrium ($M_Z = M_0$). It is called the spin-lattice relaxation time (T_1).

$$M_z = M_0(1 - e^{-t/T_1})$$

The second time constant is called the spin-spin relaxation time (T_2) and describes the decay of the transverse magnetization.

$$M_{xy} = M_{xy}\, e^{-t/T_2}$$

The decay of the transverse magnetization is influenced by two factors:

1) interaction between spins
2) B_0 inhomogeneities

The combination of these two factors is what actually influence the decay of transverse magnetization and is represented as T_2^*. T_2^* is shorter than T_2.

$$\frac{1}{T_2^*} = \gamma \Delta B + \frac{1}{T_2}$$

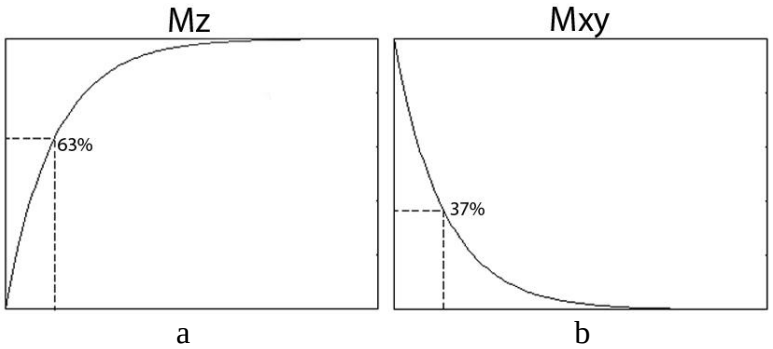

Figure 2 Mz return to the equilibrium (a) and M_{xy} decay (b). T1 represents the time necessary in order that Mz is equal to 63% of M_0 (a), T2 represents the time necessary in order that M_{xy} is equal 37% of M_0(b).

Summarizing, T_1 and T_2 describe the time necessary to M_Z to return to the equilibrium and for M_{XY} to decay respectively. Such values are dependent from the kind of tissue and, as will be later explained, are fundamental in order to obtain different contrasts in MRI.

1.3 From physics to signal

As for measurement system different from MR, the concept that lay at the basis of signal acquisition is to move a system from its equilibrium and to "see" how it returns to that status. In MRI, the RF pulse is applied in order to move the net magnetization from the equilibrium (M_z = M_0) and the signal is recorded while the net magnetization returns to the equilibrium (M_0 moves from xy plane to z axis). Consequently, the signal that is going to be recorded by a receiver coil is the one that the net magnetization produces in the xy plane. From now on, t_0 will be considered as the time when the RF pulse, applied for a time sufficient to have $M_{xy} = M_0$, is switched off. At t_0, M_{xy} is equal to M_0, then, depending on T_2, M_{xy} decays until reaching a null value. On the other hand, at t_0, M_z starts from zero and, depending on T_1, reaches the value of M_0.

The signal produced by M_{xy} is called free induction decay (FID) and is the basic signal in the MRI.

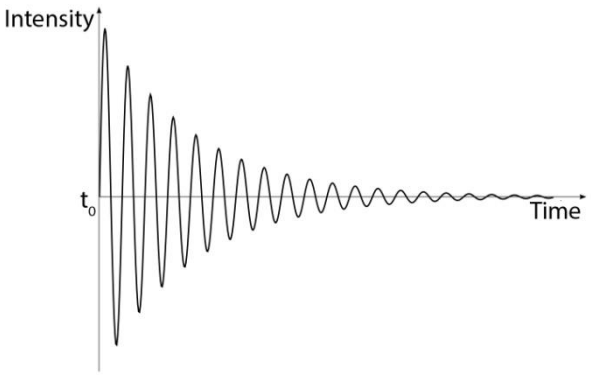

Figure 3FID signal. At t_0 M_{XY} is equal to M_0, then decays until to reach a zero value.

In only few milliseconds the amplitude of the signal decays exponentially to zero, such decay time is so short because protons coherence is influenced not only by spin interactions but also by B_0 inhomogeneities (T_2*). In order to take into account only dephasing effects, due to spin interaction and not to the influence of B_0 inhomogeneities, a 180° RF pulse is applied after the 90° one. A 180° RF pulse has the scope of rephasing spins and reversing static field inhomogeneities. Indeed, after the 90° RF pulse, at t_0 spins dephase and transverse magnetization decreases. By applying a 180° RF pulse, spins rephase in a opposite direction with respect to the previous one and transverse magnetization reappears by producing another signal, lower than FID, called echo. The echo time (TE) is considered as the time that goes from the 90° RF pulse and the highest peak of the echo. Since the 180° RF pulse reverses dephasing due to static field inhomogeneities but not the ones due to spin interactions, the signal loss is due to T_2. The signal envelope from the FID to echo maximum peaks corresponds to the T_2 decay curve (fig. 4).

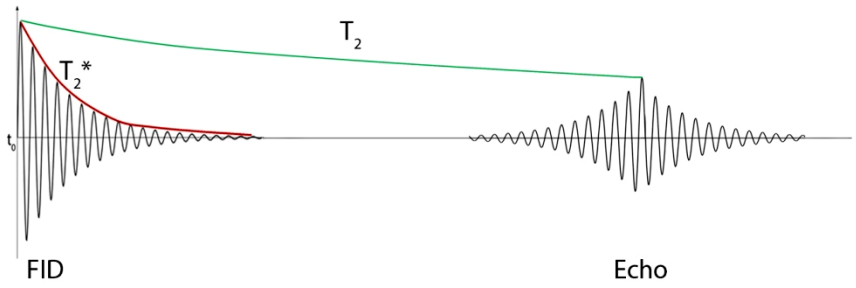

Figure 4FID and echo signal. The red line represents T_2*, while the green line represents T_2.

1.4 Image reconstruction

At this point, considering a human body immersed in a magnetic field B_0, to which is applied one or more RF pulses, the body net magnetization will move as described in the previous paragraphs and a signal from the whole body will be obtained. In this situation it is impossible to find out from which region the signal comes from. In order localize the region originating the signal, it is necessary to impose some features to the signal depending where it has been generated. In order to characterize the signal in function of its position, magnetic fields linearly variable in space (usually called gradients) are added to B_0. By applying these gradients along different directions (usually along x, y and z axis) is possible to obtain a spatial linear variation of the static field

strength in the z, x, y directions. Considering for example to apply a gradient along the z axis, the magnetic field will change linearly:

$$B_0(z) = B_0 + G_z\, z$$

where G_z is the intensity of the gradient (mT/m) and z represents the direction. Since the Larmor frequency depends on B_0, linearly changing B_0 intensity along one axis, will implicate a different Larmor frequency for each point of the axis. By using an RF pulse "centered" on the exact frequency it is possible to excite only spins rotating at that frequency. Applying the same concept to the x and y axis is possible to characterize each spins group with a frequency and phase dependent on its position and consequently to obtain a signal with a position dependent frequency and phase.

As explained in the next paragraph, in order to obtain an image from MR, the RF pulses and magnetic gradients are applied with different time combinations. As regards gradients, they are separately applied along three perpendicular axis (x, y and z). Usually the first gradient has the scope to excite the protons contained in a specific slice of the human body, while the other two gradients are necessary in order to characterize each "point" (voxel) of the slice with frequency and phase dependent on its position (fig. 5).

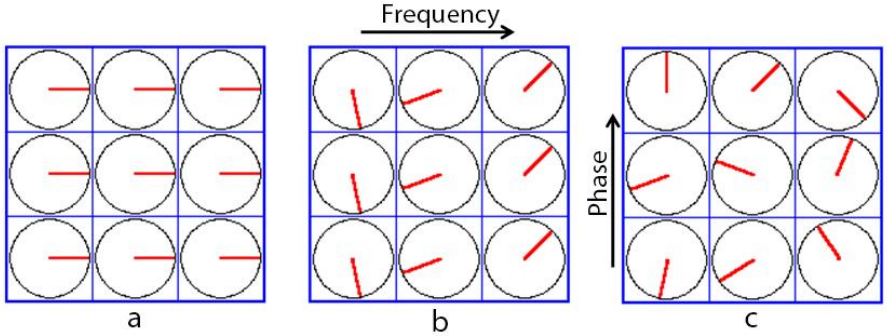

Figure 5 Effect of application of magnetic gradients. As the slice selection gradient is applied in one slice, all the vectors have the same phase and frequency (a). After the frequency encoding gradient application vectors will have a different frequency in the gradient direction (column in the figure) (b). After phase and frequency encoding gradients application, each vector will have its own phase and frequency (c).

At this point, considering that x, y and z magnetic gradients have been applied, the signal coming from each voxel in the excited slice has its own frequency and phase. Before "becoming" an image, the signal is acquired in a frequency space (K-space). The k-space has a dimension given by the number of lines and columns. Usually, the number of columns depends on the number of

frequency encoding samples, while the number of lines is equal to the times the phase encoding gradient is applied. In order to “move” from the space of frequencies to the one of the image it is necessary to apply an inverse Fourier transform. As already underlined, this chapter is only an overview about the basic concept of MRI and topics like k-space would need much more explanation in order to be fully understood. For further information about basic MRI principles it is possible to refer to the references reported at the beginning of the chapter.

1.5 Basic MRI sequences

An MRI sequence is a temporal series of RF magnetic pulses and magnetic gradients. The sequence is “guided” by two time variables: repetition time (TR) and TE. The former represents the time between two consecutive repetitions of the sequence (usually the time between two consecutive 90° RF pulses). The latter indicates the time between the 90° pulse and the echo formation. There are plenty of different sequences, each one characterized by different combinations of RF pulses and gradients, aimed at obtaining different image contrasts. Since it is strictly related with thesis projects, the spin echo sequence is here briefly reported.

The spin echo is a sequence characterized by two RF pulses and the signal is T_2 dependent, therefore M_{xy} decay is not influenced by B_0 inhomogeneities. Regarding to the sequence structure: a 90^o RF pulse is applied with a slice selection gradient (usually in the feet to head direction). After a time constant equal to TE/2 slice selection gradient is applied along with a 180^o RF pulse. Between the 90^o and 180^o pulses a gradient in the phase encoding direction is applied. The frequency encoding gradient is applied after the 180^o pulse during the echo acquisition. Since this part of the sequence is the one where the signal is acquired the frequency encoding gradient is also called the readout gradient. These gradients are usually applied along x, y and z axis, anyway the direction where each gradient can be applied is not fixed.

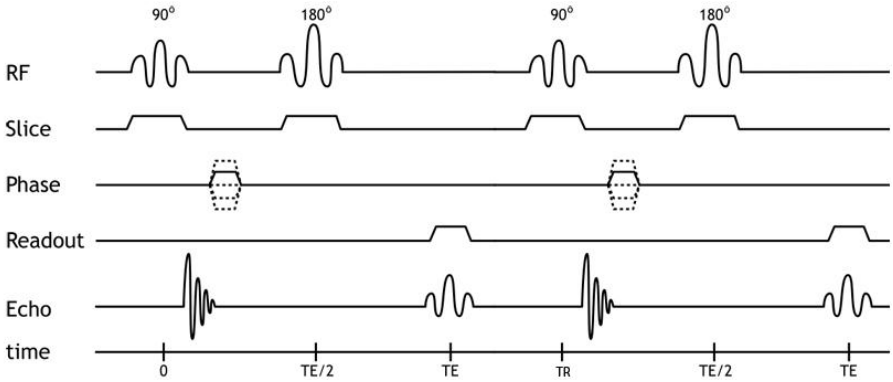

Figure 6 Schematic representation for a SE sequence. The phase encoding gradient is represented with multiple dotted lines to indicate that is repeated as many times as the number of k-space lines**.**

The signal from a spin echo sequence is as follow:

$$S = k\,\rho\left(1 - e^{-TR/T_1}\right)\left(e^{-TE/T_2}\right)$$

Considering the scheme reported in figure 6, in one TR only one eco is acquired; this means that in one TR only one line of the k-space is filled. The total acquisition time is equal to TR multiplied by the number of k-space lines and the number of slices. Such scheme requires a lot of time for each sequence. In order to have a shorter acquisition time, in the readout part of the sequence, it is common to use an acquisition technique called echo planar imaging (EPI). EPI is a readout technique able to acquire an entire slice in a TR. Therefore, the total acquisition time is shorter and equal to TR multiplied by the number of slices. EPI is characterized by an alternation of phase and frequency encoding gradients, during which time the signal is recorded. Figure 7a shows the EPI scheme, each phase encoding gradient is followed by frequency encoding gradient which polarity is reversed every time. Each time the phase encoding gradient is switched on, a new line of the k-space is filled, while the polarity of the frequency encoding gradient drives the filling direction of each line. In this way each k-space line is filled within a single combination of phase and frequency gradients.

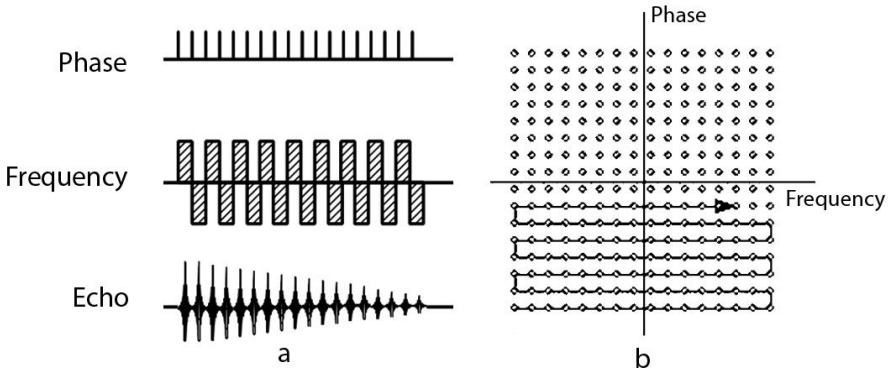

Figure 7 Alternation of phase and frequency gradients, the frequency gradient is applied every time with different polarity (a). The k-space is complied following the arrow direction (b). Each time that the phase encoding gradient is switched on a new line of the k-space is filled, while the polarity of the frequency encoding gradient drives the filling direction of each line.

1.6 Image contrast

As explained above the signal formation depends on the time constants T1 and T2. Such constants are characteristics of each tissue; consequently by choosing appropriate TR and TE is possible to acquire an image with different signal intensities and contrasts (fig. 8, 9). E.g. a long TR (with respect to T1) will give enough time to tissues magnetization to reach the equilibrium value; therefore there will be no difference in terms of signal, except for the proton density of each tissue (fig. 8). A proton density contrast is only dependent on the quantity of water molecules in each tissue and it does not provide a strong contrast (fig. 10). On the other hand, by choosing TR much shorter than T1, there will be different signal intensity for each tissue, which will be reflected by an image contrast driven by T1 (usually called T1 weighted image).

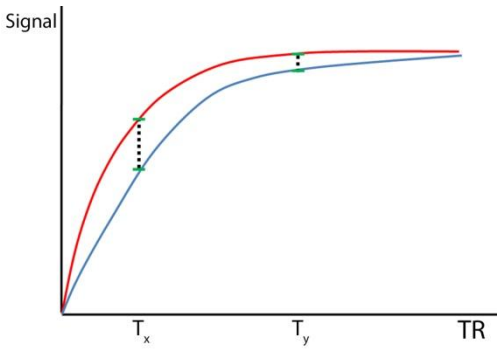

Figure 8 Example of different signal intensities for two different tissues, depending on TR. In T_X the contrast is stronger (difference of T_1 in the two tissues). In T_y the contrast is given mainly from the proton density of the tissues.

Figure 9 shows the most common contrasts that can be obtained by properly combining TR and TE with respect to the characteristics of the tissues.

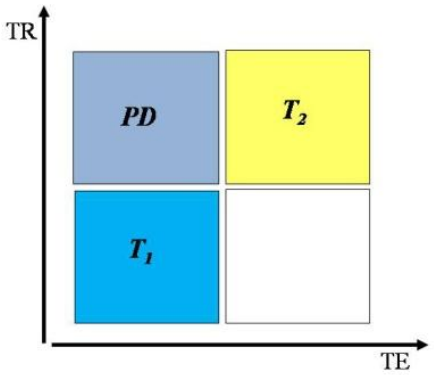

Figure 9 Schematic representation of contrast depending on TR an TE.

From a clinical point of view a different contrast is useful in order to obtain a proper diagnosis for each pathology. T_2 weighted images are useful to spot lesions, T_1 weighted ones are the most useful images for distinguishing different types of tissues.

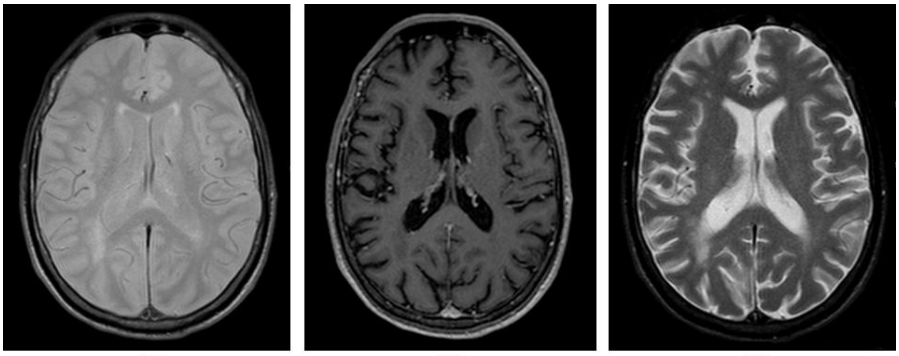

Figure 10 Example of three types of contrast. Proton density (PD): the difference between tissues is quite smooth. T1: the cerebrospinal fluid (CSF) is black and the intensity of the white matter is more hyperintense than the grey matter. T2: the CSF is white and the grey matter is more hyperintense than the white matter.

1.7 Advanced MRI techniques

In the last decades, in addition to conventional MRI techniques, advanced techniques have found their place both in clinical and research environments. These techniques give the chance to obtain detailed structural and functional information more than with conventional MRI sequences. The most important advanced MRI techniques are: perfusion imaging, diffusion weighted imaging (including diffusion tensor imaging), MR spectroscopy and BOLD imaging. This paragraph addresses to a general overview of these techniques (diffusion weighted imaging is described in the next chapter since it is the main argument of this thesis).

- **Perfusion**: Measures like blood volume, mean transit time and regional blood flow can be estimated using perfusion MRI. This technique makes use of both injected exogenous (Gadolinium) and endogenous (blood) tracers. Perfusion performed with exogenous tracers exploits the magnetic susceptibility effect of the Gadolinium, both with T_2 or T_2* weighted images. By comparing the signal before and after tracer's injection is possible to extract hemodynamic parameters. Perfusion performed with endogenous tracer is called arterial spin labeling (ASL). In ASL, the saturated blood serves as a tracer. This saturation provokes a variation in the received signal which is different from an acquisition without prior saturation. A comparison between the signal acquired with and without saturated blood will allow an estimation of some hemodynamic parameters. The main applications of perfusion MRI are to evaluate tumoral regions and vascular pathologies.

- **BOLD imaging**: Neuronal activity causes an increase in oxygen consumption and an increase in local blood flow. Due to oxygen consumption during neural activity, activated areas will show an increase in oxyhemoglobin compared to deoxyhemoglobin. Since deoxyhemoglobin has a paramagnetic effect, such concentration difference can be detected by MRI as change in the T_2* weighted signal. This is the theory behind BOLD contrast imaging. Measuring the BOLD signal will allow spotting activated regions. Since the T_2* difference is quite small, in order to have a good measure, signal averaging is necessary. Since this phenomenon is also very fast, EPI sequences are usually used to acquire this kind of images. Usually there are two main areas of application of the BOLD signal: the resting state and the functional MRI. The former acquires the signal while the subject is in a rest condition, while the latter acquires the signal while the subject is performing a task (motor, cognitive etc..).

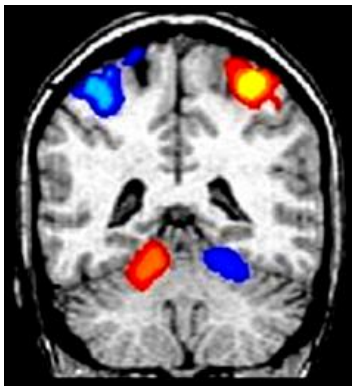

Figure 11 Example of fMRI activation during a motor task. The colored regions are the results of BOLD imaging post processing. As shown in the figure, such result is usually overlaid on to a generic brain image. Each cerebellar hemisphere is activated with the contralateral cerebral hemisphere (same color represents a simultaneous activation).

- **MR spectroscopy**: MR spectroscopy allows obtaining in vivo quantification of tissue molecular composition. Molecular particles, called metabolites, involved in physiological or pathological processes, can be identified with this technique. Each metabolite, depending on its chemical composition, has its own chemical shift. Different chemical shifts correspond to different resonance frequencies of the molecules. The resonance frequency difference between molecules is reported as parts per million and is independent of magnetic field amplitude. This technique does not provide an image but a spectrum of the metabolites present in the investigated area. Spectroscopy acquisitions can be executed using single or multi voxels. By analyzing different metabolites concentration and proportion it is possible to investigate pathologies or to evaluate tumors.

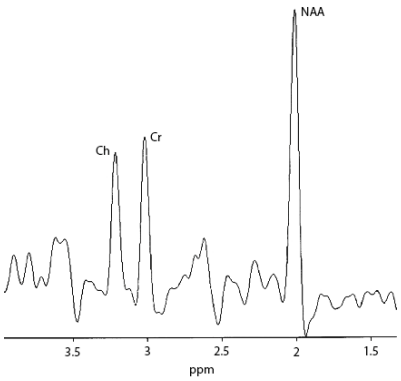

Figure 12 Example of MR spectrum with three metabolites evidenced. Ch = Choline; Cr = Creatine; NAA = *N*-acetyl-aspartate.

Chapter 2: Diffusion MRI

Diffusion MRI is an advanced MRI technique, developed in the early to mid 1990s, that provides a non invasive method to describe microstructural properties of tissue in vivo (Basser and Jones, 2002). Its basis lays on random motion of water molecules that can be measured, with the MRI scanner, by adding diffusion encoding gradients to a standard spin echo EPI sequence. By differentiating areas where water molecules are free to move without constrains, from areas where they have directional constrains, diffusion MRI is able to obtain a wide range of structural information useful to describe and characterize WM tissue both in normal and pathological subjects. Since this technique provides a wide range of previously unavailable in vivo information it has gained huge interest from both clinical and research communities.

2.1 Physics and acquisition of diffusion imaging

Diffusion is a random transport phenomenon, which describes the transfer of material (water molecules) from one location to another over time. The diffusion coefficient, D (mm^2/s), is described by the equation (Einstein, 1956):

$$D = \frac{\langle \Delta r^2 \rangle}{2n\,\Delta t}$$

where $\langle \Delta r^2 \rangle$ represents the mean squared displacement, n the number of dimensions and Δt the diffusion time.

In biological tissues water diffusion is mainly caused by random thermal motions and is strongly dependent on interaction between water molecules and cellular structures. Water molecules that are outside cellular membranes can flow without constraint. On the other hand, water molecules located inside cellular membranes tend to be more restricted and to diffuse along a precise direction.

In fibrous tissues, like WM, water molecules are forced to move in the direction parallel to fiber orientation, consequently diffusion in directions perpendicular to these fibers is almost equal to zero. This situation, where water molecules are forced to move along a particular direction, is called anisotropic. On the other hand, when water molecules are free to move in every direction the diffusion is called isotropic. Two components generally describe diffusion anisotropy: parallel ($\boldsymbol{D}||$) and perpendicular ($\boldsymbol{D}\perp$) diffusion.

Basser et al. (1994) introduced the diffusion tensor in order to describe anisotropic diffusion behaviour. In this model, diffusion is described as a multivariate normal distribution:

$$P\ (\Delta r, \Delta t) = \frac{1}{\sqrt{4\pi\Delta t^3 |\boldsymbol{D}|}} e^{\left\{\frac{-\Delta r^T \boldsymbol{D}^{-1} \Delta r}{4\Delta t}\right\}}$$

where the diffusion tensor is a 3×3 covariance matrix:

$$D = \begin{bmatrix} D_{xx} & D_{xy} & D_{xz} \\ D_{yx} & D_{yy} & D_{yz} \\ D_{zx} & D_{zy} & D_{zz} \end{bmatrix}$$

Diagonal elements of the matrix represent diffusion variances along the x, y and z axes, while off diagonal elements represent the covariance and are symmetric with respect to the diagonal. The eigenvalues (l1, l2, l3) of the matrix represent diffusivity values along the main directions, and the eigenvectors (ê1, ê2, ê3) represent the main diffusion axes (Alexander *et al.*, 2007).

The most practical way to represent diffusion is to use an ellipsoid which axes orientation and magnitude are defined by diffusion matrix eigenvectors and eigenvalues respectively (fig. 13). Consequently, an isotropic diffusion is represented by equal eigenvalues (l1 = l2 = l3); on the other hand, if the eigenvalues have a different magnitude (e.g., l1 > l2 > l3) the diffusion is anisotropic.

Physiological changes (both pathological or normal) may affect the magnitude of eigenvalues and diffusion properties of the tissue. Therefore, by analysing the diffusion tensor it is possible to distinguish normal from abnormal tissue structure.

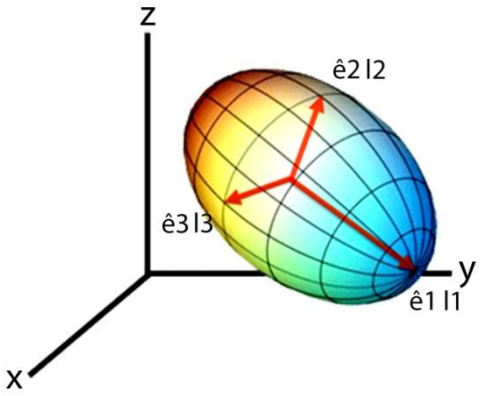

Figure 13 Representation of diffusion in a single voxel. Each axes orientation and magnitude defined by the eigenvectors (ê1, ê2, ê3) and eigenvalues (l1; l2; l3) respectively.

Considering the human brain, in WM tissue the diffusion is usually anisotropic, while it is isotropic in cerebrospinal fluid and grey matter. Therefore, in WM tissue, water molecules main direction is supposed to be parallel to the fibers main axes.

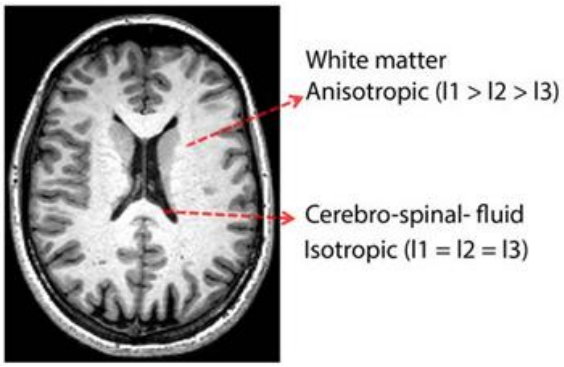

Figure 14 Different image contrasts depending on diffusion properties of tissues.

A common diffusion weighted sequence is a spin echo EPI with the addition of two gradients (diffusion gradients) applied symmetrically before and after the 180° RF pulse (fig. 15). The first diffusion gradient (before the 180° RF pulse) dephases the magnetization, while the second one (after the 180° RF pulse) rephases the magnetization. These gradients have a different effect on signal intensity depending on tissue diffusion properties. In case of tissues with low diffusivity, the dephasement induced by the first diffusion gradient is cancelled from the second one, without any signal attenuation. In case of tissues with high diffusivity, the diffusion gradients dephase the net magnetization causing a signal attenuation.

Such attenuation is:

$$S = S_0 e^{-bD}$$

where S is the diffusion weighted signal, S_o is the signal without diffusion gradients, D is the apparent diffusion coefficient and b (s/mm^2), called *b-value,* is the diffusion weighting coefficient:

$$b = \gamma^2 G^2 \delta^2 \, (\Delta - \delta \, /3 \,)$$

where G, δ, Δ correspond to amplitude, duration and interval of diffusion gradients.

Since, in diffusion weighted acquisition, the diffusion gradients are applied at least along three non complanar directions (paragraph 2.2, 2.3), in order to reduce the total acquisition time it is necessary to use a fast sequence. As for BOLD imaging, also for diffusion the EPI technique is used

to reduce the total acquisition time, with advantages for both patient comfort and reduction of artefacts due to movement in the image.

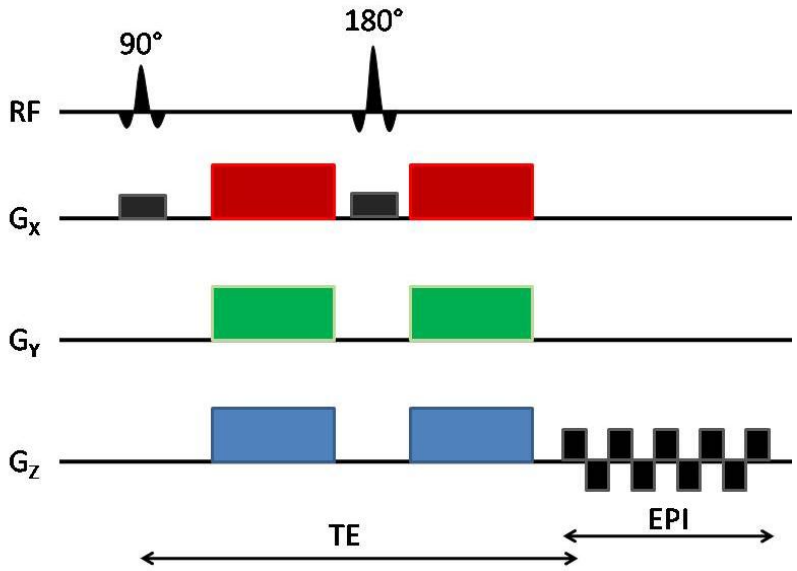

Figure 15 Common diffusion EPI sequence. Red, green and blue rectangles represent the diffusion gradients. Black rectangles stand for slice selection and EPI gradients. For clarity phase and frequency gradients are not reported in the scheme.

The fast acquisition speed of EPI makes it highly efficient, which is important for maximizing the image signal to noise ratio (SNR) and the accuracy of the diffusion measurements. Even if EPI short acquisition time is very useful in order to perform fast and high quality imaging it has some disadvantages. Magnetic field inhomogeneities and eddy currents have a strong influence on this technique leading to image distortions. Eddy current in particular are quite an important problem for diffusion imaging because they are generated from diffusion gradients that are continuously switched on and off. If not huge, eddy current distortions can be corrected during image post processing. Anyway if not corrected, eddy currents artefacts compromise the quality of structural information that can be obtained from diffusion imaging (Alexander *et al.*, 2007).

Depending on the number of diffusion gradients directions it is possible to distinguish between diffusion weighed imaging (DWI) and diffusion tensor imaging (DTI). In the next two paragraphs are explained the main differences, in terms of acquisition and post processing, of these two diffusion techniques.

2.2 Diffusion weighted imaging

If the diffusion gradients are applied along 3 non-collinear directions, it is possible to partially reconstruct the diffusion tensor. This means that the diffusion parameters obtained from this acquisition are dependent from gradients directions. Even if DWI does not describe the whole diffusion tensor it is useful since is a short diffusion based sequence and can be applied for various clinical diagnosis such as:

- early identification and differentiation of stroke
- assessment of cortical lesions in Creutzfeldt-Jakob disease
- assessment of the extent of diffuse axonal injury
- assessment of active demyelination.

The parameter obtained from DWI is the apparent diffusion coefficient (ADC):

$$ADC_i = \frac{\ln(S_i) - \ln(S_0)}{b_i}$$

where "i" indicates a generic diffusion gradient direction and S_0 the signal acquired without diffusion weight.

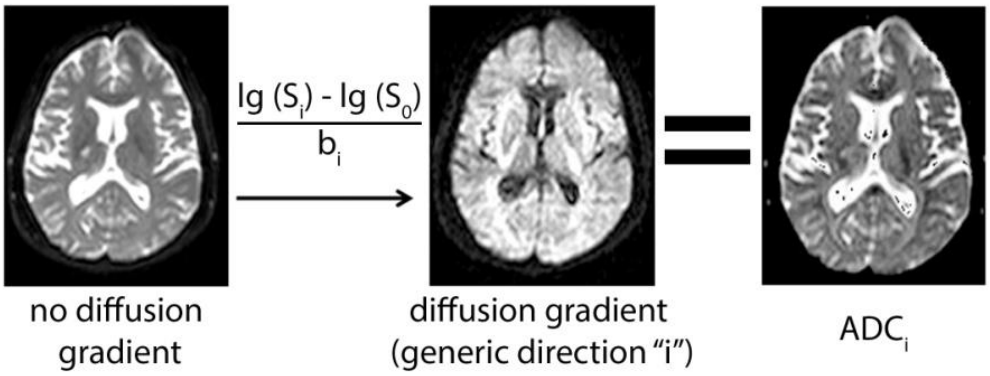

Figure 16 Schematic representation of how ADC map for a generic direction "i" is calculated. S_i and S_0 stand for signal acquired with and without diffusion gradients respectively.

As reported above, ADC depends on the gradient direction. Therefore, in order to minimize this dependence, it is common to use the mean ADC map, calculated by the arithmetic mean, for each voxel, of the ADC along the three directions (x, y, z).

$$\langle ADC \rangle = \frac{ADC_x + ADC_y + ADC_z}{3}$$

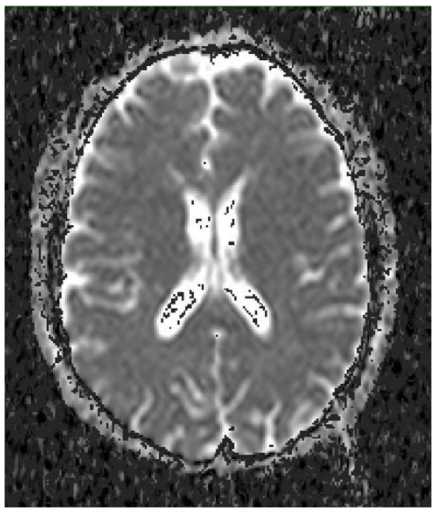

Figure 17 Mean ADC map.

2.3 Diffusion tensor imaging

With DTI it is possible to reconstruct the three dimensional shape of the whole diffusion tensor. In order to perform DTI, diffusion gradients have to be applied along at least six non-collinear directions. Various diffusion direction schemes have been proposed during years. The selection of diffusion gradients directions is very important in order to minimize errors in the evaluation of diffusion parameters. Usually for clinical application the number of directions is between 6 and 12, while for research application at least 45 directions are commonly used. As already reported, artifacts like eddy currents, subject motion, and magnetic field inhomogeneities can highly influence data quality. Therefore, it would be appropriate to correct these artifacts before calculating any diffusion parameter.

The mean diffusivity (MD) is one of the most used (both in clinical and research studies) and simplest DTI derived parameter. MD gives information similar to the one provided by ADC.

$$MD = \frac{l_1 + l_2 + l_3}{3}$$

Using diffusion imaging also it is possible to quantify the degree of anisotropy of each tissue. The parameter that describes tissue anisotropy is the Fractional Anisotropy (FA). FA is a rotationally invariant scalar that quantifies the shape of the diffusion tensor (Alexander *et al.*, 2007; Basser and Pierpaoli, 2011).

$$FA = \frac{\sqrt{(l_1 - MD)^2 + (l_2 - MD)^2 + (l_3 - MD)^2}}{2({l_1}^2 + {l_2}^2 + {l_3}^2)}$$

FA varies between zero and one. Zero represents a total isotropic diffusion (e.g. cerebrospinal fluid), while one represents a total anisotropic diffusion (e.g. corpus callosum, internal capsule). The FA values are calculated voxel by voxel consequently obtaining FA maps.

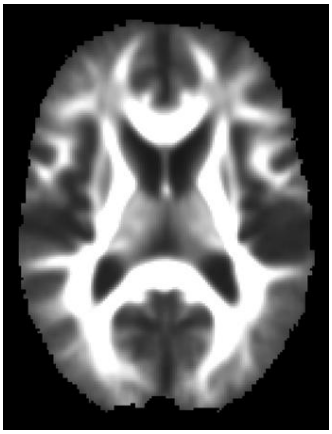

Figure 18 Fractional anisotropy map.

From DTI data it is possible to measure the tensor orientation (major eigenvector direction) voxel by voxel. For areas with high anisotropy (WM tracts), by combining the FA value with the tensor orientation it is possible to obtain color coded (red-green-blue) FA maps showing not only the intensity of anisotropy but also fibers direction (fig. 19). Color coded FA maps are useful to identify and parcellate WM tracts with high accuracy, this is one of the reason that made DTI specificity useful tool both in clinical and research studies.

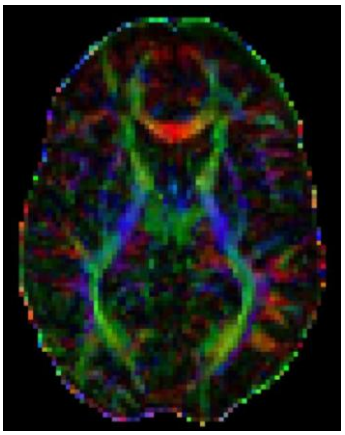

Figure 19 Color coded fractional anisotropy. Red: left-right fibers, blue: feet-head fibers, green: front back fibers.

Recently it has been suggested that the eigenvalue amplitudes or combinations of the eigenvalues (e.g., the radial diffusivity, RD = $(l_2 + l_3)/2$) reveal crucial information in relationship to WM

pathology. RD seems to be an indicator of myelin condition, whereas the axial diffusivity (AxD = l_1) describes axonal degeneration.

2.4 Tractography

DTI based tractography allows to determine intervoxel connectivity on the basis of the anisotropic diffusion of water. Tractography is useful to reconstruct specific WM tracts in human in vivo (Basser *et al.*, 2000). Therefore is used both for diagnosis and for research projects (e.g. basic and cognitive neuroscience). For each voxel, in case of high anisotropy, the primary eigenvector is assumed to be parallel to WM fibers. Therefore by using the diffusion tensor of each voxel, tractography algorithms perform a 3D fiber reconstruction. DTI fiber tracking algorithms are mainly divided into deterministic and probabilistic (Behrens *et al.*, 2007).

Deterministic methods reconstruct fibers by continuous tracking fibers trajectories from one region of interest (seed) to another one (target). Fibers trajectories are reconstructed according to primary eigenvector for each voxel in 3 dimensions. Voxel by voxel, the trajectory direction is changed in order to match the primary eigenvector of the next voxel. In order to respect anatomical coherence, some constraints, like maximum angle between two consecutive eigenvectors or minimum FA values, are usually applied. Like for diffusion based parameters, also for tractography it is important to avoid artifacts as much as possible, in order to have a precise reconstruction of WM tracts.

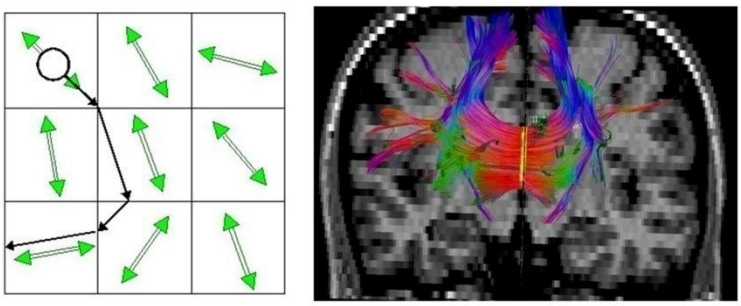

Figure 20 Example of the theory behind deterministic tractography (a). Corpus callosum tract reconstructed using deterministic tractography (b).

Probabilistic fiber tracking methods incorporate probabilistic models into the tracking algorithm. Probabilistic tractography tends to reconstruct “bigger” trajectories than deterministic one, therefore greater portion of a tract can be reconstructed, but at the same time it is necessary to

take care about false positive results. Therefore, also in this case some constrained have to be applied in order to reflect anatomical shape of the tract.

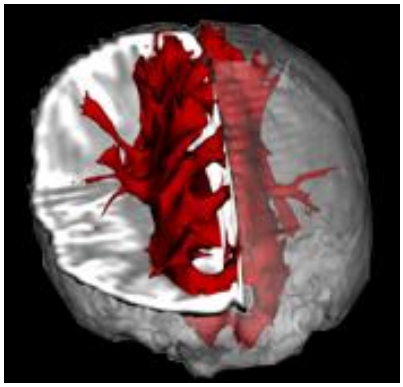

Figure 21 Corpus callosum tract reconstructed using probabilistic tractography.

Tractography algorithms have some fundamental limitations. Indeed, diffusion tractography cannot distinguish fiber direction, therefore every tractography study have to be structured with solid anatomical knowledge. Another important issue of both deterministic and probabilistic tractography is that such algorithms are not able to reconstruct the pathway where there are voxels characterized by crossing fibers, indeed with classical approaches described so far, the pathway was reconstructed taking into account only the principal eigenvector for each voxel.

Within the aim of the thesis project (in particular the one described in chapter 4) it is important to describe an advanced tractography method able to solve the crossing fibers problem. This method falls inside probabilistic tractography algorithms and combines two new techniques: track density imaging (TDI) and constraint spherical deconvolution (CSD) (Tournier *et al.*, 2007; Calamante *et al.*, 2010). TDI allows to gain spatial resolution using post processing methods based on diffusion MRI fiber tracking, to reveal structures beyond the resolution of the acquired imaging voxel. As explained in the following chapter, with this method it is possible to draw seed and target region of interests with higher accuracy than with FA maps or anatomical images. CSD provides fiber orientation distribution that is robust to noise whilst preserving angular resolution and therefore improving the angular resolution of the results. Using CSD it is possible to better estimate fiber orientation and to resolve orientations that are separated by smaller angles than previously possible. Consequently, tractography algorithms based on CSD are able to track pathways running through crossing fiber regions.

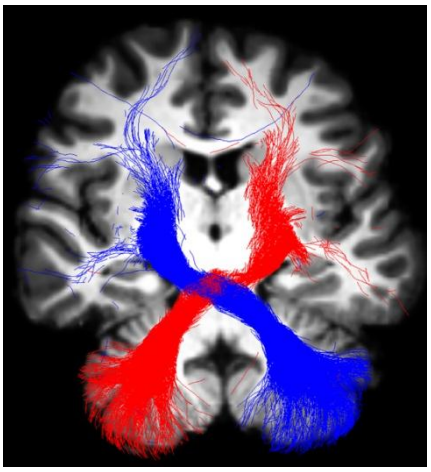

Figure 22 Two contralateral cerebro-cerebellar tracts reconstructed using probabilistic tractography combined with the constraint spherical deconvolution algorithm.

Chapter 3: White matter differences between Alzheimer Disease and Vascular Dementia

AD and VaD together represent the majority of dementia cases. Since their neuropsychological profiles often overlap and WM lesions do not always correlate with VaD, differentiating between VaD and AD results difficult. Therefore, in order to help in characterizing these different forms of dementia, quantitative imaging biomarkers specifically sensitive to AD or VaD would be desirable. In the last years, advanced MRI techniques role in diagnosis has become more and more central. In particular DTI derived parameters have been reported to be helpful in differentiating between dementias. Therefore, the main aim of this part of the thesis was to analyze DTI data acquired from patients affected by VaD, AD and in healthy controls (HC) in order to investigate core WM changes (in terms of DTI based parameters). To reach this goal a whole brain statistical analysis on DTI data acquired with a 3T MRI scanner was performed. WM alteration patterns, considered useful in distinguishing between VaD and AD, were successfully identified. In the following paragraphs the pipeline used in the analysis process is explained in detail and the obtained results are discussed in terms of their utility during the diagnostic process.

3.1 Alzheimer Disease and Vascular Dementia: an overview

Dementia is one of the major personal and financial issues of older people; since society mean age is constantly rising, also dementia incidence rate is growing. AD and VaD together represent the majority of dementia cases (Rizzi *et al.*, 2014). AD is characterized by progressive deterioration in memory, language, perceptual skills, attention, orientation and problem solving. VaD is characterized by coexistence of cognitive impairment (e.g. semantic memory, executive/attentional function etc...) and cerebrovascular disease. The entity of impairment in VaD is proportional to number, location and extent of cerebrovascular lesions (Suri *et al.*, 2014). For what concerns brain areas involved with the diseases, in AD temporal and parietal lobes are the most impaired ones, while in VaD the cerebral impairment is dependent from various vascular etiologies, even if brain anterior areas are reported to be the most affected ones (Savoiardo and Grisoli, 2001; Sugihara *et al.*, 2004; Mayzel-Oreg *et al.*, 2007). However, confirmed cases of VaD and AD showed that their neuropsychological profile often overlap and WM lesions do not always correlate with VaD, (Olsson *et al.*, 1996; Reed *et al.*, 2007; Zarei *et al.*, 2009). Therefore, in order to better characterize these different forms of dementia, quantitative biomarkers specifically

sensitive to AD or VaD would be desirable. Last decades advances in neuroimaging, in particular in MRI techniques, allow the investigation in humans in vivo of structural and functional brain alterations. Advanced MRI techniques role in diagnosis has become more and more central, they have been indeed recommended as a part of the diagnostic pipeline (McKhann *et al.*, 2011). In particular, DTI derived measures quantitatively describing water molecules movement in the WM, are useful to highlight WM changes that could be related with the disease (Acosta-Cabronero *et al.*, 2010). FA and MD are the DTI derived parameters most used to characterize dementia, the former reflects anisotropy properties of WM tissues, while the latter reflects the magnitude of water diffusion. Even if FA and MD have been widely used in studying dementia, in order to have more accurate description of molecules diffusion in the WM, it is useful to analyze also axial diffusivity (AxD) and radial diffusivity (RD). AxD refers to the molecules movement parallel to the primary diffusion direction, while RD refers to the molecules movement perpendicular to the primary diffusion direction. As FA and MD, RD and AxD also provide information relative to WM fibers (see chapter 2). Therefore, taking in to account all these parameters instead of only FA and MD, it is possible to have a more complete view of diffusion into WM (Mori and Zhang, 2009; van Bruggen *et al.*, 2012). However, no standard values or alteration patterns of DTI derived parameters have been defined to distinguish between AD and VaD (Alves *et al.*, 2012; Suri *et al.*, 2014). An analysis approach that, combined with DTI derived data, has been proved to be useful in analyzing dementia is the Tract based spatial statistics (TBSS). TBSS is an automated voxel wise analysis method that gives the opportunity to compare the whole WM in groups of subjects, without any predefined region of interest (Smith *et al.*, 2006). With TBSS it is possible to improve the objectivity and interpretability of DTI studies, performing a whole brain analysis and avoiding some classical problems related to dementia. One of the main problem in voxel wise analysis on patients affected by dementia lies in the atrophy caused by this pathology, that leads to misalignment of the template. Using TBSS this problem is solved since from each subject is extracted the "main skeleton" (i.e. the centre of all tract common to all subjects) from normalized FA images, resolving the misalignment problem. TBSS has been largely used in the study of AD (Acosta-Cabronero *et al.*, 2010; Shu *et al.*, 2011). To the best of our knowledge, only Zarei et al. (2009) used TBSS to study differences in terms of FA between AD, VaD and elderly controls. Other groups focused their attention only on specific brain structures, Sugihara (2004) used a ROI (corpus callosum and anterior/posterior WM) approach to investigate differences between AD, VaD and HC. Hippocampal microstructural changes in VaD with respect to HC were recently

studied by Ostojic et al. (2015). As regards subtypes of VaD (e.g patients affected by Vascular Mild Cognitive Impairment or Subcortical Ischaemic Vascular Dementia) both region of interest and whole brain approaches were performed (see Alves et al. (2012) and Suri et al. (2014) for a review of past studies about subtype of VaD).

Therefore the main aim of this study was to use TBSS approach to assess specific pattern of WM alterations for each kind of dementia, without any a priori region of interest and analyzing changes of multiple DTI derived parameters (FA, MD, AxD, RD).

To the best of our knowledge, this is the first study where FA, MD, AxD and RD, obtained from 3T DTI data, are used together in order to distinguish AD, VaD and HC.

3.2 Tract based spatial statistics

There has been growing interest in the study of WM structure and connectivity. Diffusion derived parameters have been widely used to describe these properties. In order to have a complete vision of WM structure, it is useful to perform whole brain analysis. Very often, in particular studying diseases that have an impact on cerebral morphology (e.g. atrophy caused by AD), the whole brain analysis results compromised. Such irregularity in the morphology of the brain makes registration algorithms not able to properly align diffusivity maps to a template, consequently influencing the quality of results.

TBSS is an automated voxelwise analysis method able to solve misalignment issues using a non-linear registration process and a projection onto a tract representation (mean skeleton) alignment invariant. One of the core point of TBSS is the identification of a mean FA skeleton that represents the center of all WM bundles common to all subjects. Once the skeleton is identified each subject's FA map is registered onto it. This registration is based on "correspondence" of FA value between each voxel of the skeleton and the subjects' FA maps (Smith *et al.*, 2006).

The main TBSS steps are the following:

- From all subjects, a common registration target is identified, then each subject's FA map is aligned to this target. The best subject is considered as the one that, after having registered every subject to every other one, has the minimum distance to all other subjects.
- After that, all subjects are aligned to the target; they are then aligned to the MNI 152 template (1x1x1mm) and a mean FA image is created by averaging all subjects FA maps. From the mean FA map the mean FA skeleton is created, that includes tracts common to all

subjects. The FA skeleton is obtained by doing a 3x3x3 voxel neighborhood "research" in the mean FA map. This means to map mean FA voxels combining maximum FA values and diffusivity directions, in order to find voxels with the highest FA value and consider them as the center of the tract.

- As last step, each subject's FA map (previously aligned to the best target) is projected onto the skeleton. A further registration is accomplished by filling each voxel of the skeleton with values from subject's FA map, which may be displaced: the best correspondence is found by searching the maximum FA value in the direction orthogonal to the local skeleton tract.

3.3 Analysis pipeline

A total of 93 subjects were acquired with a 3T Siemens Skyra scanner (Siemens, Erlangen, Germany) during the study. Subjects were divided in three groups: 31 AD (age (72 ± 7) yrs, 12 females (F), Mini Mental State Examination (MMSE) score = 16 ± 6), 27 VaD (age (77 ± 8) yrs, 21 F, MMSE = 18 ± 4) and 35 HC (age (69 ± 10) yrs, 17 F, MMSE = 28 ± 1). Inclusion criteria for study participants were: male or female, more than 65 years of age, and of any race or ethnicity. All subjects provided written informed assent prior to study participation.

Diffusion weighted data were acquired using a twice refocused spin echo EPI sequence with the following parameters: TR = 10 s, TE = 97 ms, 70 axial slices with no gap, acquisition matrix = 122×122, 2 mm isotropic voxel; 64 volumes with non-collinear diffusion directions with b = 1200 s/mm^2 and 10 volumes with no diffusion weighting (b_0 = 0 s/mm^2). For anatomical reference a whole brain high-resolution 3DT1w scan was acquired using the following parameters: TR = 2300 ms, TE = 2.95 ms, TI = 900 ms, acquisition matrix = 256 x 256, in plane resolution 1.05 x 1.05 mm, slice thickness 1.2, 176 sagittal slices, acquisition time 5 min 12 s.

DTI analysis

Processing of diffusion weighted imaging data was performed using FSL (FMRIB Software Library, http://fsl.fmrib.ox.ac.uk/fsl/fslwiki/).

First, fslmaths (part of FSL software) was used to average each subject's 10 volumes acquired without diffusion weighting (b_0 = 0 s/mm^2). From this point onward, each subject's DTI data are composed of a total 65 volumes (the first one is the mean b_0 image, obtained in the previous step using fslmaths, while the sequent 64 volumes are diffusion weighted ones). Artifacts due to eddy

current were corrected using eddy_correct tool, provided by FSL, that aligning each diffusion weighed volume to the mean b_0 one by applying an affine transformation. Next, in order to obtain DTI derived maps only from the brain regions, a binary brain mask was obtained from the mean b_0 volume using Brain Extraction Tool (Smith, 2002). Finally, DTIFIT, part of the FDT toolbox of FSL, was used to generate individual FA, MD and AxD maps for each subject. RD maps were calculated using fslmaths to implement the RD formula (see paragraph 2.3 for RD analytical definition).

Tract based spatial statistics

TBSS was performed to investigate the voxel wise distribution of FA, MD, AxD and RD changes among groups. Such analysis was executed using the TBSS tool in the FMRIB software library. TBSS has already been described in the previous paragraph, for a more detailed description of the complete TBSS pipeline see Smith et al. (2006). Here is reported a recap of the main steps.

- FA maps from all subjects were nonlinearly aligned to the most representative one (as suggested in http://fsl.fmrib.ox.ac.uk/fsl/fslwiki/TBSS/UserGuide, paragraph 2.1.3). The average time to find the most representative subject is 5 minutes x N x N (http://fsl.fmrib.ox.ac.uk/fsl/fslwiki/TBSS/UserGuide), where N is the number of subjects. Because of the time that it would have taken if all cohorts of subjects were used for the best subject selection, the most representative one was chosen from a cohort of 15 subjects (5 for each categories) randomly chosen from each group.
- All the aligned FA images were translated to the standard MNI152 template (1x1x1 mm).
- The mean FA image and its mean WM skeleton were created from all subjects FA.
- The FA images were projected onto the mean WM skeleton and the resulting maps were compared in a cross subjects statistical analysis, that is described in the next section.
- MD, AD and RD maps were also projected in to the mean WM skeleton using the same projectors vectors that were obtained in the FA maps alignment described above.

Statistical analysis

Since in the statistical analysis the mean FA value of the brain (considered as WM and grey matter (GM) added together) was used as covariate, alignment and segmentation processes were needed in order to obtain this value for each subject. WM and GM were segmented from 3DT1w images using FAST algorithm (Zhang *et al.*, 2001). Subsequently, FA map of each subjects was aligned to

the respective 3DT1w volume using FLIRT (Jenkinson and Smith, 2001; Jenkinson *et al.*, 2002a). Finally, mean FA value of the brain was obtained for each subject by overlapping WM and GM segmentation, previously obtained, with the FA maps aligned to the 3DT1w space. Mean FA was calculated on the whole brain (GM plus WM) in order to not underestimate WM bundles extension and to consider all brain structures with the only exception of cerebrospinal fluid.

The voxel wise statistics from TBSS images were performed using Randomise (Winkler *et al.*, 2014), a FSL tool for nonparametric permutation inference on neuroimaging data. The mean FA skeleton (thresholded at 0.2) was used as mask, the number of permutations was set to 5000. Significance of difference among groups was tested at $p<0.02$ (threshold free cluster enhancement corrected). Age, gender and mean FA of the whole brain (WM+GM) tissue were used as covariates for the statistics. Comparison was performed for all parameters (FA, MD, AxD, RD), testing differences among all groups of subjects.

3.4 Results

Results are reported in the three following sub paragraphs, where comparisons between groups (*HC vs AD*, *HC vs VaD*, *AD vs VaD*) are described. All brain areas reported in the results were tested by a significance at $p<0.02$. All results are summarized in table 1.

	Table 1a - HC vs AD	
	AD < HC	**AD > HC**
FA	CRBL - PhG - CC (body and splenium) - ThR - occipital, parietal and temporal lobes	Left CST
MD		WCA, except for: ThR, anterior CG and CST
RD		WBA, except for: ThR, anterior CG and CST
AxD		WCA, except for: ThR, anterior CG and CST

	Table 1b - HC vs VaD	
	VD < HC	**VD > HC**
FA	WBA, except for: anterior PhG, CC (splenium), CG and CST	
MD		WBA, except for anterior right PhG
RD		WBA, except for anterior right PhG
AxD		WBA, except for anterior ight PhG

	Table 1c - AD vs VaD	
	AD < VD	**AD > VD**
FA	Anterior PhG	CRBL - left ThR– SLF
MD	CRBL - ThR - SLF - CC (genu) - CST	Anterior Right PhG
RD	CRBL - ThR - SLF - CC (genu) - CST	Anterior PhG
AxD	CRBL - ThR - SLF - CC (genu) - CST	

Table 1: FA reductions and MD, RD, and AxD increases. 3a) AD compared with HC; 3b) VaD compared with HC; 3c) AD compared with VaD. WBA = widespread brain alteration, WCA = widespread cerebrum alteration, CRBL = cerebellum, ThR = thalamic radiation, PhG = parahippocampal gyri, CC = corspus callosum, CST = cortico spinal tract, SLF = superior longitudinal fasciculus, CG = cingulate gyrus. Blanks cell=no statistically significant difference.

HC versus AD (tab.1a)

AD patients, compared with HC, showed a widespread reduction of FA in the posterior part of the brain and in the temporal lobes. In particular, posterolateral cerebellum (CRBL), both parahippocampal gyri (PhG) (fig.23a), thalamic radiation (ThR), body and splenium of corpus callosum (CC) (fig.24a) emerged as areas of decreased FA. In AD patients an increase of MD, RD and AxD was found in widespread brain regions, with the exception of ThR (fig.25a), anterior cingulate gyrus (CG) and corticospinal tract (CST). In CRBL, no changes of MD and AxD were found, while an increase of RD emerged only in posterolateral CRBL.

HC showed decreased FA in left CST, while no areas of increased MD, RD and AxD were revealed.

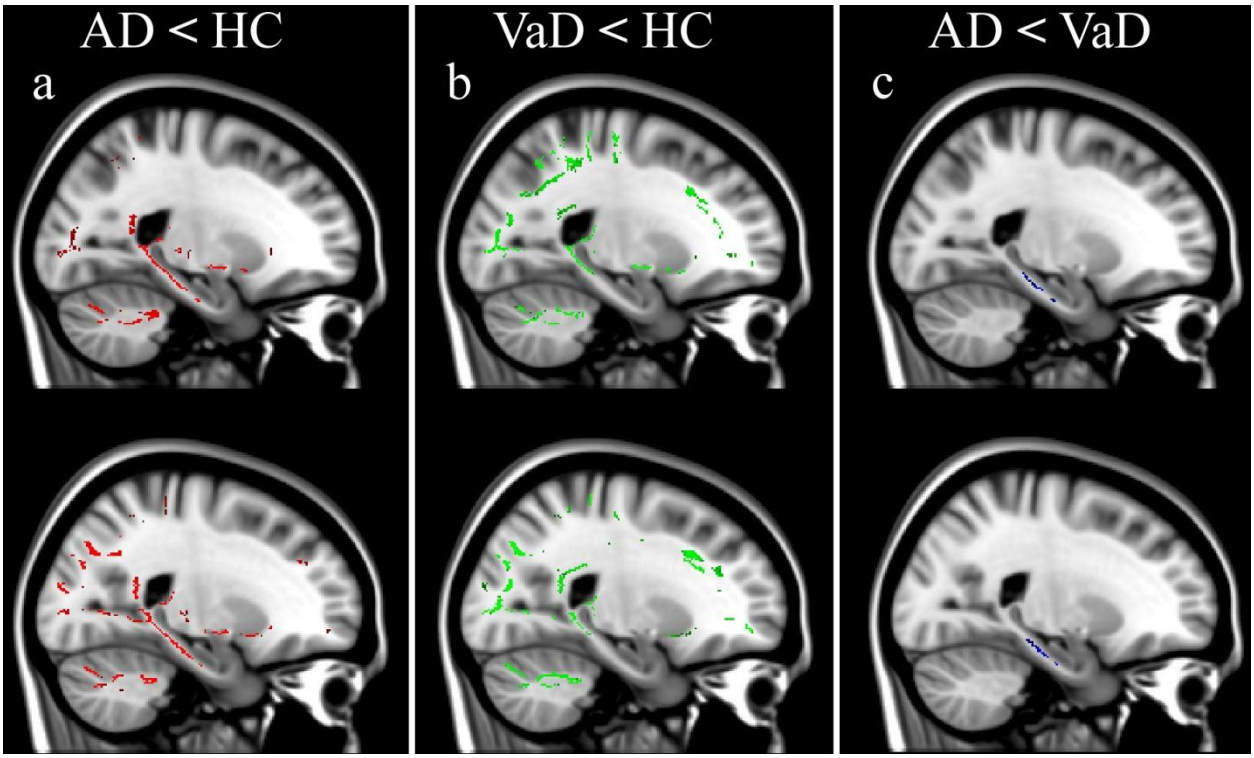

Figure 23FA reductions in AD versus HC (a), VaD versus HC (b) and AD versus VaD (c). Top row: left hemisphere. Bottom row: right hemisphere. All results are overlaid onto the MNI 152 template. X coordinate top row = -22mm, X coordinate bottom row = 23mm.

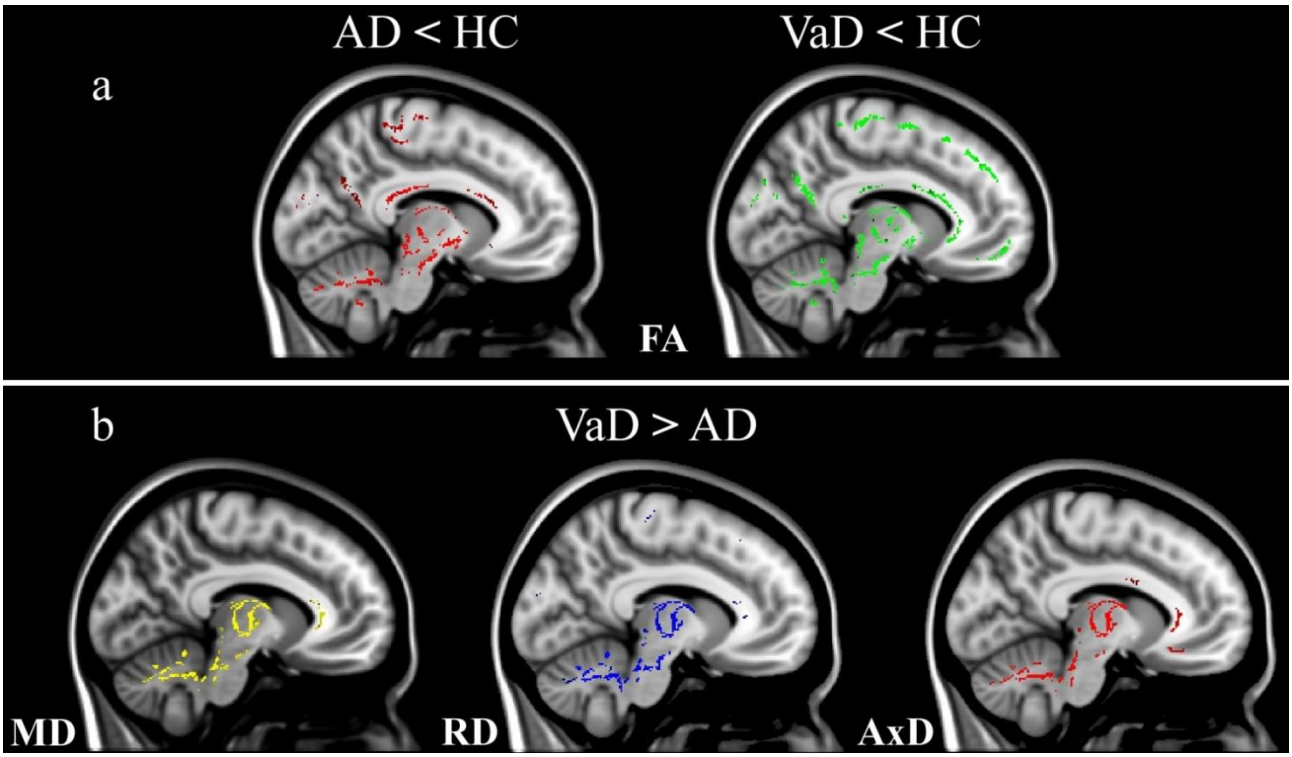

Figure 24FA reductions in AD and VaD with respect to HC (a). Increases of MD, RD, AxD in VaD with respect to AD (b). All results are overlaid onto the MNI 152 template. X coordinate = -9mm.

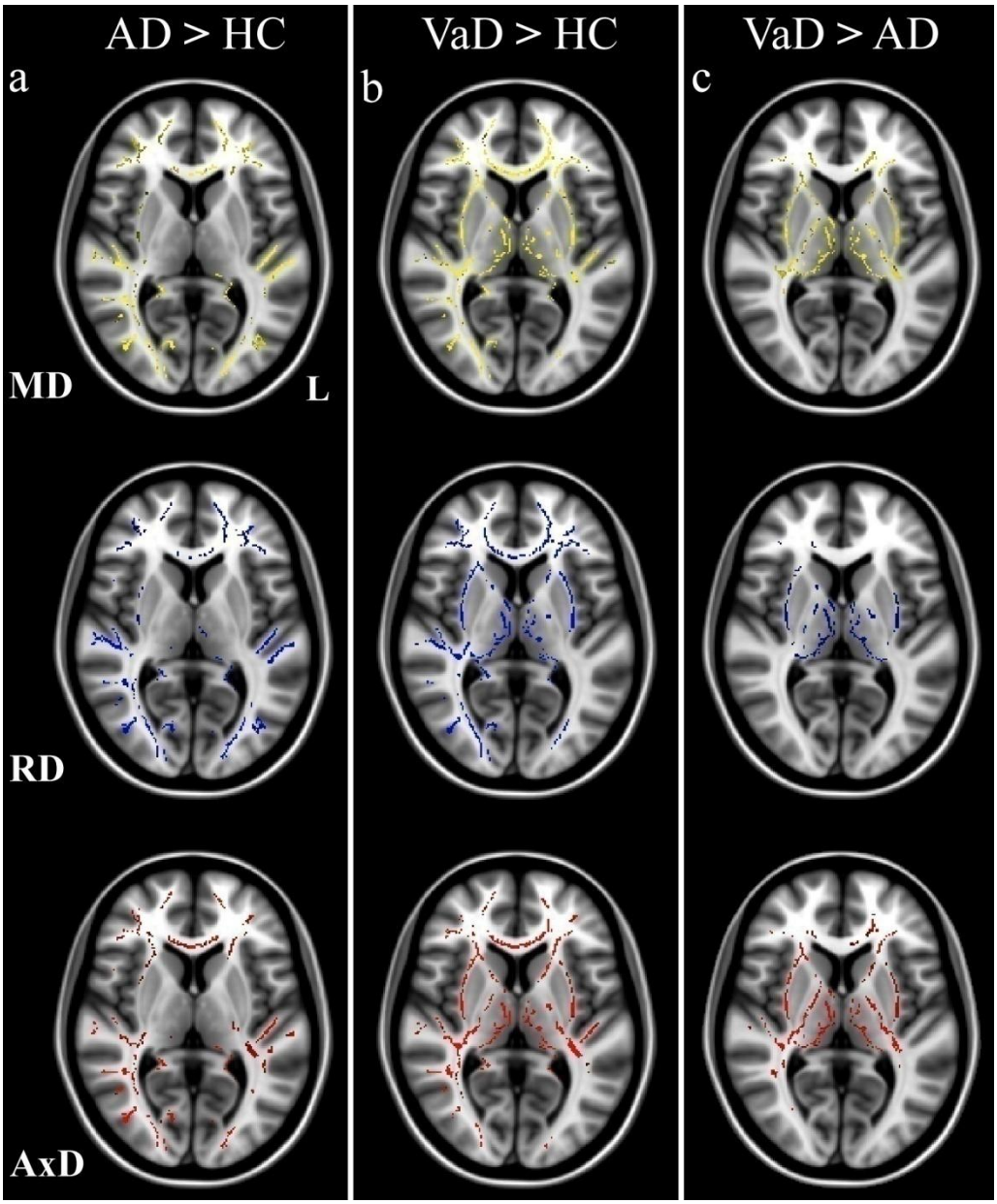

Figure 25MD (top row), RD (middle row) and AxD (bottom row) increases in AD versus HC (a); VaD versus HC (b), and VaD versus AD (c). L = left hemisphere. All results are overlaid onto the MNI 152 template. Z coordinate = 4mm.

HC versus VaD (tab.1b)

VaD patients, compared with HC, had significantly reduced FA in the whole WM with the exception of anterior part of PhG (fig.23b), splenium of CC (fig.24a), CG and CST. Increases of MD, RD and AxD were found in the whole WM of VaD patients with the exception of the anterior right PhG.

No areas of FA reduction or MD, RD and AxD increment were found in HC with respect to VaD subjects.

AD versus VaD (tab.1c)

AD compared with VaD patients, showed a reduction of FA in both left and right anterior PhG (fig.23c), in these areas an increase of RD was also found, while higher value of MD was found only in the right anterior PhG. No areas of increased AxD were found in AD compared with VaD.

In VaD with respect to AD, a reduction of FA and an increase of MD, RD and AxD were found in posterolateral CRBL (fig.24b) , left ThR and bilateral superior longitudinal fasciculus. Increases of MD, RD and AxD in VaD patients were also found in right ThR, genu of CC (fig.24b) and bilateral CST.

3.5 White matter bundles useful in the diagnosis

The analysis process revealed some WM alterations patterns specific to AD and VaD, useful in distinguishing between these pathologies. Since their psychological spectrum often overlap and ischemic WM lesions do not necessarily can be considered as pure VaD symptoms, distinguishing between VaD and AD subjects is one of the main issue in the dementia field (Olsson *et al.*, 1996; Reed *et al.*, 2007; Zarei *et al.*, 2009). Therefore, results presented here give additional information with potential implications in diagnosis. It is to note that the found regions emerged from an analysis of the whole WM, without using any predefined region of interest or other anatomical assumptions. Furthermore, both anisotropy (FA) and diffusivity (MD, AxD and RD) parameters were investigated, taking into account changes due to alterations of both anisotropy and magnitude of water diffusion in the whole brain (Shu *et al.*, 2011). As reported in other studies (Takahashi *et al.*, 2002), using data acquired with a 3T scanner, we obtained a more accurate quantification of anisotropy than with lower field scanners. Even if in the recent years TBSS has been widely used to study differences between dementia (Zarei *et al.*, 2009; Acosta-Cabronero *et al.*, 2010; Suri *et al.*, 2014), to the best of our knowledge, there are no 3T studies were a TBSS was performed, using FA, MD, AxD and RD together, in order to investigate the core WM structural changes in patients affected by VaD, AD.

From this point onward, the word “impairment” refers to FA decrease and/or increase of MD, RD and AxD. Indeed, as reported in several studies, such trends reflect alteration of WM tracts and, consequently, a supposed impairment (O'Dwyer *et al.*, 2011; Bosch *et al.*, 2012). The relationship between DTI parameters alterations and changes of fibers properties (e.g. demyelination, tissue loss, axon properties) is not absolute and it is strongly dependent from their combination (e.g.

lower FA and higher MD may indicate areas with a loss of structural barrier, while decreased FA with increased RD is supposed to be linked with loss of myelin) (Beaulieu *et al.*, 1996; Song *et al.*, 2003; Smith *et al.*, 2007; Gold *et al.*, 2010; O'Dwyer *et al.*, 2011). Anyway, the aim of this study is not to establish the exact relationship between DTI parameters changes and physiology.

Several areas of differences between groups emerged from the analysis. Relying on the specific pattern of each area and the existing literature, some of them seem to be particularly useful to distinguish between pathologies. Such areas are deeply discussed in the following sections of the paragraph. Briefly, PhG resulted to be distinctive, not only, as it is known, between AD patients and HC (Detoledo-Morrell *et al.*, 1997; Salat *et al.*, 2010; Echávarri *et al.*, 2011), but also between AD and VaD subjects. Indeed, comparing AD with VaD patients, the only impaired area in AD was anterior PhG. The CC also is a structure useful in discriminating between pathologies. Indeed, dementia groups when compared to HC, have a different pattern of decreased FA in CC (decreased FA in splenium for AD and in genu for VaD). ThR is another WM structure where changes of DTI parameters could discern between AD and VaD; here indeed MD, RD and AxD increases were found only in VaD (both versus AD and HC, while no impairment in ThR, in terms of MD, RD and AxD, was found comparing AD with HC).

Considerations reported above link to a posterior impairment in AD and a frontal impairment in VaD, indeed PhG and splenium of CC resulted more damaged in AD, while ThR and genu of CC in VaD. Such findings support previous studies, which describe differences of posterior/frontal impairment between these dementia (Suri *et al.*, 2014) and suggest a further cut off about the brain regions involved in these two forms of dementia. In the following part of the paragraph a section is dedicated to each group, with the scope to evidence WM alterations characteristics of each of them.

HC alterations

No areas of alterations were found in HC when compared with VaD patients, while in the comparison with AD patients, FA in the CST resulted to be minor in HC than in AD group. A possible explanation of such reduction is given by Teipel et al.(2014), here the increase of FA in the CST of AD patients is associated with an increase of Mode. Such measure reflects shape characteristics of the diffusion tensor (Ennis and Kindlmann, 2006). Their hypothesis is that the simultaneous increase of both FA and Mode reflects a loss of crossing fibers that leads to an increment of anisotropy. Consequently, according to this view the increment of FA is sign of

impairment in AD patients with respect to HC and not vice versa. Since except for the study cited above, higher FA value in the CST of AD when compared to HC is not reported in literature, further investigation is needed in order to understanding the meaning.

AD alteration

The most important areas, among those emerged from the analysis, which seem to characterize AD, are PhG and CC. In PhG, comparing AD subjects with HC, FA increased (fig.23a) and MD, RD and AxD decreased. When compared with VaD patients, in both left and right anterior PhG , AD patients showed a decrease of FA (fig.23c) and an increase of RD. A decrease of MD emerged in the right PhG. It is to note that, with a lower significance (< 0.05), also left PhG resulted characterized by an increase of MD, giving a further proof of PhG impairment in AD. These findings confirm the literature (it is well know that PhG is an area of major impairment in AD) (Detoledo-Morrell *et al.*, 1997; Salat *et al.*, 2010; Echávarri *et al.*, 2011) and show that PhG is more affected in AD than in VaD. Therefore, we argue that FA and RD alteration patterns in PhG can be used as distinguishing markers between pathologies.

CC is another structure in which TBSS analysis revealed differences useful to characterize AD patients. Comparing AD patients with HC, this area was characterised by an increase of all diffusivity parameters (MD, RD and AxD), while a decrease of FA emerged mainly in the posterior part of the CC (fig.24a). Therefore, in AD with respect to HC, fibers in the posterior part of CC are more impaired, indeed they are characterised by a loss of anisotropy and an increase of diffusion magnitude. Such finding suggests a different alteration pattern between anterior and posterior CC fibers. From a connectivity point of view, CC white matter impairment could lead to a "disconnection" between the two hemisphere and consequently to cognitive impairment, due to a disruption of communication between interconnected networks (Genc *et al.*, 2015). Physiological implications of CC alterations in AD have already been discussed (Takahashi *et al.*, 2002; Stricker *et al.*, 2009; Acosta-Cabronero *et al.*, 2012). As regards the aim of this study, the importance of the result obtained in CC emerges when associated with the one obtained in VaD in the same WM structure (see "*Differentiate between dementias*" section of this paragraph).

In ThR we found a decrease of FA, with no changes of MD, RD, and AxD, in AD with respect to HC. Our results are in agreement with previous literature reporting thalamic alterations in AD (Medina *et al.*, 2006; Salat *et al.*, 2010; Zarei *et al.*, 2010). Decreased FA in ThR along with no changes of MD in AD compared with HC, was found by Rose et al. (2008), who hypothesized an involvement

of perturbed cortico thalamic and thalamo cortical pathways. Considering only AD patients, this result is just a literature confirmation, but examining ThR alterations found in VaD such structure seems to assume an important role in distinguishing between dementias.

Posterior part of bilateral CG resulted impaired in AD when compared with HC; here indeed MD, RD and AxD increase in AD. Such finding is in agreement with previous studies (Acosta-Cabronero *et al.*, 2012; Bosch *et al.*, 2012) leading to a cognitive impairment of AD patients (Gili *et al.*, 2011; Suri *et al.*, 2014). Indeed, the CG is one of the major associative WM fasciculus, connecting various cerebral areas (frontal, temporal, and parietal regions) (Bozzali *et al.*, 2012), therefore a damage in CG involve a "disconnection" between such areas.

In the posterolateral areas of CRBL, AD compared with HC, showed a decrease of FA and an increase of RD. To the best of our knowledge relevant to TBSS studies, only few works reported cerebellar impairment in AD when compared to HC (Acosta-Cabronero *et al.*, 2010; Liu *et al.*, 2011; Teipel *et al.*, 2014). However, other works suggested cerebellar impairment in AD (Wang *et al.*, 2007; Castellazzi *et al.*, 2014) using different analysis methods. It is to note that we found an impairment mainly in the posterior and lateral areas of the CRBL. Since these areas are supposed to be involved in cognition (Stoodley and Schmahmann, 2010), we argue that this result could reflect cognitive impairment in AD patients.

VaD alterations

To find specific patterns of alteration in VaD resulted more difficult than in AD. Indeed, in more than one comparison widespread areas of alterations emerged (see tab.1 for detail). Such difficulty in finding defined WM alterations patterns in VaD is reported also in other studies. FA reductions are reported in widespread brain regions in VaD, both in the comparison with AD patients and HC (Sugihara *et al.*, 2004; Mayzel-Oreg *et al.*, 2007). Other works identified an impairment in frontal brain areas and in CC (Zarei *et al.*, 2009; Suri *et al.*, 2014). Such lack of information could be due to pathology characteristic (e.g. random locations of WM lesions) and to the lower number of studies focused on WM impairment in VaD with respect to AD. Indeed even if in the last years there is a growing interest in understanding and characterizing VaD, there are few DTI based studies where VaD, AD and HC are directly compared, in particular using all DTI derived parameters (Suri *et al.*, 2014). However, from the analysis some areas emerged, that we argue to be helpful to characterize this kind of dementia.

VaD patients showed impairment in the anterior part of the CC both in comparison with HC and AD patients. A decrease of FA emerged in the genu of CC, comparing AD with HC (fig.24a), while an increase of MD, RD and AxD was found in the same part of the CC comparing VaD with AD (fig.24b). Lower FA values in this area have already been reported comparing patients affected by VaD and other subtype of VaD both with HC and AD patients (Zarei et al. 2009, Fu et al. 2012, Wu et al. 2014, Suri et al. 2014). Suri et al (2014) hypothesize that an impairment in the anterior part of the CC in VaD could lead to a loss of intraemispheric prefrontal connection with a consequent cognitive decline. Interestingly both VaD and AD patients have an impairment in the CC but in VaD the anterior part is the one more affected while in AD is the posterior the one which reflects more alteration, such different posterior/anterior alterations trend in CC is important within the aim of distinguishing between dementias. Furthermore, since AD did not show any sign of impairment in the CC when compared to VaD, while VaD showed an increase of diffusivity values, it seems that the CC (at least the anterior part) is mostly affected in VaD.

Comparing VaD patients with HC, we found an increase of MD, RD and AxD in widespread brain regions with the exception of anterior right PhG. At the same time, when considering FA reduction, the bilateral anterior part of the PhG does not result impaired in VaD (fig.23b). Even if such result has not a key role in characterizing VaD impairment, it acquires importance when compared to that obtained in the same structure in AD. In ThR, increases of MD, RD and AxD in VaD subjects, with respect to AD ones and HC, were found (table 1.c, fig.25b-c). In the comparison with HC, VaD patients showed also a decrease of FA (tab.1b). To the best of our knowledge there are no DTI based studies reporting this result; however damage in thalami is known to be associated with VaD and to cause cognitive and psychological alterations (Cummings, 1994; Szirmai *et al.*, 2002). Our findings strengthen the role of thalami in characterizing VaD and suggest other structural and functional MRI studies necessary to clarify the role of ThR in VaD. According to our results MD, RD and AxD increases in ThR seem to be characteristic of VaD; indeed, looking at figure 25 it is possible to see that AD patients do not have any alteration in these areas.

In CRBL, when VaD patients are compared with AD ones, a reduction of FA and an increase of MD, RD and AxD (fig.24b) emerged in the posterior lobules (tab.1c). Posterior cerebellar areas are supposed to be involved in cognitive functions (Stoodley, 2012); such finding suggests a major cerebellar cognitive impairment in VaD patients than in AD ones. Since this result has never been reported, more studies are necessary to verify possible implications of such WM alteration.

Further studies with larger cohort of subjects and different MRI analysis could be helpful to clarify the reasons and possible consequences of alterations we found in VaD, in particular the ones with a low literature validation.

Differentiate between dementias

The previous part of this chapter was important to explain and discuss all alterations found in each comparison. Anyway, at this point, it is necessary to summarize which are the WM bundles that seem to be more useful in distinguishing between dementia.

PhG and CC showed dementia specific alteration patterns. Even if previously were discussed also other WM, PhG and CC are considered to be more relevant since also other studies considered them as specific for AD and VaD. This work indeed is not mean to substitute existing clinical knowledge but to find a way to help the diagnosis when cases are uncertain, therefore results of this analysis have to be considered like an help for the diagnosis and not like an alternative.

In PhG it is possible to distinguish between anterior and posterior alterations. Indeed, while the posterior part is impaired in both dementia groups, the anterior one seems to be specific for AD. Lower FA values in posterior PhG emerged in both dementia groups compared to HC, while the anterior part showed lower FA only in AD, both compared with HC and VaD (fig.23). Anterior PhG also showed an increase of MR, RD and AxL in AD with respect to VaD.

Anterior/posterior dementia specific alterations emerged also in CC, figure 24a shows how a different pattern of FA reduction (compared with HC splenium resulted impaired in AD and genu in VaD) emerged in this area. Furthermore, comparing dementia groups, in VaD we found an increase of MR, RD and AxL in genu of CC. Therefore it is possible to argue that an impairment in the anterior part of the CC can be considered as a consequence of VaD.

Results obtained in ThR, even if did not show a specific alteration patterns like in PhG and CC, are useful in distinguishing between AD and VaD. Alterations in terms of MD, RD and AxL in this area emerged only in VaD (fig. 25). Considering these parameters, both comparing patients between them and with HC, a widespread impairment is generally found all over the brain. In ThR however, AD patients, differently from VaD, did not show any changes whit respect to HC. Interestingly, such structure resulted impaired in VaD also when compared with AD, therefore an increase of MD, RD and AxL in ThR seems to be VaD specific.

Considering to face the problem of distinguishing between patients group which diagnosis is uncertain, comparing such groups between them and with HC and checking anterior/posterior

alterations patterns in PhG and CC, alongside with changes of diffusivity magnitude in ThR could be helpful in clarify the diagnosis.

It is to note that we are aware that differentiating between AD and VaD is a tricky question and the obtained results need improvement and confirmations. However, these findings are a starting point for further analysis and can be used as inputs for the development of a machine learning approach.

Chapter 4: Tractography of the cortico-ponto-cerebellar pathway in human in vivo

Cerebellar involvement in cognition is increasingly recognized and is thought to depend on reciprocal connections with the cerebral cortex. Even if experiments in animals revealed that cerebro-cerebellar connections comprise cerebello-thalamo-cortical (CTC) and cortico-ponto-cerebellar (CPC) pathways, the CTC and CPC characterization in humans in vivo is still challenging. In this part of the thesis project, advanced MRI tractography was used to reconstruct the CPC pathway in human in vivo. Furthermore, quantitative indices were used in order to quantify the presence of streamlines in different cerebro and cerebellar cortical areas. Such quantitative description was used to investigate connectivity between cortical areas, both from anatomical and functional view point. Indeed, understanding functional and structural cerebro-cerebellar connectivity is crucial because comparing the results obtained in this study with the ones relative to the CTC pathway, difference in terms of cerebral areas reached by the two pathways suggests an asymmetry of the cerebro-cerebellar loop regarding cognitive tasks, while results during motor tasks suggest a symmetrical communication between the cerebrum and the cerebellum. The study presented in this chapter supports the hypothesis that once information has reached the cerebral cortex from the cerebellum via the CTC, communication involves serial processing between multiple cerebral cortical modules before information is sent back to the cerebellum via the CPC. Despite of, future studies are warranted to provide evidence supporting or rejecting our hypothesis.

4.1 Cerebro-cerebellar connectivity

Two main pathways have a key role in the cerebro-cerebellar connectivity: the CTC pathway and the CPC pathway (Voogd, 2003; Ramnani, 2006).The CTC pathway originates from the cerebellum and, passing through the superior cerebellar peduncle (SCP), reaches the contralateral cerebral cortex via synapses in the contralateral anterior-lateral nuclei of the thalamus (Kwon *et al.*, 2011). The CPC pathway originates from the cerebral cortex and, after descending through the ipsilateral cerebral peduncle (CP), makes synapses in the pontine nuclei and passes through the contralateral middle cerebellar peduncle (MCP) before reaching the cerebellum (Kamali *et al.*, 2010). Substantial evidence points to the CTC and the CPC pathways as the main components of the cerebro-cerebellar loop (fig. 26).

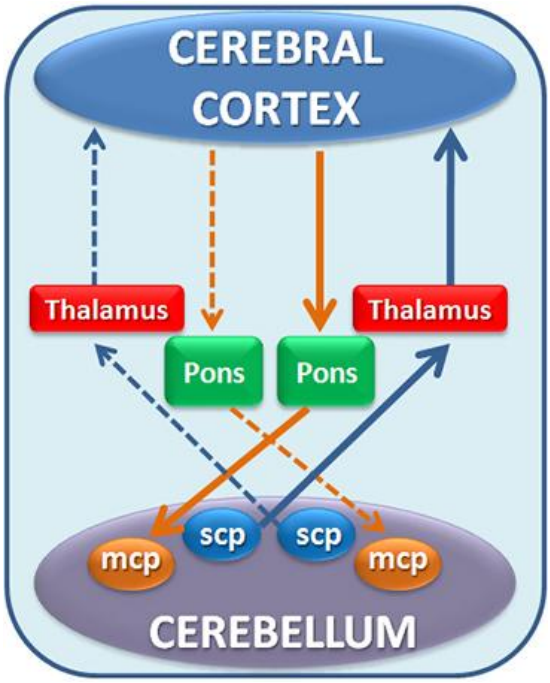

Figure 26 Schematic diagram of the cerebro-cerebellar loop. The cortico-ponto-cerebellar pathway (orange arrows) connects the cerebrum with the cerebellum passing through the pons and the contralateral middle cerebellar peduncle (MCP). The cerebello-thalamo-cortical pathway (blue arrow) connects the cerebellum with the cerebrum passing through the superior cerebellar peduncle (SCP) and the contralateral thalamus. Dotted arrows represent the contralateral pathway with corresponding colors.

Further information about the structure of this loop in humans *in vivo* could have implications in physiological, clinical and technical fields. From a physiological point of view, understanding the structure of the CTC and CPC pathways could give further information about the cerebellar contribution in motor learning and could give further evidence of cerebellar involvement in cognition. Indeed, while cerebellar involvement in motor control (Marr, 1969; Glickstein, 1992) has widely been discussed, its involvement in cognition is a recent matter of discussion (Leiner *et al.*, 1991; Schmahmann and Caplan, 2006). For what concerns the clinical implication of this study, abnormal functioning of the cerebro-cerebellar loop has been suggested to be involved in major neurological conditions such as dystonia, ataxia, hemiplegia, stroke and autism (Corben *et al.*, 2011; D'Angelo and Casali, 2012; Filip *et al.*, 2013; Fiori *et al.*, 2015).

Since the CTC pathway in human in vivo has already been reconstructed (Palesi et al. 2014), from this point onward the attention is focused on the CPC pathway. In order to study the CPC pathways in humans in vivo, advanced MRI techniques have been used, in particular diffusion weighted MRI (Basser and Jones, 2002), allowed to study specific pathways in humans in vivo with post processing methods such as tractography (Basser *et al.*, 2000). The whole, or a part of, CPC

pathway has been reconstructed using the diffusion tensor model (Habas and Cabanis, 2007; Kamali *et al.*, 2010; Jang *et al.*, 2014; Keser *et al.*, 2015; Morita *et al.*, 2015). Some of these studies (Kamali *et al.*, 2010; Jang *et al.*, 2014) were focused on CPC fibers division in relation to the cortical areas of destination. Whilst most of these MRI studies provided a visualization of projections through the MCP or the CP, they were affected by intrinsic limitations of the diffusion tensor model, such as its inability to resolve structures characterized by crossing fibers (Mori and van Zijl, 2002; Assaf and Pasternak, 2008; Tournier *et al.*, 2011). In order to overcome these limitations, advanced models of the diffusion process in vivo are needed, such as diffusion spectrum imaging (DSI) (Wedeen *et al.*, 2008), which was used to study the role of the MCP in intra cerebellar circuits in healthy (Granziera *et al.*, 2009) and pathological subjects (Lascano *et al.*, 2013). DSI though requires non-conventional acquisitions in order to reconstruct microstructural properties. An alternative approach that does not require hard changes in the acquisition (see next paragraph) consists of combining CSD (Tournier et al. (2007; 2011)) with probabilistic tractography. To our knowledge, only two publications (Fiori *et al.*, 2015; Sahama *et al.*, 2015) presented a successful reconstruction of the CPC pathway using CSD; anyway such studies were not focused neither in investigating cerebellar involvement in cognition nor in the method description.

Few studies have reported the presence of a convincing relationship between the CPC pathway and cognition (Salmi *et al.*, 2010; Sokolov *et al.*, 2014). One approach has been to rely on functional MRI (fMRI) results to first identify cerebral and cerebellar regions that are functionally connected, then to examine structural connections between those pre defined regions (Salmi et al. 2010; Sokolov et al. 2012, 2014). However, since with this approach specific cortical areas were used as targets, it may not be optimal in order to describe CPC pathway as a whole. In a previous study, we successfully reconstructed and quantified the efferent CTC pathway in healthy subjects in vivo without limiting cortical targets. We achieved this by combining high-angular resolution diffusion MRI data with advanced probabilistic tractography, using as seed region the SCP and as way point the red nucleus. The outcome showed that with this unconstrained CTC pathway reconstruction it was possible to assess the distribution of the target cortical regions reached by the efferent pathways from the cerebellum and establish a possible involvement of cognitive cortical areas (Palesi *et al.*, 2014). Therefore, mapping the CPC pathway too could give further information about both cerebro-cerebellar loop structure and cerebellar involvement in cognition.

The aim of this study is therefore to complement the findings from Palesi et al. (2014), by applying the same method used for the reconstruction of the CTC pathway, in order to verify whether: *(1)*

the CPC fibers can be properly identified by simply imposing their transit through the MCP and the contralateral CP; *(2)* there is a correspondence between cortical and cerebellar cognitive areas via the MCP, in a way that reciprocates the results found for the CTC pathway; *(3)* cerebro-cerebellar loop can be reconstructed by assessing the areas reached by the CPC and CTC pathways (Palesi *et al.*, 2014).

4.2 Reconstruction method

Two advanced diffusion techniques were used in this project in order to reconstruct the CPC pathway: CSD and track density imaging (TDI). CSD is useful to model multiple fibers within a voxel and to reconstruct pathway characterized by trans hemispheric decussation, while using TDI it is possible to obtain higher resolution and contrast than with classical DTI derived maps. Such super resolution maps allow to place seeds and target regions of interest (ROIs) more accurately than with fractional anisotropy or mean diffusivity maps. In order to use TDI maps high-angular resolution diffusion imaging (HARDI) data are necessary (Calamante *et al.*, 2010). Although HARDI data require more diffusion directions than in clinical applications, the sequence is feasible to acquire on a clinical scanner. A Philips Achieva 3T MRI scanner (Philips Healthcare, Best, The Netherlands) with a 32-channel head coil was used for the acquisition. The HARDI scan consisted of a cardiac-gated spin echo EPI sequence. The total scan time was about 20 minutes. The imaging parameters were TR ≈ 24 s (depending on the cardiac rate), TE = 68 ms, SENSE factor = 3.1, acquisition matrix = 96 x 112, 2 mm isotropic voxel and 72 axial slices with no gap. 61 non collinear diffusion directions were acquired with a b value of 1200 s/mm^2 (Cook *et al.*, 2007). For each set of diffusion weighted data, 7 volumes with no diffusion weighting (b = 0) were acquired. A whole brain high-resolution 3D sagittal T1-weighted (3DT1w) fast field echo (FFE) scan (TR = 6.9 ms, TE = 3.1 ms, TI = 824 ms, acquisition matrix = 256 x 256, 1 mm isotropic voxel, 180 sagittal slices, acquisition time 6 min 31 s) was acquired in order to have an anatomical reference.

Since one of the aim of this study was to compare results with those previously obtained by Palesi et al. (2014), in the study of the CTC, the same data from the same subjects were analyzed: 15 right handed healthy adults (7 males and 8 females; mean age 36.1 years and range 22–64 years) with no previous history of neurological symptoms.

In the following part of this paragraph, each step of the analysis pipeline is described. Diffusion data were analyzed using FSL (FMRIB Software Library, http://fsl.fmrib.ox.ac.uk/fsl/fslwiki/) and

MRtrix (http://www.brain.org.au/software/mrtrix/) software packages. 3DT1w data were post processed using FSL.

- Pre processing and data alignment: Eddy current artifacts and brain extraction (Smith, 2002) were performed using FSL. FLIRT algorithm from FSL was used in order to ally 3DT1w volumes to the diffusion data (Jenkinson *et al.*, 2002b). From this point onward such space will be considered as the subject's native space.
- Whole brain tractography and TDI maps: TDI maps were obtained performing whole brain tractography with an MRtrix algorithm able to combine CSD with probabilistic tractography (seed = whole brain, step-size = 0.1 mm, maximum harmonics order = 8, termination criteria: exit the brain or when the CSD fiber orientation distribution amplitude was < 0.1). Streamlines were randomly seeded throughout the whole brain until 2.5 millions tracks were selected (Tournier *et al.*, 2012). From these streamlines a TDI map was computed as the total number of streamlines passing within each element of a user defined 1 mm resolution grid (Calamante *et al.*, 2010).
- Cortico-ponto-cerebellar pathways: the CPC pathway was reconstructed using the MRtrix algorithm described in the previous step. Seed and a target ROI were placed in the MCP and the whole contralateral CP for each hemisphere respectively (Ramnani, 2006; Fiori *et al.*, 2015). A total of 3,000 streamlines for each subject were selected.
- Seed/target ROIs: Seed and target ROIs were placed using TDI maps. Seed ROI was defined as a sphere with 2.5 mm radius centered on the MCP in each cerebellar hemisphere and was identified in the coronal plane, as described by Calamante et al. (2010) (fig. 27a). Whereas the target ROI was traced on the whole contralateral CP (Ramnani, 2006) for each hemisphere, this structure was identified as the blue area (top-down fiber direction) on the axial plane of color coded TDI maps (fig. 27b).

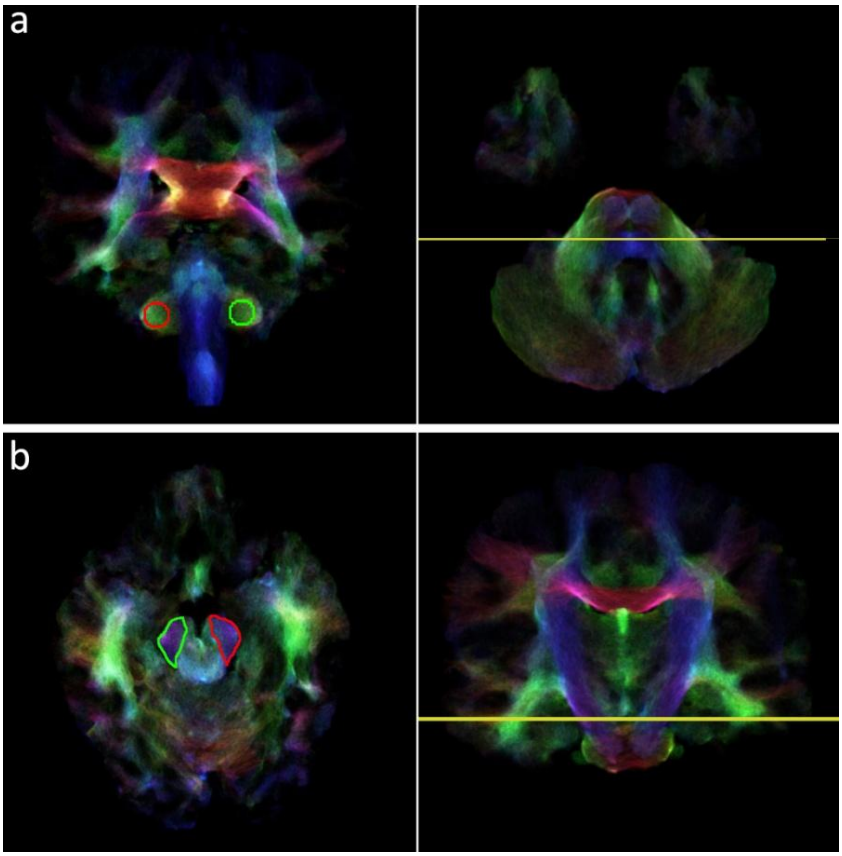

Figure 27 Seed and target ROIs drawn on color TDI map.(a) Seed ROIs placed in the coronal plane (left) on both right (red) and left (green) middle cerebellar peduncle at the level identified by the yellow line in the axial plane (right). (b) Target ROIs placed in the axial plane (left) on both right (green) and left (red) cerebral peduncle at the level identified by the yellow line in the coronal plane (right). The correspondence between each seed ROI and its contralateral target ROI is represented by the same color.

- Brain cortices parcellation: Cerebro and cerebellar parcellations (according to both anatomical and functional basis) were performed aligning the atlas of Brodmann areas (BA) and of the cerebellum (SUIT) (Diedrichsen *et al.*, 2009) to each subject's native space.

  Anatomical parcellation consisted of the following areas:

  - Cerebrum: prefrontal cortex, frontal, parietal, temporal, occipital and limbic lobes (Brodmann, 2006);
  - Cerebellum: anterior, VI, lateral Crus I–II, lobules VIIb/VIII and inferior lobules (Schmahmann *et al.*, 1999).

  Functional parcellation consisted of the following areas:

  - Cerebrum: motor, associative, primary sensory, primary auditory and primary visual areas (Brodmann, 2006);

- Cerebellum: primary motor, sensory motor and cognitive/sensory areas (Diedrichsen *et al.*, 2009).

- Quantification of $trGM_{cROI}$, $cROI_{tract}$ and TSC: In order to quantify the pattern of cerebro-cerebellar connections and to compare the CPC with the CTC pathway two previously defined metrics were used (fig. 28) (Palesi *et al.*, 2014). The $trGM_{cROI}$ index represents the proportion of the tract reaching a singular parcellation. It was calculated dividing the volume of grey matter (GM) reached by the tract (trGM) in one cortical parcellation by the total trGM across all cortical parcellations. The $cROI_{tract}$ index represents the proportion of a given ROI that is involved in the tract, and was obtained by dividing trGM in one cortical parcellation by the number of voxels within the parcellation itself. The total streamline count (TSC) was used to describe the number of the streamlines reaching the cortex. TSC was calculated applying the MRtrix filtering algorithm in order to obtain from the tract only the streamlines related to each parcellation.

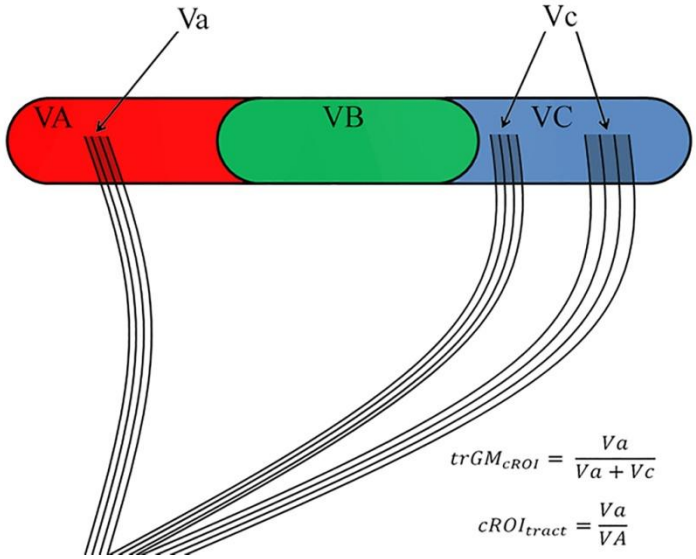

Figure 28 Tractography indices: trGMcROI, cROItract referred to ROI A (red). As an example a cortical parcellation with three ROIs is considered: ROI A; ROI B (green), reached by no streamline; ROI C (blue) reached by several streamlines. VA, VB, VC are the respective volumes, while Va, Vb=0, Vc represent the volume occupied by the streamlines (black lines in figure) impinging on the three ROIs, respectively.

- Mean cortico-ponto-cerebellar pathway: To assess the consistency of the pathways and for display purposes, the pathway obtained from all subjects were normalized to MNI space using FNIRT algorithm from FSL (non linear registration with nearest neighbor interpolation)(Klein *et al.*, 2009). Each subject normalized pathway was binarized

(tracks2prob algorithm from MRtrix) and the mean image was calculated (Ciccarelli *et al.*, 2003). Voxels intensity was proportional to the number of subjects with that specific voxel included in the mask. In the mean image were included only voxels common to at least 20% of subjects.

4.3 Results: cortico-ponto-cerebellar pathway analysis and quantification

A successful reconstruction of both left and right seeded CPC pathway was obtained combining CSD and probabilistic tractography. In figure 29a it is possible to note that by using only a ROI in the MCP the algorithm reconstructs both ipsilateral and contralateral fibers as well as fibers that run from one cerebellar hemisphere to the opposite one. Therefore, it is necessary to add another target ROI in the CP in order to reconstruct only fibers contralateral to the MCP (fig. 29b).

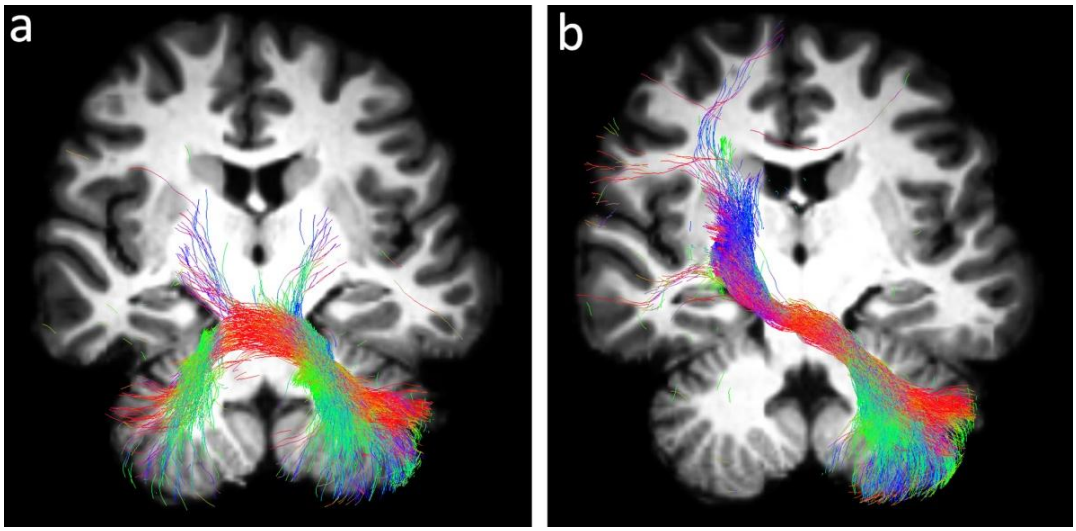

Figure 292D rendering of combined CSD technique and probabilistic streamlines tractography. Tracts in both left and right images are color coded according to the fiber direction (green = anterior-posterior, red = right-left, blue = feet-head). (a) Pathway reconstructed with only a seed ROI placed in the left middle cerebellar peduncle. (b) Pathway reconstructed with a seed ROI in the left middle cerebellar peduncle and a target ROI in the contralateral cerebral peduncle.

In figure 30 each pathway is shown with a single color to distinguish left from right seeded streamlines.

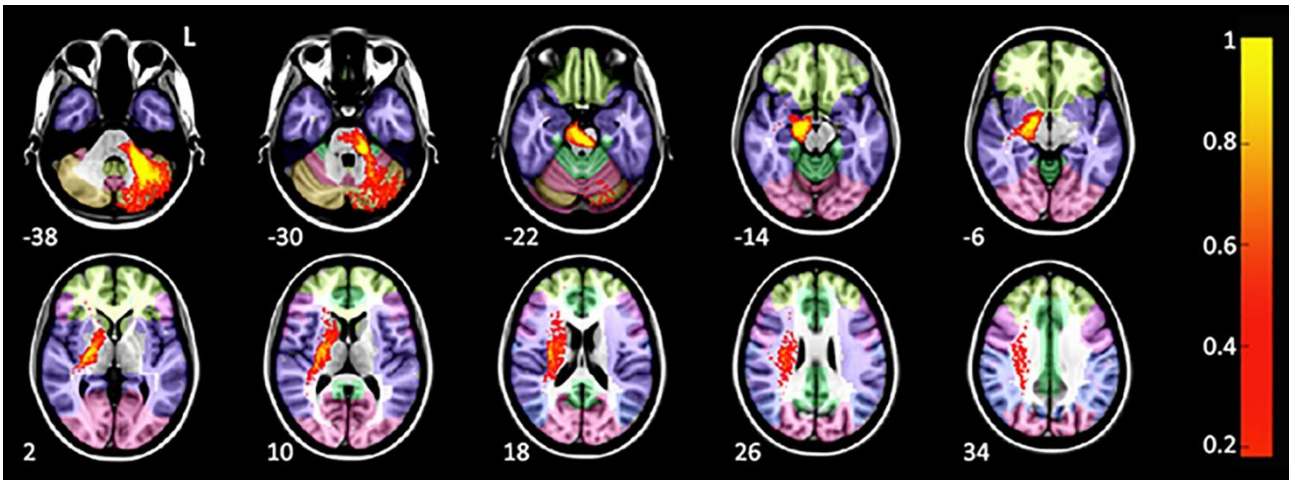

Figure 30 Extension of the left cortico-ponto-cerebellar tract (red-yellow) averaged across all subjects and normalized in the MNI space. Note major fiber density in temporal and frontal lobes and in Crus I-II. For clarity only left CPC tract is shown. Z coordinates are reported for each slice (mm). L = left side of the brain. The scale on the right represents the legend of the mean pathway color in terms of percentage of subjects.

In order to evaluate the extent of the mean CPC pathway from the cerebellum to the cerebrum figure 31 shows sections of the mean pathway across all subjects in MNI space, parcellated according to anatomical division. It is worth noting that the pathway does not enter the thalamus, but instead runs just outside this area, passing through the internal capsule (e.g. see figure 30: 2 and 10 mm MNI slices) (Glickstein *et al.*, 1985). Such characteristic of the pathway is important since indicates a correspondence with anatomical features found with ex vivo experiments on animals.

In table 2 and 3 are reported $trGM_{cROI}$, $cROI_{tract}$ and TSC values relative to anatomical and cortical parcellations respectively.

For what concerns cerebral and cerebellar anatomical parcellations, from table 2 it is possible to note that $trGM_{cROI}$, $cROI_{tract}$ and TSC have the highest values in the temporal lobe. In the cerebellum, the metrics have the highest values in the lateral Crus I-II.

Table 2 reveals some relevant correspondences:

- Overall, in the cerebellum the posterior-lateral areas (Crus I-II and lobules VIIb/VIII) are the ones most reached by the tract.
- $trGM_{cROI}$ has similar values in the lateral Crus I-II (62% ± 4%) and the temporal lobe (54% ± 6%).
- $trGM_{cROI}$ has similar values in lobules VIIb/VIII (24% ± 5%) and in the frontal cortex (20% ± 6%).

Structure	Anatomical Areas	$trGM_{cROI}$%	$cROI_{tract}$%	TSC
Cerebrum	Prefrontal Cortex	8(5)	1.1(0.6)	352(208)
	Frontal Lobe	20(6)	3.5(1.2)	888(269)
	Parietal Lobe	9(4)	1.9(1.3)	494(285)
	Temporal Lobe	**54(6)**	**3.8(1)**	**3355(816)**
	Occipital Lobe	6(2)	1.1(0.6)	446(160)
	Limbic Lobe	3(1)	1.1(0.4)	723(392)
Cerebellum	Anterior Lobule (I-V)	2(1)	2.5(1)	1017(515)
	Lobule VI	11(3)	15.2(4.1)	1420(327)
	Lateral Crus I-II	**62(4)**	**34.9(2.5)**	**4336(219)**
	Lobules VIIb/VIII	24(5)	22(5.8)	2286(450)
	Inferior Lobule(IX-X)	1(0)	2.3(1.3)	219(174)

Table 2: $trGM_{cROI}$, $cROI_{tract}$ and TSC values of cerebral and cerebellar cortical areas defined on anatomical bases, each value is averaged over left and right tract. Data are expressed as mean (SD) for each area. $cROI_{tract}$ percentage of each cortical region within the tract, $trGM_{cROI}$ proportion of the overall tract grey matter belonging to a specific cortical region, TSC total streamline count.

In table 3 are reported $trGM_{cROI}$, $cROI_{tract}$ and TSC values relevant to cerebral and cerebellar functional parcellations. Cerebrum associative areas have the highest $trGM_{cROI}$ and TSC values, while $cROI_{tract}$ has the highest value in the motor areas. Cerebellar cognitive/sensory area has the highest $trGM_{cROI}$, $cROI_{tract}$ and TSC values.

Table 3 reveals some relevant correspondences:

- In the cerebellum almost all streamlines of the pathway reach the cognitive/sensory area ($trGM_{cROI}$= 96% ± 1%).
- The associative areas of the cerebrum encompass the highest percentage of streamlines GM ($trGM_{cROI}$ = 69% ± 7%).
- Consequently about 70% of the pathway is likely to involve cerebral and cerebellar cognitive areas.

Structure	Functional Areas	$trGM_{cROI}$%	$cROI_{tract}$	TSC
Cerebrum	Motor Area	19(6)	**4.3(1.5)**	844(268)
	Associative Area	**69(7)**	2.5(0.6)	**3865(864)**
	Primary Somato-sensory	4(2)	3.4(2.1)	267(154)
	Primary Visual Area	6(2)	1.1(0.6)	446(160)
	Primary Auditory Area	2(1)	3.2(2.9)	119(97)
Cerebellum	Primary motor area	2(1)	2.5(1)	1017(515)
	Cognitive/Sensory Area	**96(1)**	**25.6(2.3)**	**5858(210)**
	Sensory-Motor Area	2(1)	11.4(3.3)	354(115)

Table 3: $trGM_{cROI}$, $cROI_{TRACT}$ and TSC values of cerebral and cerebellar cortical areas defined on functional bases, each value is averaged over left and right tract. Data are expressed as mean (SD) for each area. $cROI_{tract}$ percentage of each cortical region within the tract, $trGM_{cROI}$ proportion of the overall tract grey matter belonging to a specific cortical region, TSC total streamline count.

4.4 Hypothesis of cerebro-cerebellar connections

The main finding of this study is that at least 70% of the CPC pathway connects associative areas of the cerebral cortex to contralateral cognitive ones of the cerebellum, giving a further proof about cerebellar involvement in cognitive processing. The main metrics that we used to quantitatively describe the reconstructed pathway are the $trGM_{cROI}$ index (GM tract volume in one cortical parcellation relative to all cortical parcellations), the $cROI_{tract}$ index (GM tract volume in one cortical parcellation relative to the number of voxels within the same parcellation) and the total TSC index (the number of the streamlines reaching the cortex). The approach of this study has been to look for the involvement of cortical and cerebellar areas in the overall CPC pathway, rather than testing direct connectivity between regions.

As concerns the reconstruction method two key methodological choices have to be highlighted: high resolution TDI maps were used to draw seed and target ROIs, and a non tensor model (CSD algorithm) was combined with probabilistic tractography in order to resolve the crossing fiber problems. The former choice was adopted since it allows to draw ROIs with higher accuracy than classical DTI based maps, while the latter allowed the reconstruction of streamlines starting from the MCP and developing into contralateral tracts. It is to note that ROIs were placed in peduncles (MCP and CP), therefore streamlines were free to reach whatever cerebral and cerebellar cortical areas. The areas reached by the reconstructed CPC pathway are mostly in agreement with the anatomical findings of *ex vivo* experiments (Voogd, 2003). Figure 30 shows that the pathway does not enter the thalami but run across to the internal capsule as reported in tracers studies (Glickstein *et al.*, 1985; Schmahmann and Pandya, 1997).

The metrics previously described were used to quantify how different GM areas are involved in the reconstructed pathway. Comparing the values of such indices from cerebral and cerebellar cortical parcellations allowed us to make some observations about the CPC pathway.

The reconstructed CPC pathways reach mainly the temporal and frontal cortex of the cerebrum, while in the cerebellum the majority of streamlines terminates in lateral Crus I-II and lobules VIIb/VIII (table 2). Looking at the results obtained of the anatomical parcellations there are some interesting index correspondences.

Results suggest a similar involvement of the lateral Crus I-II and the temporal lobe ($trGM_{cROI}$ was 62% ± 4% and 54% ± 6% respectively), which could reflect a connection between these areas or the ability of a functional integration. Temporal lobe connection to the cerebellum and its involvement in the cerebro-cerebellar loop has been largely discussed (D'Angelo and Casali, 2012; Baumann *et al.*, 2015). Although the exact nature of the connections between temporal areas and the cerebellum is still debated. Ex vivo studies, though, in non-human primates support the presence of direct projections from the superior temporal sulcus to the pons (Brodal, 1978; Glickstein *et al.*, 1985; Schmahmann and Pandya, 1991) and from the pons to the cerebellum (Brodal, 1979; Glickstein *et al.*, 1994). Further proof about direct temporal lobe connections to the cerebellum is given by other experiments on animals (Heath and Harper, 1974) in which cerebellar fastigial nuclei project to several temporal areas. For what concerns studies on humans, significant functional connectivity between cerebellum and temporal areas was found using fMRI (Krienen and Buckner, 2009; Habas *et al.*, 2011; Dobromyslin *et al.*, 2012). Dynamic casual modeling also provided a strong bidirectional connection between the temporal lobe and the cerebellum (Booth *et al.*, 2007). From a structural point of view, some tractography based studies have shown no direct connections between the temporal lobe and the cerebellum (Ramnani, 2006) but this perhaps, at least in part, reflects the difficulty of following the high curvature of the cerebello temporal connections. Sokolov et al.(2014), using tractography based on seed and target ROIs derived from fMRI studies, reported the existence of a bidirectional connection between the superior temporal sulcus and the cerebellar lobule Crus I. Therefore, our results are in accordance with the large consensus about a common involvement of both lateral Crus I-II and temporal lobe in multimodal cognitive functions (Sokolov *et al.*, 2012; Baumann *et al.*, 2015). Our metrics were able to provide a quantitative description of the correspondence of temporo cerebellar involvement in humans in vivo.

The frontal cortex was the area with the second highest $trGM_{cROI}$ value in the cerebrum. Such result is in agreement with virus tracers experiments where BA 4-6-8 project a large quantity of fibers to the pons (Glickstein *et al.*, 1985). Since frontal area M1 is known to project to the pons and then to the cerebellum (Kelly and Strick, 2003), the high $trGM_{cROI}$ value agrees with cerebellar involvement in motor control. Furthermore, there is a correspondence of $trGM_{cROI}$ values between the frontal cortex and lobules VIIb/VIII, with values of 20% ± 6% and 24% ± 5% respectively. Literature reports the involvement of lobules VIIb/VIII are known in sensory motor and cognitive functions (Stoodley, 2012). Ex vivo and in vivo studies report the existence of connection between the frontal cortex and lobules VII/VIII. Ramnani (2012) reported that lobules V, VI, VIIb and VIIIa are related to the primary motor cortex in both humans and non-human primates. Kelly and Strick (2003), injecting H129 strain ofHSV1 in a part of the frontal cortex, reported that the granule cells of lobule VIII receive input from the frontal area related to arm control. fMRI experiments showed that activations associated with the right hand movement are localized in the right lobule V with a secondary representation in the right lobule VIII (Grodd *et al.*, 2001). A meta-analysis of right-handed finger-tapping studies revealed activation peaks in right lobules V–VI and lobules VIIIa and VIIIb (Stoodley and Schmahmann, 2009). There are also studies reporting cerebellar activation in lobules VII during cognitive tasks (see Stoodley and Schmahmann(2009, 2010) for reviews). Altogether these findings support the involvement of the CPC pathway in the direct connection of the frontal cortex with cerebellar lobules lobules VIIb/VIII.

The low $trGM_{cROI}$ value (8%) in the prefrontal cortex parcellation is probably due to its position with respect to the target ROI. Indeed, tractography algorithms are biased towards the reconstruction of pathways characterized by shorter streamlines with lower curvature, such as those going from the CP to the temporal lobe. There are a number of studies supporting prefrontal cortex projections to the cerebellum both in animals and humans (Krienen and Buckner, 2009; Stoodley, 2012). It is therefore possible that our reported $trGM_{cROI}$ index reflects an underestimation of the streamlines connecting these areas.

Looking at the results relevant to functional parcellation, as already said, there is a high cerebro-cerebellar cognitive involvement. In fact, the main finding (table 3) is that the cognitive/sensory hemispheres of the cerebellum and the cortical associative areas encompassed 96% and 69% of the tract GM, respectively, supporting the hypothesis that lateral areas of the cerebellum are involved in higher cognitive processes (Habas *et al.*, 2009; Strick *et al.*, 2009; Watson *et al.*, 2014).

The functional parcellation with the second highest $trGM_{cROI}$ value (19% ± 6%) is the cerebral motor area. Such finding is in accordance with cerebellar involvement in motor control. Even if cerebellar influence in motor task has already been largely discussed (Marr, 1969; Glickstein, 1992) such results compared with the one obtained in the CTC study (Palesi et al. 2014) acquires an interesting role in the loop reconstruction. An interpretation is given in following section, when our results are discussed in comparison with existing cerebro-cerebellar models (Ito, 2008).

The primary auditory and visual cortices only constitutes 2% and 6% of the tract connected GM, respectively. These values are in accordance with fMRI studies showing that primary auditory and visual cortices do not appear functionally connected with the cerebellum (Buckner *et al.*, 2011). On the other hand, an underestimation of these streamlines due to their relative position with respect to the cerebellum, has to be considered. As already discussed by Buckner et al. (2011) the high curvature of fibers connecting the cerebellum with visual and auditory areas (located in the occipital and temporal lobes, respectively) could make them hard to detect by tractographic methods. The cerebrum somato-sensory area constitutes only 4% of the CPC pathway. Since works based on functional connectivity reported an existing network between the cerebellum and this cerebral area (Buckner *et al.*, 2011), further studies with new analysis methods (Smith *et al.*, 2012, 2013, 2015a) could help to clarify the value we found.

It is to note that all the hypotheses, made in this paragraph about cerebro-cerebellar connections, are not to be intended as an alternative to previous anatomical findings, but as a way to give a further proof about the existence in human in vivo of some direct connections between cerebral and cerebellar cortices. Every hypothesis does not rely only on the indices values but is also reflected by previous studies. Obtained results could be improved by exploiting recent developments in diffusion MRI tractography methods (Smith *et al.*, 2013, 2015b) and by repeating the analysis using higher resolution data, such as those available through the Human Connectome Project (Uğurbil *et al.*, 2013; van Baarsen *et al.*, 2016). In this way would be possible to clarify or confirm some interpretation related to our result relying not only on literature but on a quantitative analysis.

We are aware about main tractography limitations: impossibility to determine fiber direction and to not reach a resolution comparable with axon dimension (Jones *et al.*, 2013). There are also studies reporting that tractography algorithm can produce an high number of false positive tracts (Descoteaux *et al.*, 2016). Anyway, the basis of this work rely on solid anatomical findings (ROIs in

the MCP and the CP) and the chosen reconstruction method that is the one more suitable to reconstruct contralateral pathways. Beside all its limitations, actually tractography is the only method able to reconstruct cerebral pathways in humans in vivo; therefore if associated with strong anatomical knowledge and efficient method it allows to develop new and interesting hypotheses.

4.5 Involvement of the pathway in the cerebro-cerebellar loop

Cerebro-cerebellar connection has been thought to have a main role in motor control and, only recently, to be involved in cognitive processing. Generally, the scheme of such connection is composed of two main ways, one that goes from the cerebellum to the cerebrum (CTC) and another that runs through the opposite direction (CPC) (Schmahmann and Pandya, 1997; Voogd, 2003). Because of its connections with the cerebral cortex, the role of the cerebellum with respect to the cerebrum is to act as an information processing system that modulates its activity (Ramnani, 2006). According to the error correction model, the cerebellum receives input from the cortex via the CPC pathway and modulates cerebral processing via the CTC pathway (Marr, 1969; Ito, 2006). Initially, such model was supposed to be just related with the cerebellar role in motor control. In the last years, in accordance with the growing evidence of cerebellar implications in cognition, the cerebellum is supposed to modulate not only motor functions but also cognitive ones.

As explained in paragraph 4.1 one of the scope of this work was to verify if, using diffusion based tractography, it is possible to reconstruct and quantitatively describe the cerebro-cerebellar loop in human in vivo trying to hypothesize which cortical areas are mainly involved in the communication between the cerebrum and the cerebellum. In order to investigate the cerebro-cerebellar loop, the results obtained for the CPC pathway are compared with the ones obtained for the CTC pathway (Palesi et al. 2014)(fig. 31).

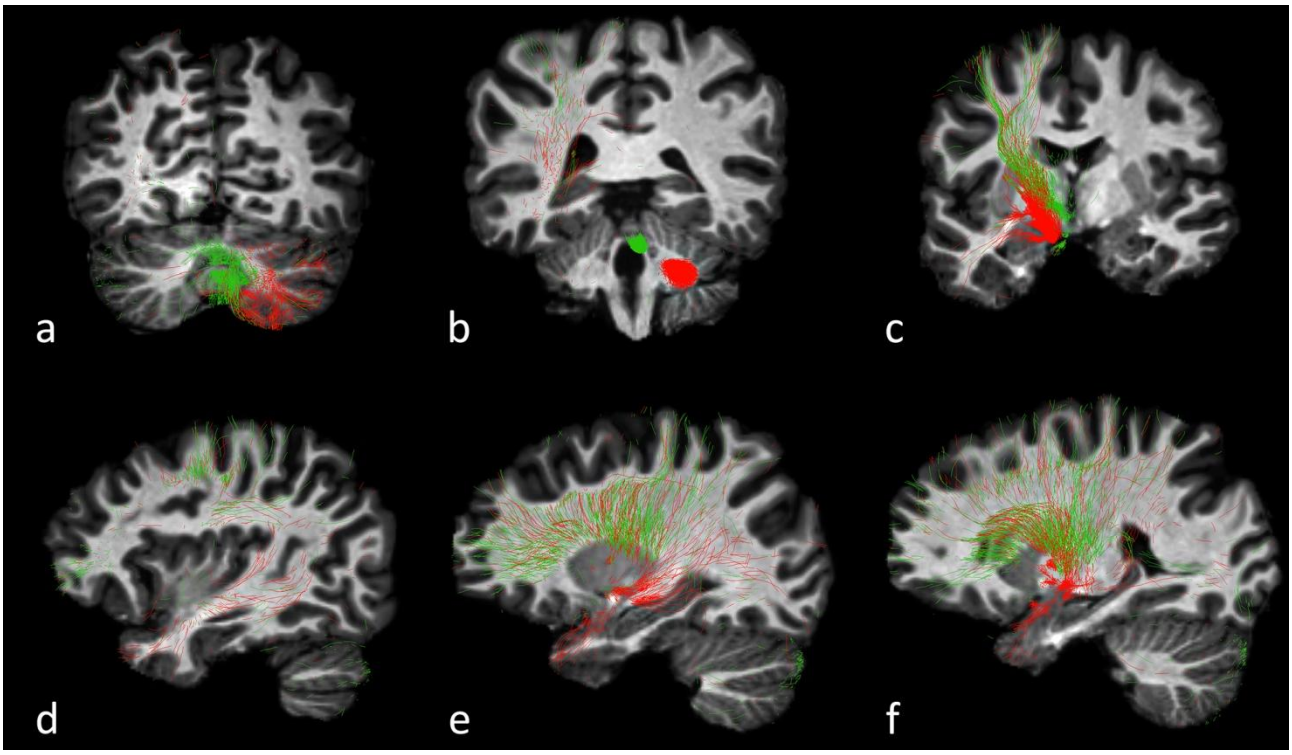

Figure 31 Left seeded cortico-ponto-cerebellar tract (red) and cerebello-thalamo-cortical tract (green) of a representative subject. In the cerebellum pathways occupy mainly lateral Crus I-II and lobules VIIb/VIII (a), while outputs from the cerebellum (b) are different. In cerebral areas they partially overlap in the frontal lobe (b ,d ,e). The temporal lobe is reached more densely by CPC streamlines than CTC ones, while in the prefrontal cortex there are more CTC than CPC fibers (d, e, f).

Looking at $trGM_{cROI}$ values associated to functional areas (table 3) it is possible to note that both CTC and CPC pathways are strongly reaching cognitive ones, about 80 and 70% respectively (see table 3 in Palesi et al. (2014) for CTC $trGM_{cROI}$ values). In contrast, $trGM_{cROI}$ values associated to anatomical parcellations show that the proportion of CTC and CPC streamlines, reaching anatomically defined areas (table 2), is not similar (see table 2 in Palesi et al. (2014) for CTC $trGM_{cROI}$ values). Whereas CTC streamlines reach the prefrontal cortex more than other areas, CPC streamlines mostly involve the temporal lobe. On the other hand, there was a good agreement of the proportion of the frontal cortex involved in both pathways, which is in line with virus tracers' studies, which showed that frontal areas, such as the primary motor area M1, send projections to the cerebellum through the pons and receive cerebellar projection through the thalamus (Kelly and Strick, 2003; Ramnani, 2006).

For what concerns the cerebellum, even if the absolute $trGM_{cROI}$ values of corresponding anatomical areas are not identical between the CTC and CPC pathways, there is a correspondence in terms of the main encompassed GM parcellation. Indeed, the anterior part of the cerebellum

(lobule I-V) is poorly reached by both CPC and CTC streamlines. On the other hand, both afferent and efferent cerebro-cerebellar pathways show a high percentage of streamlines in lobule VI, lateral Crus I-II and lobules VIIb/VIII. In particular, both pathways show that the most involved cerebellar lobules are the ones assigned to cognitive functions (Stoodley, 2012).

Areas where the $trGM_{cROI}$ index has the greatest difference between the pathways are the temporal lobe and the prefrontal cortex, with a much greater involvement of the temporal lobe in the CPC pathway and of the prefrontal cortex in the CTC one. If this was to be a true anatomical feature of the cerebro-cerebellar loop, these results suggest that in the temporal lobe there are more efferent than afferent fibers, while in the prefrontal lobe there are more afferent then efferent fibers. Since the cerebro-cerebellar connections are considered as a loop where the information goes from the cerebral cortex to the cerebellum and vice versa, we argue that there must be a connection between the prefrontal cortex and the temporal lobe to close this loop, as recently discussed (Simons and Spiers, 2003). Functional connections between these two areas were reported in studies with both EEG and fMRI, where the prefronto-temporal circuit was found to mediate novel verbal episodic encoding and working memory (Kirchhoff *et al.*, 2000; Burgess *et al.*, 2001; Axmacher *et al.*, 2008). Regarding structural connections between these areas, both histological and MRI based studies describe the uncinate fasciculus as a bidirectional connection pathway between the temporal lobe and the prefrontal cortex (Schmahmann *et al.*, 2007; Catani and Thiebaut de Schotten, 2008). The uncinate fasciculus is also supposed to serve as a conduit for prefrontal cortex fibers to join other WM bundles such as the cingulum, corpus callosum and superior longitudinal fasciculus (Lehman *et al.*, 2011; Jbabdi *et al.*, 2013).There are also other hypotheses on the prefronto-temporal connection, which involve other WM bundles alongside the uncinate fasciculus, such as the fornix and the parahippocampal cingulum (Metzler-Baddeley *et al.*, 2011). The fornix connects the hippocampal formation to the prefrontal cortex (Poletti and Creswell, 1977), while the parahippocampal cingulum includes fibers that link the hippocampal formation with the cingulate cortex (Vann *et al.*, 2009), thereby providing a second route for fronto-temporal interactions. Considering the total number of WM tracts in the human brain, multiple pathways could be hypothesized for the prefronto-temporal connection. Consequently the information could be exchanged through a single tract or a pathway involving a combination of WM bundles and synapses between the temporal lobe and the prefrontal cortex.

An alternative approach to analyze the interaction between cerebrum and cerebellum is to compare our results with already existing cerebro-cerebellar "models". According to Marr (1969)

the cerebellar cortex is supposed to act like a storage for neural representations of body movements, acquired through learning; such representations are called "internal models". The interaction between the cerebellum and the cerebral cortex is based on the "recall" of internal models, with a forward or an inverse based “control” system (Kawato *et al.*, 1987; Ito, 2008). The forward model is supposed to be predominant before learning, while, as the learning progresses, the inverse model is predominant. Even if both the forward and the inverse model were hypothesized in order to describe cerebellar involvement in motor control, as the cerebellar role in cognition has become more evident, they were generalized from motor execution to motor planning and cognitive control. As for motor control, internal models are supposed to have a key role also in cognition, therefore, at first the cerebral cortex seems to be playing a key role in elaborating new thoughts; then, as the thoughts become more usual the cerebellum takes over recalling the cortex internal models. According to the model proposed by Ito (2008), during cognitive tasks, the prefrontal and the temporal cortex have a key role in the interaction with the cerebellum both in the forward and in the inverse model. As previously described, our results are indicating that there are possible pathways between the temporal and the parietal lobe, as hypothesized in the cognitive model of the cerebro-cerebellar loop (Ito, 2008); the role of such connections could be to facilitate prefrontal cortex modulation of mental models encoded in the temporal and parietal cortices. Therefore, cerebellar connections with these brain regions could be assumed to be needed for automatization of information processes, through a continue error evaluation, which, in the case of new thoughts would leads to generating new internal models.

With regard to the motor control, as described in the cerebro-cerebellar model, the motor cortex (which is located in the frontal lobe) is the one with major influence in the loop. The correspondence of $trGM_{cROI}$ values, found in the frontal cortex between the CPC and CTC pathways, is in accordance with the theory proposed by Ito (2008); therefore we argue that in motor processing the interaction between the cerebrum and the cerebellum (internal models application and error evaluation) is mainly relying on the portion of the loop directly connecting the cerebellum and the frontal cortex.

In summary, the comparison of tractography results in the context of the cerebro-cerebellar models theory, leads to argue that in the cerebro-cerebellar loop it is possible to discern connections assigned to motor control from connections assigned to cognitive functions. In particular, during motor tasks the frontal cortex is the main area involved, whereas when the brain is solving cognitive tasks an interaction between the cerebellum and multiple cerebral areas is

necessary, leading to a major involvement of CPC and CTC pathways in connecting areas known to be related to cognition.

Chapter 5: Implementation and application of a zoom diffusion weighted sequence

As explained in the previous chapters diffusion based MRI has an important value both in research and clinical fields. Different tractographic techniques, as well as diffusion derived parameters have been largely adopted in the study of different pathological cases in order to have useful and previously unavailable information. New diffusion models and post processing techniques are continuously developed to improve the quality of the results and obtain bigger and more reliable number of information from diffusion images. Despite all these applications and improvements related to diffusion MRI, the poor quality of available diffusion images in some areas (both brain and body) often reduces the potential of this technique and restricts clinical applications to certain regions. Therefore, an improvement of spatial resolution is highly desirable. In this chapter the development is described of an MRI sequence, able to acquire a small body area with higher resolution (ZOOM), applying a technique based on non-coplanar excitation (90°) and refocusing (180°) pulses. By applying ZOOM technique it is possible to increase SNR and therefore to reach higher in plane resolution than with standard sequences. A standard slice selection never permits zooming; in case a limited FOV was selected, spatial aliasing would occur due to discrete Fourier transform properties. Zooming technique do overcome this issue by activating an echo only in a selected region, by non coplanar excitation and refocusing.

Data acquired with the developed sequence were compared with the ones acquired with an already existent sequence (ZOOMit, property of Siemens) that uses a different technique to reach the same scope. At the end of this chapter some preliminary results are also reported, obtained in human in vivo with a 9.4T MRI scanner.

5.1 Zoom: theory and advantages

DTI and DWI have a notable clinical interest since provide non invasive information about structural integrity and alterations of neural tissue. Further investigations of diffusion characteristics in neural structures may give new information about various pathologies (e.g. spinal cord injury or AD). Precise localization of lesions, as well as a more accurate definition of particular WM structures in terms of diffusion derived parameters, will allow a more accurate

description of pathologies, consequently giving more opportunities to both clinical and research fields.

In order to reach the goals described above, it is necessary to acquire data with resolution as higher as possible. However, the resolution is inherently limited by the SNR; such limitation leads to acquire data with higher field (from 3T onward) in order to reach higher resolution and at the same time, increasing the SNR. Other issues that affect image quality are physiological motion and susceptibility effects. These problems mainly depend on the readout technique used. Single shot EPI techniques have a lower motion influence and higher SNR efficiency with respect to other readout techniques. On the other hand, inhomogeneities due to static field (that linearly increase with the scanner strength) cause phase errors during the readout part of the sequence and consequently, the acquired image results distorted. In order to avoid these distortions it is possible to use other readout techniques such as turbo spin echo, line scan and stimulated echo acquisition mode (Gudbjartsson *et al.*, 1996; Nolte *et al.*, 2000; Tsuchiya *et al.*, 2003). These techniques however do not allow reaching high SNR as with single shot EPI. The best way to have high SNR and at the same time to avoid susceptibility distortions is to use EPI sequences with a short readout time. Techniques like segmented EPI and parallel imaging has been applied to reduce the readout time, anyway they suffer from some problems like complexity of physiological motion in case of segmented EPI or patient geometry restriction in case of parallel imaging (Cercignani *et al.*, 2003; Tsuchiya *et al.*, 2005; Holdsworth *et al.*, 2008).

Possible alternatives to the techniques described above are the spatially reduced FOV single shot EPI approaches. These approaches have shown good results, in terms of high SNR and low artifacts, for diffusion imaging of regions limited in one dimension. Different modalities have been used to implement reduced FOV sequences (non-coplanar spin echo (SE) selection (Feinberg *et al.*, 1985; Wheeler-Kingshott *et al.*, 2002), two dimensional selective pulses (Rieseberg *et al.*, 2002), outer volume suppression (OVS) (Wilm *et al.*, 2007)). For SE sequences, the reduced FOV is obtained by applying non-coplanar excitation (90° RF pulse) and refocusing pulses (180° RF pulse). Consequently, only the spins contained in the volume defined by the intersection of the two slices excited by the RF pulses are both excited and refocused, thus eliciting an echo at TE. Feinberg et al. (1985) initially applied this technique. However, for multiple slice acquisitions, this technique would lead to signal loss and artifacts. Wheeler-Kingshott et al. (2002) proposed a method that combines the line scan with an EPI readout. Here the 180° pulse is applied obliquely with respect to the imaging plane defined by the 90° pulse, thereby a FOV reduction is achieved within a

rhomboidal region (rhomboidal shape is caused by two transition bandwidths (Tb), due to a partial alignment of the two RF pulses, in the phase encoding direction). In order to suppress Tb, Wilm et al. (2009) used OVS technique. Here, the same theory of Wheeler-Kingshott et al.(2002) is adopted. Instead of OVS (that implicate longer acquisition time), it was preferred to control every sequence parameter (see next paragraphs) in order to have a prior knowledge of Tb dimensions and be able to delete them during post processing.

5.2 Implementation

Figure 32 schematically shows the structure of the sequence able to acquire a reduced FOV. During the 90° RF pulse, in addition to the slice selection gradient, another one is applied in the phase encoding direction, while, during the 180° RF pulse, only the slice selection gradient is applied. In this way, if the readout direction is set as transversal, the slice relevant to the refocusing pulse (180°) is perpendicular to this direction, whereas the one excited by the 90° RF pulse is tilted by an angle dependent on intensity and duration of the combination of phase encoding and slice selection gradients.

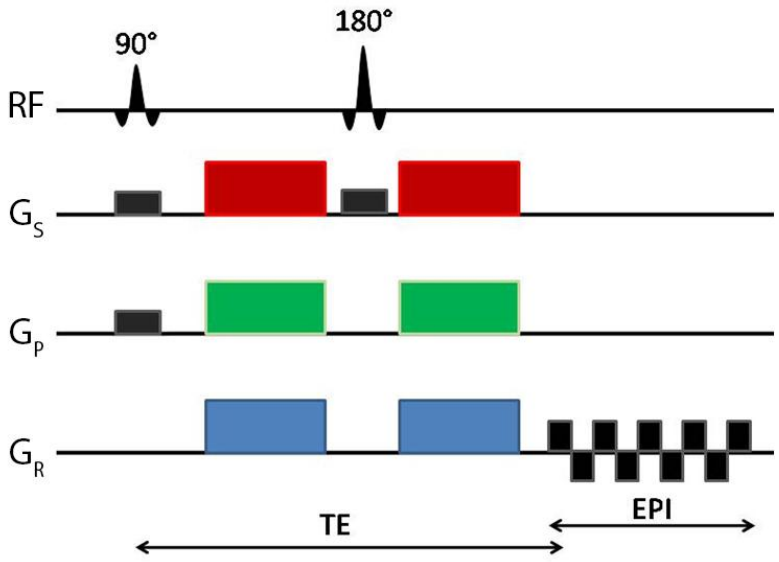

Figure 32 Schematic representation of the developed sequence. RF and gradients (slice selection Gs, phase encoding Gp, readout Gr) are shown in each line. Tilting of the 90° pulse is obtained by an additional gradient in the phase encoding direction during the 90° slice selection.

Since 90° and 180° RF pulses are not coplanar applied (the slice excited by the 90° RF pulse is tilted with respect to the one excited by to 180° one), only the spins contained in the volume defined by the intersection of the two excited slices (inner volume (IV)) are completely refocused (pink area in figure 33). As a consequence, the signal originates only from this region, with the exception of other two areas. Indeed, in the phase encoding direction, there are two Tb where the spins are partially excited (green areas in figure 33). Here, the slice excited by the two pulses partially overlaps within a measure dependent on the tilt angle and slice thickness.

In this part only the theory relative to the implementation is given. Further on, a detailed description is provided of the values for the acquisition and how they have been chosen.

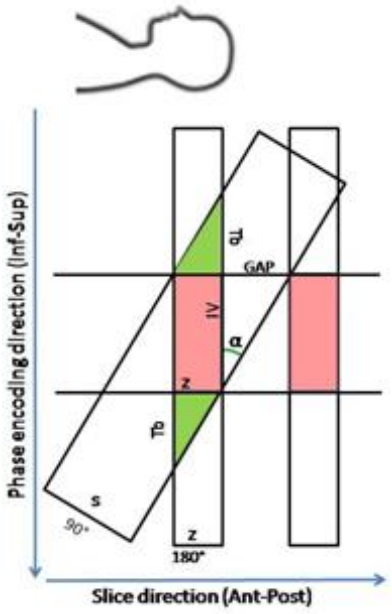

Figure 33 Schematic representation of FOV reduction theory. Each rectangle in the figure represents a slice. Pink areas represent the inner volume (IV). Green areas are the transition bandwidths (Tb) where the spin are partially excited. s = thickness of the slice excited by the 90° pulse. z = thickness of the slice excited by the 180° pulse. α = angle between the 90° and the 180° RF pulses.

As it is possible to deduce from the figure above, a desirable rectangular FOV (without transition bandwidth) will be achieved if the 90° and the 180° RF pulses are perpendicular to each other. Since the slice-to-slice time is significantly shorter than the repetition time TR, a perpendicular application of the two pulses would saturate also slices that are not meant to be excited, causing low signal and artifacts. For this reason, it is necessary to tilt the 90° pulse by an angle smaller than 90°. Even using an angle smaller than 90°, there will be regions where neighbor slices are excited.

In order to avoid exciting unwanted slices, it is necessary to leave a GAP between them. As a consequence, in order to acquire a continue volume it is necessary to repeat the acquisition more than once. In the example reported in figure 34 the whole volume (60 mm long in the slice selection directions) is acquired using three different groups of slices (each slice is 4mm thick and the gap between two slices, belonging to the same group, is 8 mm).

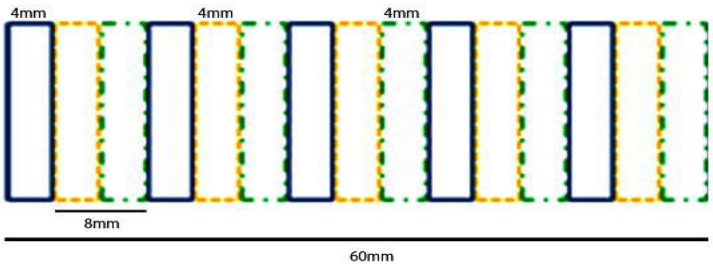

Figure 34 Schematic representation of slice order acquisition. Each color represents a group of slices. Slice thickness 4mm, gap between slices 8mm, total acquire thickness 60mm. In this example, in order not to excite contiguous slices, the whole volume is acquired by repeating three times the sequence (one time for each slice group).

There are different solutions to eliminate the unwanted Tb (e.g. Wilm et al. (2009) applied OVS technique). Here, in order to reduce the total acquisition time, we decided not to use any of these techniques but to control acquisition parameter so that the Tb do not influence the quality of the image and can be deleted during post processing (in the next paragraph acquisition parameters are reported).

Until now, the theoretical concepts about reduced FOV theory and acquisition have been given, in the following part of the paragraph the formula for calculating acquisition parameters is described.

As already reported, the dimension of the IV depends on various parameters. With reference to figure 33, the tilt angle α is given by:

$$\alpha = arctg(\frac{GAP}{IV})$$

where GAP is the distance between two consecutive slices belonging to the same group (8 mm in the example of figure 34) and IV is the desired dimension, in the phase encoding direction, of the reduced FOV.

The length, in the phase encoding direction (Tb_{phe}), of each transition bandwidth is:

$$Tb_{phe} = \frac{z}{\tan \alpha}$$

where z is the thickness of the slice refocused by the 180° RF pulse.

Once that α and Tb dimensions are known, it is possible to calculate the thickness of the slice excited by the 90° RF pulse:

$$s = \sin \alpha \ \left(IV + Tb_{phe}\right)$$

Considering that the desired IV is 26 mm in the phase encoding direction, the slice thickness 4 mm and the GAP 8 mm (we suppose to acquire 3 slice groups therefore the GAP is two times the slice thickness), by applying the reported formulas the tilt angle is α ≅ 17°, each transition bandwidth is Tb_{phe} ≅ 13 mm and the necessary thickness of the slice excited by the 90° RF pulse is s ≅ 11 mm. As explained in the next paragraph, once known these parameters, it is possible to set the proper acquisition parameters, in order to acquire the reduced FOV without aliasing artifacts.

Code implementation

Even if it is not easy to understand code implementation without the whole script, in this paragraph section for completeness, the main changes made to the sequence's code are briefly described. The modified code (C++) derives from a diffusion spin echo EPI package (DWI-SE), property of Siemens. The original sequence, implemented in the package, does not allow to add a phase encoding gradient to the slice selection one during the 90° RF pulse. Therefore, parts of the code were modified in order to make the sequence able to tilt only the 90° pulse. It was also necessary to modify the code in order to have different thickness between the slices relevant to the 90° and 180° RF pulses. In the following part each step is briefly described and schematically reported in figure 35.

- **Rotation matrix:** The sequence is "organized" according to two reference systems: one is the physical coordinate system, defined by x, y, and z axes. Standing in front of the scanner and looking at it, the axes are defined:
    - x-axis points from left to right;
    - y-axis points from down to up;
    - z-axis points from rear to front (towards you).

  The other reference system is the one of the gradients. In order to pass from the gradient reference system to the physical one, it is necessary to apply a rotation matrix (R):

$$\begin{bmatrix} x \\ y \\ z \end{bmatrix} = R \begin{bmatrix} G_{phase} \\ G_{readout} \\ G_{slice} \end{bmatrix}$$

In the code, each pulse has its own rotation matrix that defines the orientation of the pulse (with respect to the scanner reference system) and consequently the gradients that are applied together with the pulse. When the 90° pulse is applied perpendicular to the slice direction (feet to head) and the phase encoding direction is set as anterior-posterior R is:

$$R = \begin{bmatrix} 0 & -1 & 0 \\ -1 & 0 & 0 \\ 0 & 0 & -1 \end{bmatrix}$$

In order to obtain the reduce FOV was necessary to tilt the 90° RF pulse around the x axis (see above for x axis orientation). Therefore the rotation matrix R was multiplied by an x-rotation matrix.

$$R = \begin{bmatrix} 1 & 0 & 0 \\ 0 & cos\alpha & -sin\alpha \\ 0 & sin\alpha & cos\alpha \end{bmatrix} \begin{bmatrix} 0 & -1 & 0 \\ -1 & 0 & 0 \\ 0 & 0 & -1 \end{bmatrix}$$

In this way the reference system relative to the 90° pulse is tilted with respect to the 180° one (fig. 35a) and the scanner adds a gradient in the phase encoding direction only during the first pulse.

- **Slice object:** Each RF pulse has his own slice object (the terms "object" is to intend in the C++ way) which contain all information relative to the excited slice. Since the 90° RF pulse rotation matrix was changed the slice object relevant to this pulse was centered to a different reference system with respect to the 180°RF pulse slice object. In order to have the center of the excited and refocused slices in the same position, the 90° slice object coordinate was shifted in phase and slice selection directions, by translating its coordinate to the plane defined by the 180° rotation matrix (fig. 35 d).
- **Special card:** Since the original code is not mean to acquire a reduced FOV, in the user interface there isn't any part where the user can enter the necessary parameters. Therefore, a special card (special card is the Siemens term to indicate an additional windows that can be added to the user interface) was added in order to allow entering the desired IV, the angle between RF pulses and the thickness of the slice excited by the 90° pulse.

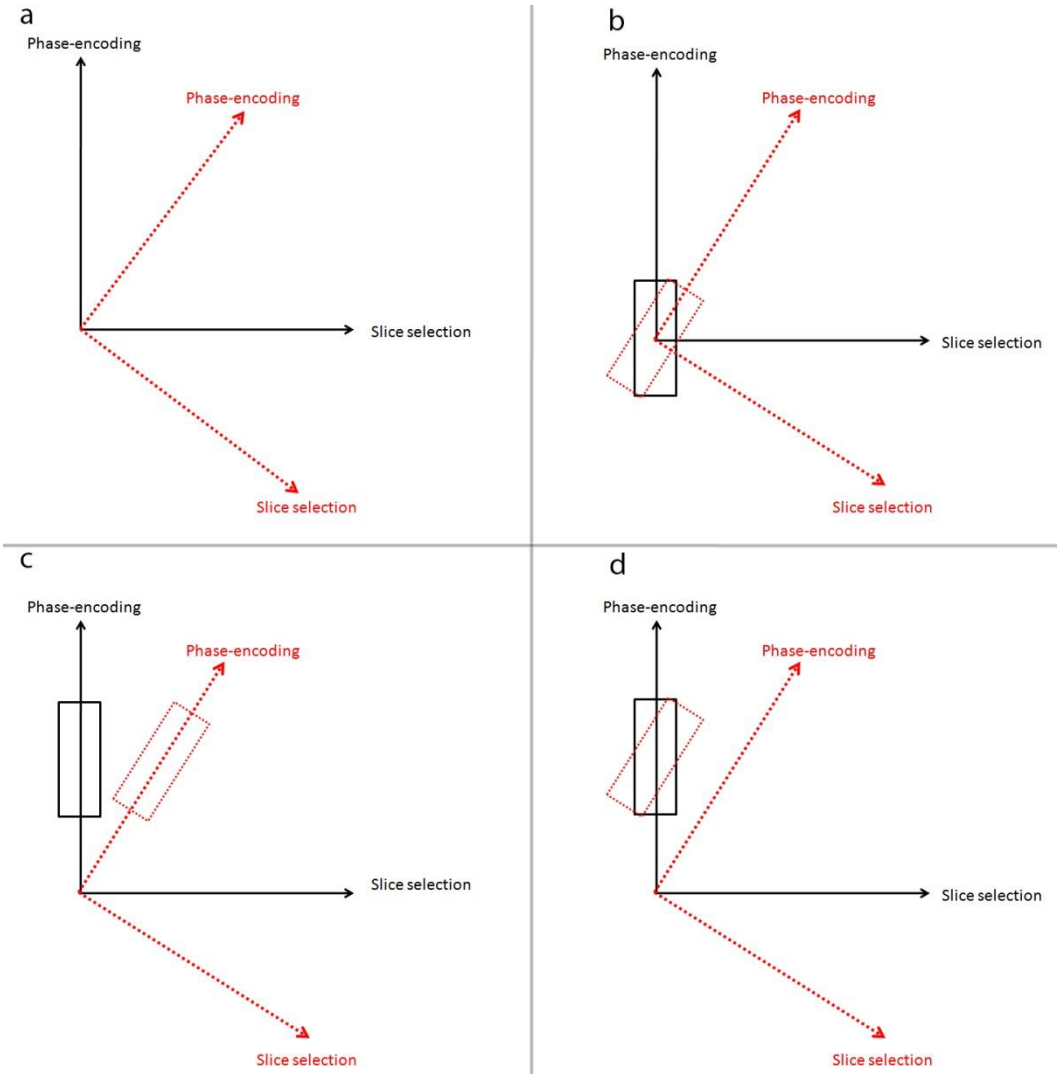

Figure 35 For clarity here are schematically reported the changes made to the code. The black reference system and rectangle are the ones relative to the 180° RF pulse, while the dotted red ones are relative the 90° RF pulse. (a) Once the rotation matrix relative to the 90° pulse is modified its reference system is titled with respect to the 180° one. (b) Also the slice relative to the 90° pulse is tilted. In the case of isocenter the center of each slice object is in the same position. (c) If the slices are not in the isocenter the center of each object is not in the same position. (d) By properly modifying the shift (both in slice and phase encoding directions) of the 90° slice object the 90° and 180° slices are centered in the same position.

5.3 Acquisition

3T scanner implementation

As reported above, the aim of this project was both to develop the sequence and to compare its performance with that of ZOOMit already implemented by Siemens. Both sequences acquire a reduced FOV but the theory behind the acquisition is different. The one developed for this project uses non-coplanar RF pulses, while ZOOMit uses parallel transmission (Blasche *et al.*, 2012). Each subject was acquired with both sequences, using the same parameter with the only exception of

TE. For each sequence, TE was chosen to be as short as possible in order to have, with a fixed resolution, the SNR as high as possible. To acquire a 60 mm long volume in the slice selection direction, Siemens ZOOMit was applied one time, acquiring 15 slices (4 mm thickness) with no gap. The one developed in this project was applied 3 times, acquiring each time 5 slices (4 mm thickness) with a 8 mm GAP. The resolution in both cases was 1.3x1.3x4mm. In the following table the main acquisition parameters are reported. Data from 8 subjects were acquired; each one was acquired in the isocenter, while 6 of them have also an acquisition in an area different from the isocenter.

At this point it is necessary to explain how the dimension of acquisition FOV impacts on the IV. The final goal was to have an IV of 26 mm in the phase encoding direction, as can be seen in table 4, the acquired FOV in that dimension is 40 mm. A schematic explanation for this choice is reported in figure 36. An IV of 26 mm with a GAP of 8 mm implicates two Tb_{phe} of 13 mm each. Choosing an acquisition FOV of 40 mm means that 13 mm below and above the center of the FOV there will be the IV (26 mm total). Each side of the IV there are the Tb split in two 7 mm long (in the phase encoding direction) areas. In these areas there will be the wraparound artifact caused by the remaining two 6 mm Tb that are outside the acquired FOV. Anyway, since these areas can be ignored in the clinical evaluation and deleted with post processing this is not a problem for the quality of the image.

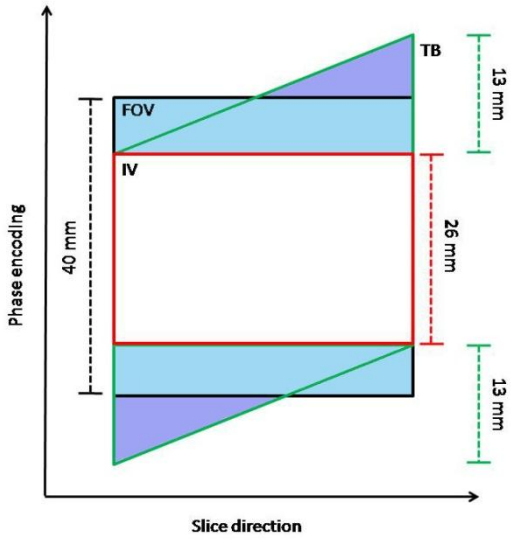

Figure 36 Schematic representation of the FOV (black rectangle, 40 mm) dimension and Tb (green rectangles, 13 mm each) influence on the final image. The desired IV (red rectangle, 26 mm) is at the center of the acquired FOV. Outside the acquired FOV, symmetrically with respect to the phase encoding direction, there are 6 mm of the Tb (violet areas). These areas cause an wraparound artifact in the remaining 7 mm of the Tb that are inside the acquired FOV (light blue

areas). This wraparound artifact will be contained in the part of Tb that remains inside the FOV without influencing the quality of the signal “contained” in the IV.

	Gradient zoom	Siemens ZOOMit
Slice number	5	15
Distance factor	200%	0%
Orientation	Transversal	Transversal
Phase encoding direction	A>>P	A>>P
Fov read	80mm	80mm
Fov phase	50%	50%
Slice thickness	4mm	4mm
TR	3200ms	3200ms
TE	57ms	66ms
Concatenations	1	1
Fat suppression	SPAIR (strong)	SPAIR (strong)
Base resolution	64	64
Phase resolution	100%	100%
Phase partial fourier	6/8	6/8
Bandwidth	752Hz/Px	752Hz/Px
Echo spacing	1.46ms	1.46ms
EPI factor	32	32
Diffusion mode	MDDW	MDDW
Diffusion weightiness	2	2
B value	1000s/mm^2	1000s/mm^2
Diffusion directions	64	64
No diffusion weighted volumes	7	7
Multi slice mode	Interleaved	Interleaved
Angle between pulses	17°	
Refocused slice thickness	11mm	

Table 4 Acquisition parameter for 1,3x1,3x4mm resolution

Two subjects were acquired with a 2mm slice thickness. Also in this case the same parameters were used for both sequences and TE, for each sequence, was chosen to be as short as possible. Siemens ZOOMit was acquired with no gap. The one developed in this project was applied 3 times with 4 mm GAP. The resolution in both cases was 1.3x1.3x2mm. Also in this case the same considerations about the acquisition FOV, that were done for acquisition with 1.3x1.3x4mm resolution, are valid.

	Gradient zoom	RF zoom
Slice number	5/7	15/21
Distance factor	200%	0%
Orientation	Transversal	Transversal
Phase encoding direction	A>>P	A>>P
Fov read	80mm	80mm
Fov phase	50%	50%
Slice thickness	2mm	2mm
TR	3200ms	3200ms
TE	57ms	76ms
Concatenations	1	1
Fat suppression	SPAIR (strong)	SPAIR (strong)
Base resolution	64	64
Phase resolution	100%	100%
Phase partial fourier	6/8	6/8
Bandwidth	752Hz/Px	752Hz/Px
Echo spacing	1.46ms	1.46ms
EPI factor	32	32
Diffusion mode	MDDW	MDDW
Diffusion weightiness	2	2
B value	1000s/mm^2	1000s/mm^2
Diffusion directions	64	64

No diffusion weighted volumes	7	7
Multi slice mode	Interleaved	Interleaved
Angle between pulses	9°	
Refocused slice thickness	6mm	

Table 5 Acquisition parameter for 1,3x1,3x2mm resolution.

9.4T scanner implementation

The sequence was developed also for the 9.4T scanner (Siemens). Here just preliminary data in human in vivo were acquired from one subject. Since for the 9.4T scanner there is no a standard sequence able to acquire a reduced FOV, here only the developed sequence was acquired. Data were acquired with 1.3x1.3x4mm and 1.3x1.3x2mm. For both resolutions 3 groups of 5 slices were acquired with a GAP of 200% of the slice thickness. Acquisition FOV was 80 mm in readout direction and 40 mm in phase encoding direction. TR was 3500 ms and TE 81 ms. 64 diffusion directions have been acquired with a b value of 1000 mm/s^2.

5.4 Results and comparison at 3T

Color coded FA maps, with a 1.3x1.3x4mm resolution, of two representative subjects are reported in figures 37 and 38, while figures 39 and 40 show color coded FA maps, with a 1.3x1.3x2mm resolution. In each column, slices of each sequence are consecutively reported. Looking at figures it is possible to note that, with the developed sequence, the FA reconstruction is correct (fibers direction is anatomically correct and the same of the one reconstructed with ZOOMit).

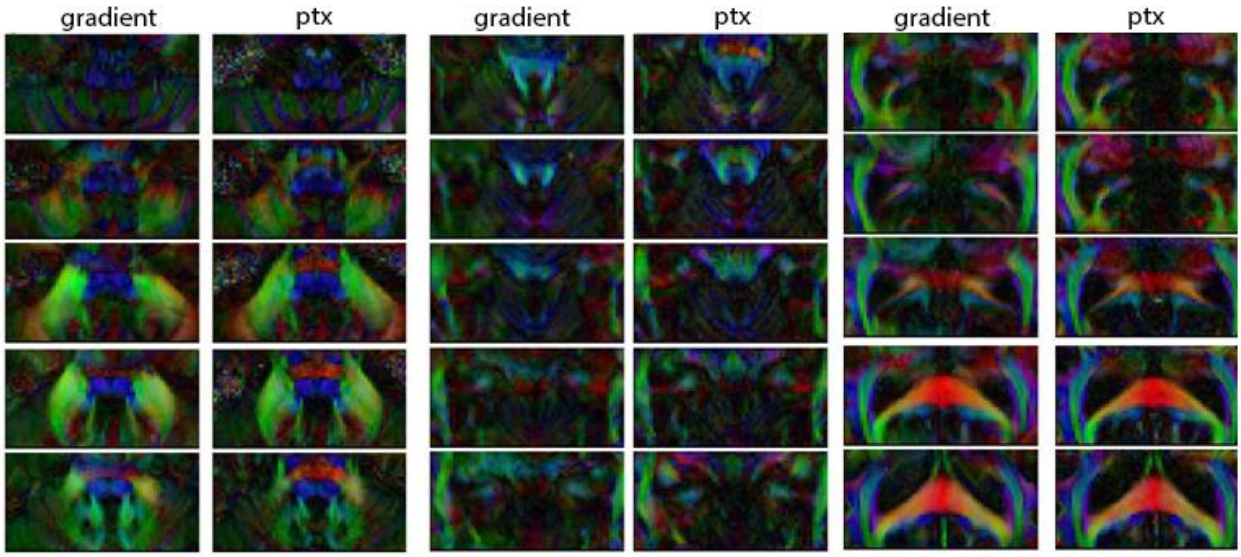

Figure 37 Color coded FA maps divided in three separated sections. Each of these is composed of two columns: left represents zoom obtained with the tilted RF pulse method (gradient label), right represents zoom obtained with the parallel transmission method (ptx label). Resolution: 1,3x1,3x4mm.

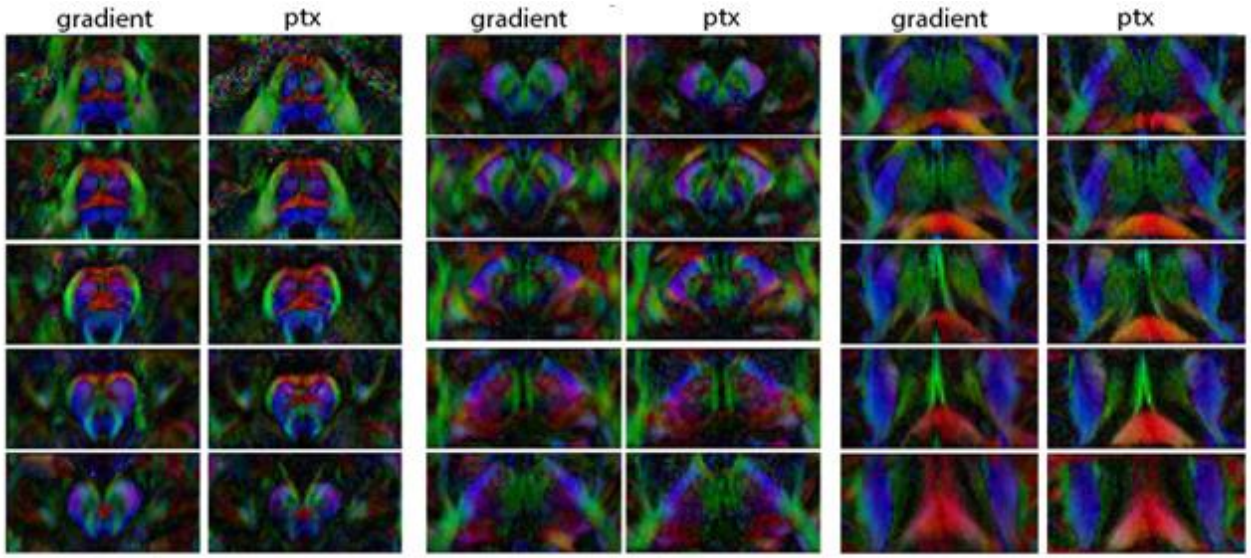

Figure 38 Color coded FA maps divided in three separated sections. Each of these is composed of two columns: left represents zoom obtained with the tilted RF pulse method (gradient label), right represents zoom obtained with the parallel transmission method (ptx label). Resolution: 1,3x1,3x4mm.

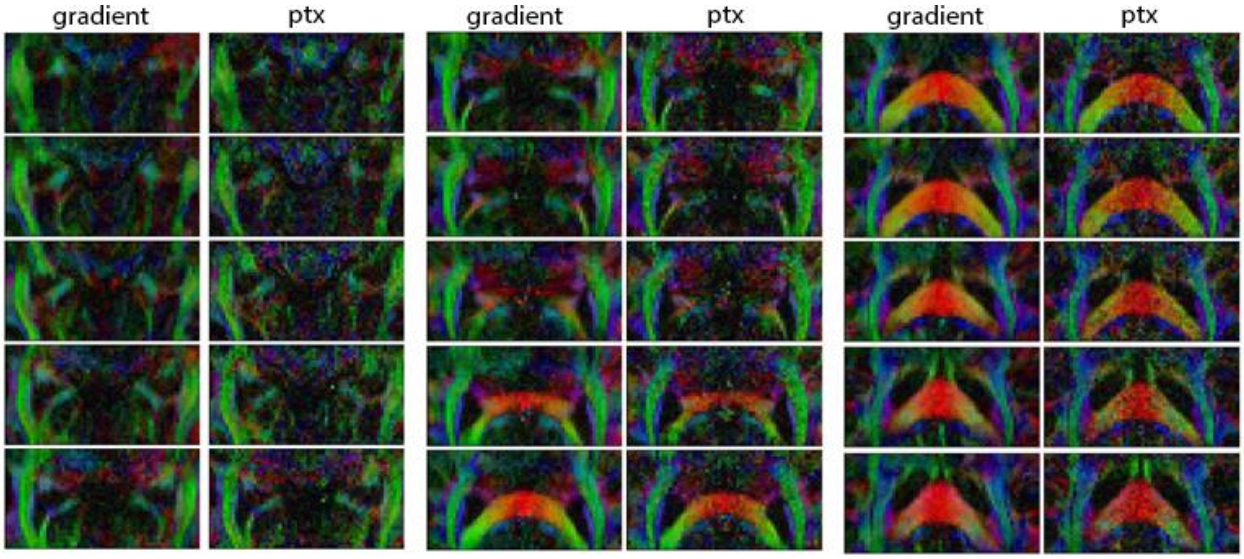

Figure 39 Color coded FA maps divided in three separated sections. Each of these is composed of two columns: left represents zoom obtained with the tilted RF pulse method (gradient label), right represents zoom obtained with the parallel transmission method (ptx label). Resolution: 1,3x1,3x2mm.

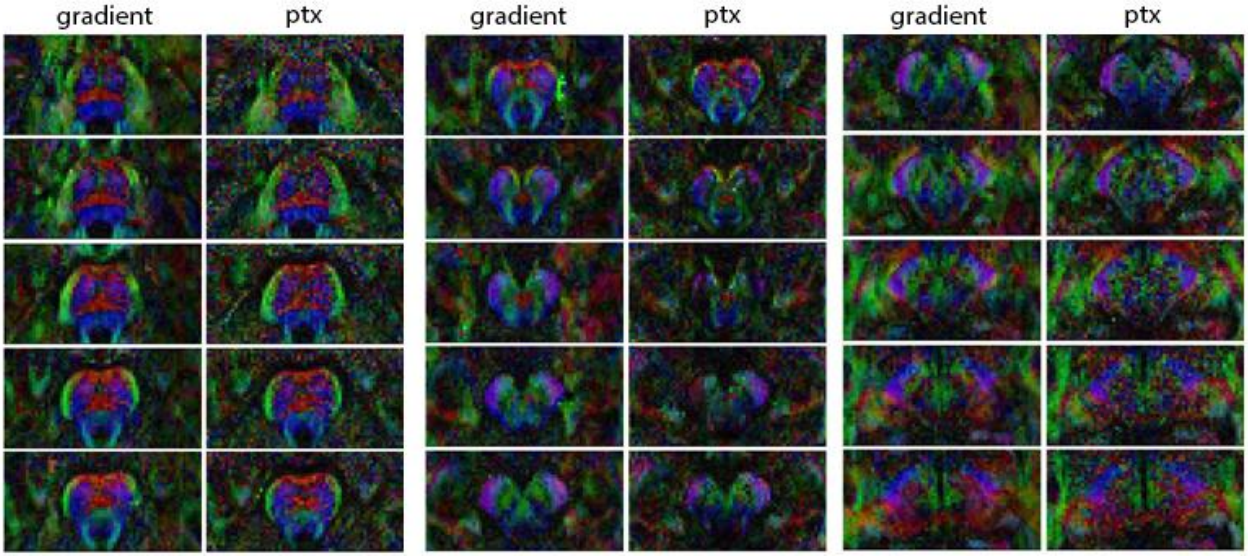

Figure 340 Color coded FA maps divided in three separated sections. Each of these is composed of two columns: left represents zoom obtained with the tilted RF pulse method (gradient label), right represents zoom obtained with the parallel transmission method (ptx label). Resolution: 1,3x1,3x2mm.

As it is possible to see from the tables above, one of the main difference between the two sequences is TE. The one developed, with a resolution of 1.3x1.3x4mm, has a TE of 9 ms shorter than the ZOOMit (table 4), while with a resolution of 1.3x1.3x2mm (table 5) the difference between TE becomes bigger (19 ms). It is well known that a longer TE has a consequence on the SNR. With the aim of verifying the impact of such difference in the acquired data, SNR was

evaluated using the signal's (S_n) mean and standard deviation of two consecutive volumes (k_1 and k_2) acquired with no diffusion gradient (Dietrich *et al.*, 2007):

$$SNR(k_1, k_2) = \frac{1}{\sqrt{2}} \frac{mean(S_n(k_1) + S_n(k_2))}{stdev(S_n(k_1) - S_n(k_2))}$$

Table 6 reports the SNR values for each acquisition with 1.3x1.3x4mm resolution, while the trend of the SNR is reported in figure 41.

Subjects	Gradient	Siemens ZOOMit
Sbj1 iso	17.0	12.5
Sbj1 ant	21.4	18.0
Sbj2 iso	16.0	11.0
Sbj2 ant	20.2	15.3
Sbj3 iso	13.3	9.5
Sbj3 ant	14.9	14.7
Sbj4 iso	16.2	10.4
Sbj4 ant	16.8	12.1
Sbj5 iso	19.9	16.7
Sbj5 ant	16.0	12.4
Sbj6 iso	15.5	9.4
Sbj6 ant	22.8	15.6
Sbj7 iso	20.2	13.8
Sbj8 iso	21.8	15.7
MEAN	**18.0**	**13.4**
STDV	**3.0**	**2.7**
MEAN/STDV	**6.1**	**4.9**

Table 6 Gradient based and Siemens ZOOMit SNR (1.3x1.3x4mm resolution).

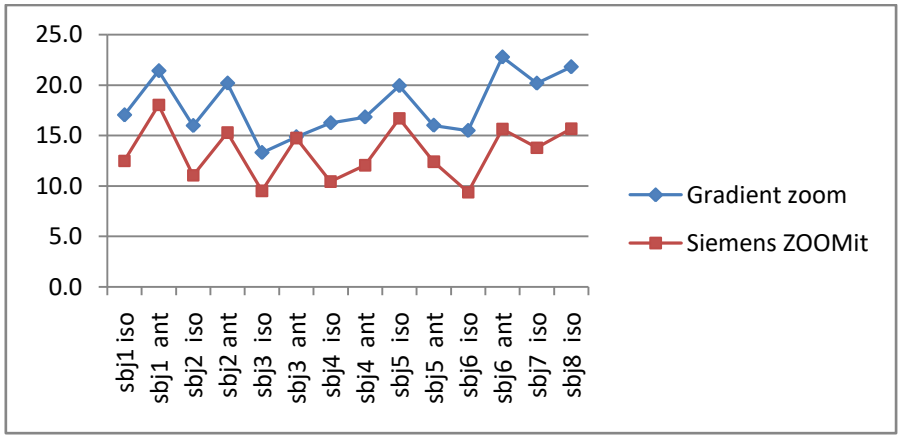

Figure 41 Gradient based and Siemens ZOOMit SNR (1.3x1.3x4mm resolution).

The SNR was also compared with a 1.3x1.3x2mm resolution data.

Subjects	Gradient	Siemens ZOOMit
Sbj5 iso	12.8	7.6
Sbj6 iso	9.6	5.5

Table 6 Gradient based and Siemens ZOOMit SNR (1.3x1.3x2mm resolution).

Previous tables and images show that the developed sequence in every acquisition has higher SNR than the ZOOMit sequence. Total acquisition time of our sequence is longer with respect to the Siemens one, due to the fact that it is necessary to acquire three groups of slices separately. Further improvement to the code and the development of a proper interleaved acquisition mode will help to reduce the total acquisition time. Despite the time limitation, the higher SNR obtained with the sequence developed is a good advantage. It is possible indeed to reach higher resolutions, consequently acquiring more accurate data. It is to note that gaining in plain resolution involved losing z-resolution (slice thickness), consequently moving away from an isotropic voxel. If in certain application this could be a disadvantage, in other studies, where high in plane resolution is required (lesion, spinal cord, optic nerve, thalamic nuclei investigation) could be an advantage (Wheeler-Kingshott *et al.*, 2002; Wilm *et al.*, 2007). Furthermore here the sequence was stressed in order ot reach the higher in plane resolution, further developments can be done in order to reach an isotropic condition. This project's sequence implicates advantages also from the hardware point of view. Indeed, parallel transmission method, the one used by ZOOMit, needs a scanner upgrade with a change of transmission coils. Whereas, by using non-coplanar gradients to acquire a reduce FOV, it is possible to run the sequence with every clinical

scanner, without any hardware change. Therefore, even if something else needs to be changed in order to reach better performances in terms of total acquisition time, the results obtained here are promising in terms of SNR and adaptability of the sequence.

5.5 Preliminary results at 9.4T

Color coded FA maps of the data acquired with 9.4T scanner are reported in figure 42 and 43 for resolution of 1.3x1.3x4mm and 1.3x1.3x2mm respectively. The color coded reconstruction was successfully performed and fiber direction is coherent with anatomical knowledge. As expected, data quality, in particular the one with 1.3x1.3x2mm resolution, is not as good as the one obtained with 3T. It is to note that the 9.4T scanner is only used for research and everything from coil to sequence is non-conventional. This, at the same time, implicates a lot of improvements chances and acquisition issues. The main problem encountered while acquiring diffusion data was related to field homogeneity. It was indeed necessary, before every acquisition, to manually adjust the shimming and even after this adjustment it was possible to acquire only occipital brain areas where the field was more strong and stable. Higher order shimming adjustments can be used in order to improve data quality and acquire in brain areas different from the posterior ones. Anyway the aim of 9.4T acquisitions was to verify if the same principle used with the 3T scanner could be applied also to ultra high field without huge problems. The results obtained are promising, indeed, data are anatomically coherent even if improvements are necessary. To the best of our knowledge this is the first time that a reduced FOV technique has been applied with a 9.4T scanner. This is an interesting starting point for application of this technique in body regions where high resolution is desired.

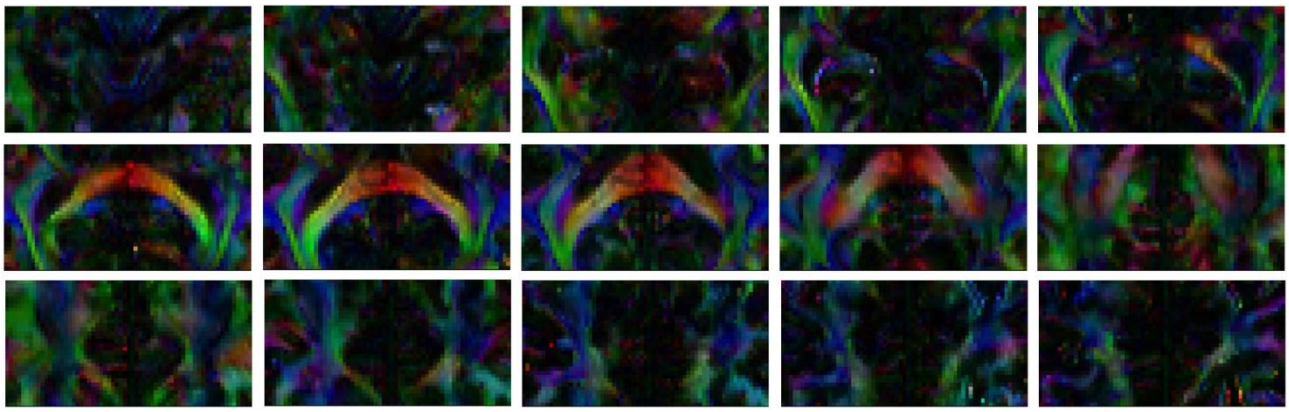

Figure 42 Color coded FA maps from 9.4T data. Resolution: 1,3x1,3x4mm.

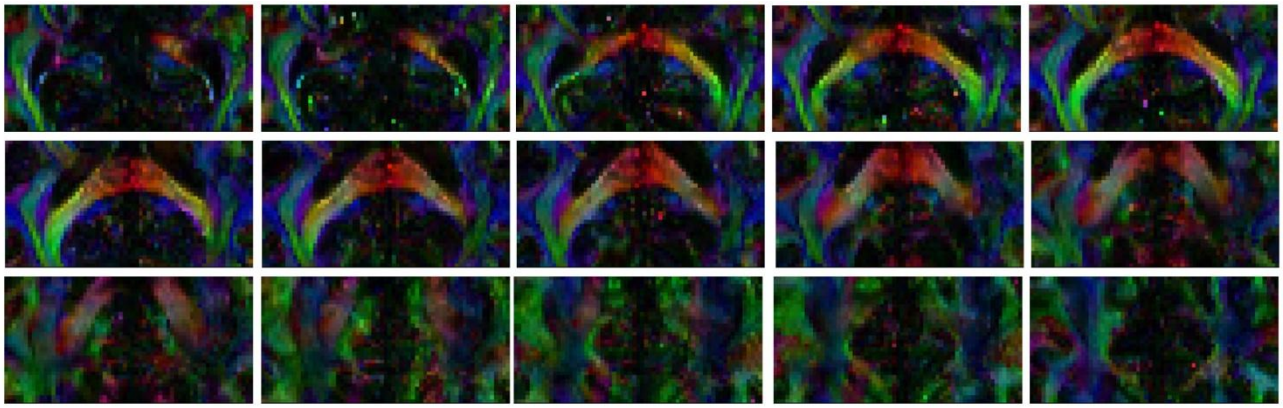

Figure 43 Color coded FA maps from 9.4T data. Resolution: 1,3x1,3x4mm.

Chapter 6: General conclusions

The core point of this thesis was the application of DTI (tractography and diffusion parameters) in order to investigate WM structure in terms of connectivity and diffusion properties. Advanced probabilistic tractography method was applied to investigate, in healthy human subjects in vivo, a pathway (CPC) connecting the cerebral cortex with the cerebellum. A voxel-wise analysis of the whole brain was performed to find core WM changes between HC and patients affected by AD and VaD.

The tractographic reconstruction of the CPC pathway suggested direct connection between cerebral and cerebellar areas related to cognition, giving a further proof about cerebellar involvement, not only in motor but also in cognitive tasks. In order to investigate the whole cerebro-cerebellar loop structure, the results obtained through this work were also compared with those related to the CTC pathway. An interesting similarity, with already existent theoretical models about cerebro-cerebellar connectivity, emerged from this comparison. Cerebro-cerebellar connections, related to motor task seems to be direct, while connections relative to cognitive tasks interest multiple brain areas. The different involvement of cerebral areas depending on motor or cognitive functions could provide further information for the development of models of cerebro-cerebellar network loop. Furthermore, since the analysis was performed on data acquired on a standard clinical scanner, this method could be applied in the assessment of the integrity of the cerebro-cerebellar connectivity in pathologies.

From the TBSS analysis, the more useful WM bundles in order to distinguish between controls, AD and VaD patients seem to be parahippocampal gyri, corpus callosum and thalamic radiations. These WM tracts are known to have a role in cognition. Furthermore, differences among the three groups of subjects emerged also in cerebellar cognitive areas. Even if further analyses need to be performed in order to confirm the results obtained from TBSS, the found areas could be useful in order to develop a multimodal machine learning approach, able to help diagnosis automatically differentiating between these dementia cases.

WM bundles emerged from TBSS analysis are known to be involved in cognition and the CPC and CTC pathways were found to be involved in the connection of cognitive cerebro and cerebellar areas. This common cognitive involvement suggests, as future work, to investigate the cerebro-cerebellar loop in AD and VaD patients. This means to reconstruct the CTC and CPC pathways and to perform TBSS analysis on the reconstructed tracts with the aim of verifying if different values of

diffusion parameters reveal different characteristics in the cerebro-cerebellar loop between these different types of dementias and healthy subjects. Results from such analysis, along with the ones already found, could be an important starting point for further investigations and give a solid basis to develop automatic classification algorithms.

Even though, both tractography and TBSS analysis revealed good quality and interesting results, DTI suffers from resolution issues due to the trade off between voxel size and SNR. Despite all post processing techniques that give the chance to improve resolution and perform detailed analysis, investigations in specific brain (e.g. pons, cerebellum) and body areas (e.g. spinal cord) would benefit from higher resolution acquisition. Even if, with the actual technology, it is impossible to reach resolution comparable with fiber dimensions, in order to partially solve this resolution problem, a sequence able to acquire diffusion data in a small FOV with high resolution was developed. Data acquired with this sequence showed good SNR values and an anatomically reliable reconstruction of color coded FA maps. This sequence can therefore be applied to investigate specific parts of the cerebro-cerebellar loop (e.g. areas where pathways decussate) or to acquire only specific part of WM bundles emerged from TBSS analysis. Higher resolution can indeed lead to a more reliable tractography and estimation of diffusion parameter.

All projects described in this thesis give interesting information about WM connectivity and structural properties, along with new advanced investigation tools. The obtained results suggest further experiments where all the techniques, here applied separately, can be applied together, in order to improve the quality of results and to formulate new hypotheses about brain connections, providing helpful information both for neurophysiologic and clinical investigations.

Bibliography

Acosta-Cabronero J, Alley S, Williams GB, Pengas G, Nestor PJ. Diffusion tensor metrics as biomarkers in Alzheimer's disease. PLoS One 2012; 7(11): e49072.

Acosta-Cabronero J, Williams GB, Pengas G, Nestor PJ. Absolute diffusivities define the landscape of white matter degeneration in Alzheimer's disease. Brain 2010; 133(Pt 2): 529-39.

Alexander AL, Lee JE, Lazar M, Field AS. Diffusion tensor imaging of the brain. Neurotherapeutics 2007; 4(3): 316-29.

Alves GS, Sudo FK, Alves CEdO, Ericeira-Valente L, Moreira DM, Engelhardt E*, et al.* Diffusion tensor imaging studies in vascular disease: a review of the literature. Dement neuropsychol 2012; 6(3).

Assaf Y, Pasternak O. Diffusion tensor imaging (DTI)-based white matter mapping in brain research: a review. J Mol Neurosci 2008; 34(1): 51-61.

Axmacher N, Schmitz DP, Wagner T, Elger CE, Fell J. Interactions between medial temporal lobe, prefrontal cortex, and inferior temporal regions during visual working memory: a combined intracranial EEG and functional magnetic resonance imaging study. J Neurosci 2008; 28(29): 7304-12.

Basser PJ, Jones DK. Diffusion-tensor MRI: theory, experimental design and data analysis - a technical review. NMR Biomed 2002; 15(7-8): 456-67.

Basser PJ, Mattiello J, LeBihan D. Estimation of the effective self-diffusion tensor from the NMR spin echo. Journal of Magnetic Resonance, Series B 1994; 103(3): 247-54.

Basser PJ, Pajevic S, Pierpaoli C, Duda J, Aldroubi A. In vivo fiber tractography using DT-MRI data. Magn Reson Med 2000; 44(4): 625-32.

Basser PJ, Pierpaoli C. Microstructural and physiological features of tissues elucidated by quantitative-diffusion-tensor MRI. Journal of magnetic resonance 2011; 213(2): 560-70.

Baumann O, Borra RJ, Bower JM, Cullen KE, Habas C, Ivry RB*, et al.* Consensus paper: the role of the cerebellum in perceptual processes. Cerebellum 2015; 14(2): 197-220.

Beaulieu C, Does MD, Snyder RE, Allen PS. Changes in water diffusion due to Wallerian degeneration in peripheral nerve. Magn Reson Med 1996; 36(4): 627-31.

Behrens T, Berg HJ, Jbabdi S, Rushworth M, Woolrich M. Probabilistic diffusion tractography with multiple fibre orientations: What can we gain? Neuroimage 2007; 34(1): 144-55.

Blasche M, Riffel P, Lichy M. TimTX TrueShape and syngo ZOOMit technical and practical aspects. Magnetom Flash 2012; 1: 74-84.

Booth JR, Wood L, Lu D, Houk JC, Bitan T. The role of the basal ganglia and cerebellum in language processing. Brain Res 2007; 1133(1): 136-44.

Bosch B, Arenaza-Urquijo EM, Rami L, Sala-Llonch R, Junqué C, Solé-Padullés C*, et al.* Multiple DTI index analysis in normal aging, amnestic MCI and AD. Relationship with neuropsychological performance. Neurobiol Aging 2012; 33(1): 61-74.

Bozzali M, Giulietti G, Basile B, Serra L, Spanò B, Perri R*, et al.* Damage to the cingulum contributes to Alzheimer's disease pathophysiology by deafferentation mechanism. Hum Brain Mapp 2012; 33(6): 1295-308.

Branca FP. Fondamenti di Ingegneria Clinica: Volume 2: Ecotomografia: Springer Science & Business Media; 2008.

Brodal P. The corticopontine projection in the rhesus monkey. Origin and principles of organization. Brain 1978; 101(2): 251-83.

Brodal P. The pontocerebellar projection in the rhesus monkey: an experimental study with retrograde axonal transport of horseradish peroxidase. Neuroscience 1979; 4(2): 193-208.

Brodmann K. Brodmann's: Localisation in the Cerebral Cortex. 3rd ed; 2006.
Brown MA, Semelka RC. MRI: basic principles and applications: John Wiley & Sons; 2011.
Buckner RL, Krienen FM, Castellanos A, Diaz JC, Yeo BT. The organization of the human cerebellum estimated by intrinsic functional connectivity. J Neurophysiol 2011; 106(5): 2322-45.
Burgess N, Maguire EA, Spiers HJ, O'Keefe J. A temporoparietal and prefrontal network for retrieving the spatial context of lifelike events. Neuroimage 2001; 14(2): 439-53.
Calamante F, Tournier JD, Jackson GD, Connelly A. Track-density imaging (TDI): super-resolution white matter imaging using whole-brain track-density mapping. Neuroimage 2010; 53(4): 1233-43.
Castellazzi G, Palesi F, Casali S, Vitali P, Sinforiani E, Wheeler-Kingshott CA*, et al.* A comprehensive assessment of resting state networks: bidirectional modification of functional integrity in cerebro-cerebellar networks in dementia. Front Neurosci 2014; 8: 223.
Catani M, Thiebaut de Schotten M. A diffusion tensor imaging tractography atlas for virtual in vivo dissections. Cortex 2008; 44(8): 1105-32.
Cercignani M, Horsfield MA, Agosta F, Filippi M. Sensitivity-encoded diffusion tensor MR imaging of the cervical cord. American journal of neuroradiology 2003; 24(6): 1254-6.
Ciccarelli O, Toosy AT, Parker GJ, Wheeler-Kingshott CA, Barker GJ, Miller DH*, et al.* Diffusion tractography based group mapping of major white-matter pathways in the human brain. Neuroimage 2003; 19(4): 1545-55.
Cook PA, Symms M, Boulby PA, Alexander DC. Optimal acquisition orders of diffusion-weighted MRI measurements. J Magn Reson Imaging 2007; 25(5): 1051-8.
Corben LA, Georgiou-Karistianis N, Bradshaw JL, Hocking DR, Churchyard AJ, Delatycki MB. The Fitts task reveals impairments in planning and online control of movement in Friedreich ataxia: reduced cerebellar-cortico connectivity? Neuroscience 2011; 192: 382-90.
Cummings JL. Vascular subcortical dementias: clinical aspects. Dementia 1994; 5(3-4): 177-80.
D'Angelo E, Casali S. Seeking a unified framework for cerebellar function and dysfunction: from circuit operations to cognition. Front Neural Circuits 2012; 6: 116.
Descoteaux M, Sidhu J, Garyfallidis E, Houde J-C, Neher P, Stieltjes B*, et al.* False positive bundles in tractography. ISMRM; 2016; Singapore; 2016.
Detoledo-Morrell L, Sullivan MP, Morrell F, Wilson RS, Bennett DA, Spencer S. Alzheimer's disease: in vivo detection of differential vulnerability of brain regions. Neurobiol Aging 1997; 18(5): 463-8.
Diedrichsen J, Balsters JH, Flavell J, Cussans E, Ramnani N. A probabilistic MR atlas of the human cerebellum. Neuroimage 2009; 46(1): 39-46.
Dietrich O, Raya JG, Reeder SB, Reiser MF, Schoenberg SO. Measurement of signal-to-noise ratios in MR images: Influence of multichannel coils, parallel imaging, and reconstruction filters. Journal of Magnetic Resonance Imaging 2007; 26(2): 375-85.
Dobromyslin VI, Salat DH, Fortier CB, Leritz EC, Beckmann CF, Milberg WP*, et al.* Distinct functional networks within the cerebellum and their relation to cortical systems assessed with independent component analysis. Neuroimage 2012; 60(4): 2073-85.
Echávarri C, Aalten P, Uylings HB, Jacobs HI, Visser PJ, Gronenschild EH*, et al.* Atrophy in the parahippocampal gyrus as an early biomarker of Alzheimer's disease. Brain Struct Funct 2011; 215(3-4): 265-71.
Einstein A. Investigations on the Theory of the Brownian Movement: Courier Corporation; 1956.
Ennis DB, Kindlmann G. Orthogonal tensor invariants and the analysis of diffusion tensor magnetic resonance images. Magnetic Resonance in Medicine 2006; 55(1): 136-46.
Feinberg DA, Hoenninger J, Crooks L, Kaufman L, Watts J, Arakawa M. Inner volume MR imaging: technical concepts and their application. Radiology 1985; 156(3): 743-7.
Filip P, Lungu OV, Bareš M. Dystonia and the cerebellum: a new field of interest in movement disorders? Clin Neurophysiol 2013; 124(7): 1269-76.

Fiori S, Pannek K, Pasquariello R, Ware RS, Cioni G, Rose SE*, et al.* Corticopontocerebellar Connectivity Disruption in Congenital Hemiplegia. Neurorehabil Neural Repair 2015.
Genc S, Steward CE, Malpas CB, Velakoulis D, O'Brien TJ, Desmond PM. Short-term white matter alterations in Alzheimer's disease characterized by diffusion tensor imaging. J Magn Reson Imaging 2015.
Gili T, Cercignani M, Serra L, Perri R, Giove F, Maraviglia B*, et al.* Regional brain atrophy and functional disconnection across Alzheimer's disease evolution. J Neurol Neurosurg Psychiatry 2011; 82(1): 58-66.
Glickstein M. The cerebellum and motor learning. Curr Opin Neurobiol 1992; 2(6): 802-6.
Glickstein M, Gerrits N, Kralj-Hans I, Mercier B, Stein J, Voogd J. Visual pontocerebellar projections in the macaque. J Comp Neurol 1994; 349(1): 51-72.
Glickstein M, May JG, Mercier BE. Corticopontine projection in the macaque: the distribution of labelled cortical cells after large injections of horseradish peroxidase in the pontine nuclei. J Comp Neurol 1985; 235(3): 343-59.
Gold BT, Powell DK, Andersen AH, Smith CD. Alterations in multiple measures of white matter integrity in normal women at high risk for Alzheimer's disease. Neuroimage 2010; 52(4): 1487-94.
Granziera C, Schmahmann JD, Hadjikhani N, Meyer H, Meuli R, Wedeen V*, et al.* Diffusion spectrum imaging shows the structural basis of functional cerebellar circuits in the human cerebellum in vivo. PLoS One 2009; 4(4): e5101.
Grodd W, Hülsmann E, Lotze M, Wildgruber D, Erb M. Sensorimotor mapping of the human cerebellum: fMRI evidence of somatotopic organization. Hum Brain Mapp 2001; 13(2): 55-73.
Gudbjartsson H, Maier SE, Mulkern RV, Mórocz IA, Patz S, Jolesz FA. Line scan diffusion imaging. Magn Reson Med 1996; 36(4): 509-19.
Habas C, Cabanis EA. Anatomical parcellation of the brainstem and cerebellar white matter: a preliminary probabilistic tractography study at 3 T. Neuroradiology 2007; 49(10): 849-63.
Habas C, Guillevin R, Abanou A. Functional connectivity of the superior human temporal sulcus in the brain resting state at 3T. Neuroradiology 2011; 53(2): 129-40.
Habas C, Kamdar N, Nguyen D, Prater K, Beckmann CF, Menon V*, et al.* Distinct cerebellar contributions to intrinsic connectivity networks. J Neurosci 2009; 29(26): 8586-94.
Hashemi RH, Bradley WG, Lisanti CJ. MRI: the basics: Lippincott Williams & Wilkins; 2012.
Heath RG, Harper JW. Ascending projections of the cerebellar fastigial nucleus to the hippocampus, amygdala, and other temporal lobe sites: evoked potential and histological studies in monkeys and cats. Exp Neurol 1974; 45(2): 268-87.
Holdsworth SJ, Skare S, Newbould RD, Guzmann R, Blevins NH, Bammer R. Readout-segmented EPI for rapid high resolution diffusion imaging at 3T. European journal of radiology 2008; 65(1): 36-46.
Ito M. Cerebellar circuitry as a neuronal machine. Prog Neurobiol 2006; 78(3-5): 272-303.
Ito M. Control of mental activities by internal models in the cerebellum. Nat Rev Neurosci 2008; 9(4): 304-13.
Jang SH, Chang PH, Kim YK, Seo JP. Anatomical location of the frontopontine fibers in the internal capsule in the human brain: a diffusion tensor tractography study. Neuroreport 2014; 25(2): 117-21.
Jbabdi S, Lehman JF, Haber SN, Behrens TE. Human and monkey ventral prefrontal fibers use the same organizational principles to reach their targets: tracing versus tractography. J Neurosci 2013; 33(7): 3190-201.
Jenkinson M, Bannister P, Brady M, Smith S. Improved optimization for the robust and accurate linear registration and motion correction of brain images. Neuroimage 2002a; 17(2): 825-41.
Jenkinson M, Bannister P, Brady M, Smith S. Improved optimization for the robust and accurate linear registration and motion correction of brain images. Neuroimage 2002b; 17(2): 825-41.

Jenkinson M, Smith S. A global optimisation method for robust affine registration of brain images. Med Image Anal 2001; 5(2): 143-56.
Jones DK, Knösche TR, Turner R. White matter integrity, fiber count, and other fallacies: the do's and don'ts of diffusion MRI. Neuroimage 2013; 73: 239-54.
Kamali A, Kramer LA, Frye RE, Butler IJ, Hasan KM. Diffusion tensor tractography of the human brain cortico-ponto-cerebellar pathways: a quantitative preliminary study. J Magn Reson Imaging 2010; 32(4): 809-17.
Kawato M, Furukawa K, Suzuki R. A hierarchical neural-network model for control and learning of voluntary movement. Biol Cybern 1987; 57(3): 169-85.
Kelly RM, Strick PL. Cerebellar loops with motor cortex and prefrontal cortex of a nonhuman primate. J Neurosci 2003; 23(23): 8432-44.
Keser Z, Hasan KM, Mwangi BI, Kamali A, Ucisik-Keser FE, Riascos RF*, et al.* Diffusion tensor imaging of the human cerebellar pathways and their interplay with cerebral macrostructure. Front Neuroanat 2015; 9: 41.
Kirchhoff BA, Wagner AD, Maril A, Stern CE. Prefrontal-temporal circuitry for episodic encoding and subsequent memory. J Neurosci 2000; 20(16): 6173-80.
Klein A, Andersson J, Ardekani BA, Ashburner J, Avants B, Chiang MC*, et al.* Evaluation of 14 nonlinear deformation algorithms applied to human brain MRI registration. Neuroimage 2009; 46(3): 786-802.
Krienen FM, Buckner RL. Segregated fronto-cerebellar circuits revealed by intrinsic functional connectivity. Cereb Cortex 2009; 19(10): 2485-97.
Kuperman V. Magnetic resonance imaging: physical principles and applications: Academic Press; 2000.
Kwon HG, Hong JH, Hong CP, Lee DH, Ahn SH, Jang SH. Dentatorubrothalamic tract in human brain: diffusion tensor tractography study. Neuroradiology 2011; 53(10): 787-91.
Lascano AM, Lemkaddem A, Granziera C, Korff CM, Boex C, Jenny B*, et al.* Tracking the source of cerebellar epilepsy: hemifacial seizures associated with cerebellar cortical dysplasia. Epilepsy Res 2013; 105(1-2): 245-9.
Lehman JF, Greenberg BD, McIntyre CC, Rasmussen SA, Haber SN. Rules ventral prefrontal cortical axons use to reach their targets: implications for diffusion tensor imaging tractography and deep brain stimulation for psychiatric illness. J Neurosci 2011; 31(28): 10392-402.
Leiner HC, Leiner AL, Dow RS. The human cerebro-cerebellar system: its computing, cognitive, and language skills. Behav Brain Res 1991; 44(2): 113-28.
Liu Y, Spulber G, Lehtimäki KK, Könönen M, Hallikainen I, Gröhn H*, et al.* Diffusion tensor imaging and tract-based spatial statistics in Alzheimer's disease and mild cognitive impairment. Neurobiol Aging 2011; 32(9): 1558-71.
Marr D. A theory of cerebellar cortex. J Physiol 1969; 202(2): 437-70.
Mayzel-Oreg O, Assaf Y, Gigi A, Ben-Bashat D, Verchovsky R, Mordohovitch M*, et al.* High b-value diffusion imaging of dementia: application to vascular dementia and alzheimer disease. J Neurol Sci 2007; 257(1-2): 105-13.
McKhann GM, Knopman DS, Chertkow H, Hyman BT, Jack CR, Kawas CH*, et al.* The diagnosis of dementia due to Alzheimer's disease: recommendations from the National Institute on Aging-Alzheimer's Association workgroups on diagnostic guidelines for Alzheimer's disease. Alzheimers Dement 2011; 7(3): 263-9.
McRobbie DW, Moore EA, Graves MJ, Prince MR. MRI from Picture to Proton: Cambridge university press; 2007.

Medina D, DeToledo-Morrell L, Urresta F, Gabrieli JD, Moseley M, Fleischman D*, et al.* White matter changes in mild cognitive impairment and AD: A diffusion tensor imaging study. Neurobiol Aging 2006; 27(5): 663-72.
Metzler-Baddeley C, Jones DK, Belaroussi B, Aggleton JP, O'Sullivan MJ. Frontotemporal connections in episodic memory and aging: a diffusion MRI tractography study. J Neurosci 2011; 31(37): 13236-45.
Mori S, van Zijl PC. Fiber tracking: principles and strategies - a technical review. NMR Biomed 2002; 15(7-8): 468-80.
Mori S, Zhang J. Diffusion Tensor Imaging (DTI). 2009.
Morita T, Morimoto M, Yamada K, Hasegawa T, Morioka S, Kidowaki S*, et al.* Low-grade intraventricular hemorrhage disrupts cerebellar white matter in preterm infants: evidence from diffusion tensor imaging. Neuroradiology 2015; 57(5): 507-14.
Nolte UG, Finsterbusch J, Frahm J. Rapid isotropic diffusion mapping without susceptibility artifacts: Whole brain studies using diffusion-weighted single-shot STEAM MR imaging. Magnetic resonance in medicine 2000; 44(5): 731-6.
O'Dwyer L, Lamberton F, Bokde AL, Ewers M, Faluyi YO, Tanner C*, et al.* Multiple indices of diffusion identifies white matter damage in mild cognitive impairment and Alzheimer's disease. PLoS One 2011; 6(6): e21745.
Olsson Y, Brun A, Englund E. Fundamental pathological lesions in vascular dementia. Acta Neurol Scand Suppl 1996; 168: 31-8.
Ostojic J, Kozic D, Pavlovic A, Semnic M, Todorovic A, Petrovic K*, et al.* Hippocampal diffusion tensor imaging microstructural changes in vascular dementia. Acta Neurol Belg 2015.
Palesi F, Tournier JD, Calamante F, Muhlert N, Castellazzi G, Chard D*, et al.* Contralateral cerebello-thalamo-cortical pathways with prominent involvement of associative areas in humans in vivo. Brain Struct Funct 2014.
Poletti CE, Creswell G. Fornix system efferent projections in the squirrel monkey: an experimental degeneration study. J Comp Neurol 1977; 175(1): 101-28.
Ramnani N. The primate cortico-cerebellar system: anatomy and function. Nat Rev Neurosci 2006; 7(7): 511-22.
Ramnani N. Frontal lobe and posterior parietal contributions to the cortico-cerebellar system. Cerebellum 2012; 11(2): 366-83.
Reed BR, Mungas DM, Kramer JH, Ellis W, Vinters HV, Zarow C*, et al.* Profiles of neuropsychological impairment in autopsy-defined Alzheimer's disease and cerebrovascular disease. Brain 2007; 130(Pt 3): 731-9.
Rieseberg S, Frahm J, Finsterbusch J. Two-dimensional spatially-selective RF excitation pulses in echo-planar imaging. Magnetic resonance in medicine 2002; 47(6): 1186-93.
Rizzi L, Rosset I, Roriz-Cruz M. Global epidemiology of dementia: Alzheimer's and vascular types. Biomed Res Int 2014; 2014: 908915.
Rose SE, Janke AL, Chalk JB. Gray and white matter changes in Alzheimer's disease: a diffusion tensor imaging study. J Magn Reson Imaging 2008; 27(1): 20-6.
Sahama I, Sinclair K, Fiori S, Doecke J, Pannek K, Reid L*, et al.* Motor pathway degeneration in young ataxia telangiectasia patients: A diffusion tractography study. Neuroimage Clin 2015; 9: 206-15.
Salat DH, Tuch DS, van der Kouwe AJ, Greve DN, Pappu V, Lee SY*, et al.* White matter pathology isolates the hippocampal formation in Alzheimer's disease. Neurobiol Aging 2010; 31(2): 244-56.
Salmi J, Pallesen KJ, Neuvonen T, Brattico E, Korvenoja A, Salonen O*, et al.* Cognitive and motor loops of the human cerebro-cerebellar system. J Cogn Neurosci 2010; 22(11): 2663-76.
Savoiardo M, Grisoli M. Imaging dementias. Eur Radiol 2001; 11(3): 484-92.

Schmahmann JD, Caplan D. Cognition, emotion and the cerebellum. Brain 2006; 129(Pt 2): 290-2.
Schmahmann JD, Doyon J, McDonald D, Holmes C, Lavoie K, Hurwitz AS*, et al.* Three-dimensional MRI atlas of the human cerebellum in proportional stereotaxic space. Neuroimage 1999; 10(3 Pt 1): 233-60.
Schmahmann JD, Pandya DN. Projections to the basis pontis from the superior temporal sulcus and superior temporal region in the rhesus monkey. J Comp Neurol 1991; 308(2): 224-48.
Schmahmann JD, Pandya DN. The cerebrocerebellar system. Int Rev Neurobiol 1997; 41: 31-60.
Schmahmann JD, Pandya DN, Wang R, Dai G, D'Arceuil HE, de Crespigny AJ*, et al.* Association fibre pathways of the brain: parallel observations from diffusion spectrum imaging and autoradiography. Brain 2007; 130(Pt 3): 630-53.
Shu N, Wang Z, Qi Z, Li K, He Y. Multiple diffusion indices reveals white matter degeneration in Alzheimer's disease and mild cognitive impairment: a tract-based spatial statistics study. J Alzheimers Dis 2011; 26 Suppl 3: 275-85.
Simons JS, Spiers HJ. Prefrontal and medial temporal lobe interactions in long-term memory. Nat Rev Neurosci 2003; 4(8): 637-48.
Smith RE, Tournier JD, Calamante F, Connelly A. Anatomically-constrained tractography: improved diffusion MRI streamlines tractography through effective use of anatomical information. Neuroimage 2012; 62(3): 1924-38.
Smith RE, Tournier JD, Calamante F, Connelly A. SIFT: Spherical-deconvolution informed filtering of tractograms. Neuroimage 2013; 67: 298-312.
Smith RE, Tournier JD, Calamante F, Connelly A. SIFT2: Enabling dense quantitative assessment of brain white matter connectivity using streamlines tractography. Neuroimage 2015a; 119: 338-51.
Smith RE, Tournier JD, Calamante F, Connelly A. The effects of SIFT on the reproducibility and biological accuracy of the structural connectome. Neuroimage 2015b; 104: 253-65.
Smith SM. Fast robust automated brain extraction. Hum Brain Mapp 2002; 17(3): 143-55.
Smith SM, Jenkinson M, Johansen-Berg H, Rueckert D, Nichols TE, Mackay CE*, et al.* Tract-based spatial statistics: voxelwise analysis of multi-subject diffusion data. Neuroimage 2006; 31(4): 1487-505.
Smith SM, Johansen-Berg H, Jenkinson M, Rueckert D, Nichols TE, Miller KL*, et al.* Acquisition and voxelwise analysis of multi-subject diffusion data with tract-based spatial statistics. Nat Protoc 2007; 2(3): 499-503.
Sokolov AA, Erb M, Gharabaghi A, Grodd W, Tatagiba MS, Pavlova MA. Biological motion processing: the left cerebellum communicates with the right superior temporal sulcus. Neuroimage 2012; 59(3): 2824-30.
Sokolov AA, Erb M, Grodd W, Pavlova MA. Structural loop between the cerebellum and the superior temporal sulcus: evidence from diffusion tensor imaging. Cereb Cortex 2014; 24(3): 626-32.
Song SK, Sun SW, Ju WK, Lin SJ, Cross AH, Neufeld AH. Diffusion tensor imaging detects and differentiates axon and myelin degeneration in mouse optic nerve after retinal ischemia. Neuroimage 2003; 20(3): 1714-22.
Stoodley CJ. The cerebellum and cognition: evidence from functional imaging studies. Cerebellum 2012; 11(2): 352-65.
Stoodley CJ, Schmahmann JD. Functional topography in the human cerebellum: a meta-analysis of neuroimaging studies. Neuroimage 2009; 44(2): 489-501.
Stoodley CJ, Schmahmann JD. Evidence for topographic organization in the cerebellum of motor control versus cognitive and affective processing. Cortex 2010; 46(7): 831-44.
Strick PL, Dum RP, Fiez JA. Cerebellum and nonmotor function. Annu Rev Neurosci 2009; 32: 413-34.

Stricker NH, Schweinsburg BC, Delano-Wood L, Wierenga CE, Bangen KJ, Haaland KY*, et al.* Decreased white matter integrity in late-myelinating fiber pathways in Alzheimer's disease supports retrogenesis. Neuroimage 2009; 45(1): 10-6.
Sugihara S, Kinoshita T, Matsusue E, Fujii S, Ogawa T. Usefulness of diffusion tensor imaging of white matter in Alzheimer disease and vascular dementia. Acta Radiol 2004; 45(6): 658-63.
Suri S, Topiwala A, Mackay CE, Ebmeier KP, Filippini N. Using structural and diffusion magnetic resonance imaging to differentiate the dementias. Curr Neurol Neurosci Rep 2014; 14(9): 475.
Szirmai I, Vastagh I, Szombathelyi E, Kamondi A. Strategic infarcts of the thalamus in vascular dementia. J Neurol Sci 2002; 203-204: 91-7.
Takahashi S, Yonezawa H, Takahashi J, Kudo M, Inoue T, Tohgi H. Selective reduction of diffusion anisotropy in white matter of Alzheimer disease brains measured by 3.0 Tesla magnetic resonance imaging. Neuroscience letters 2002; 332(1): 45-8.
Teipel SJ, Grothe MJ, Filippi M, Fellgiebel A, Dyrba M, Frisoni GB*, et al.* Fractional anisotropy changes in Alzheimer's disease depend on the underlying fiber tract architecture: a multiparametric DTI study using joint independent component analysis. J Alzheimers Dis 2014; 41(1): 69-83.
Tournier JD, Calamante F, Connelly A. Robust determination of the fibre orientation distribution in diffusion MRI: non-negativity constrained super-resolved spherical deconvolution. Neuroimage 2007; 35(4): 1459-72.
Tournier JD, Calamante F, Connelly A. MRtrix: diffusion tractography in crossing fiber regions. International Journal of Imaging Systems and Technology 2012; 22(1): 53-66.
Tournier JD, Mori S, Leemans A. Diffusion tensor imaging and beyond. Magn Reson Med 2011; 65(6): 1532-56.
Tsuchiya K, Fujikawa A, Suzuki Y. Diffusion tractography of the cervical spinal cord by using parallel imaging. American journal of neuroradiology 2005; 26(2): 398-400.
Tsuchiya K, Katase S, Fujikawa A, Hachiya J, Kanazawa H, Yodo K. Diffusion-weighted MRI of the cervical spinal cord using a single-shot fast spin-echo technique: findings in normal subjects and in myelomalacia. Neuroradiology 2003; 45(2): 90-4.
Uğurbil K, Xu J, Auerbach EJ, Moeller S, Vu AT, Duarte-Carvajalino JM*, et al.* Pushing spatial and temporal resolution for functional and diffusion MRI in the Human Connectome Project. Neuroimage 2013; 80: 80-104.
van Baarsen KM, Kleinnijenhuis M, Jbabdi S, Sotiropoulos SN, Grotenhuis JA, van Cappellen van Walsum AM. A probabilistic atlas of the cerebellar white matter. Neuroimage 2016; 124(Pt A): 724-32.
van Bruggen T, Stieltjes B, Thomann PA, Parzer P, Meinzer HP, Fritzsche KH. Do Alzheimer-specific microstructural changes in mild cognitive impairment predict conversion? Psychiatry Res 2012; 203(2-3): 184-93.
Vann SD, Aggleton JP, Maguire EA. What does the retrosplenial cortex do? Nat Rev Neurosci 2009; 10(11): 792-802.
Voogd J. The human cerebellum. J Chem Neuroanat 2003; 26(4): 243-52.
Wang K, Liang M, Wang L, Tian L, Zhang X, Li K*, et al.* Altered functional connectivity in early Alzheimer's disease: a resting-state fMRI study. Hum Brain Mapp 2007; 28(10): 967-78.
Watson TC, Becker N, Apps R, Jones MW. Back to front: cerebellar connections and interactions with the prefrontal cortex. Front Syst Neurosci 2014; 8: 4.
Wedeen VJ, Wang RP, Schmahmann JD, Benner T, Tseng WY, Dai G*, et al.* Diffusion spectrum magnetic resonance imaging (DSI) tractography of crossing fibers. Neuroimage 2008; 41(4): 1267-77.

Wheeler-Kingshott CA, Parker GJ, Symms MR, Hickman SJ, Tofts PS, Miller DH*, et al.* ADC mapping of the human optic nerve: Increased resolution, coverage, and reliability with CSF-suppressed ZOOM-EPI. Magnetic resonance in medicine 2002; 47(1): 24-31.
Wilm B, Gamper U, Henning A, Pruessmann K, Kollias S, Boesiger P. Diffusion-weighted imaging of the entire spinal cord. NMR in biomedicine 2009; 22(2): 174-81.
Wilm B, Svensson J, Henning A, Pruessmann K, Boesiger P, Kollias S. Reduced field-of-view MRI using outer volume suppression for spinal cord diffusion imaging. Magnetic resonance in medicine 2007; 57(3): 625-30.
Winkler AM, Ridgway GR, Webster MA, Smith SM, Nichols TE. Permutation inference for the general linear model. Neuroimage 2014; 92: 381-97.
Zarei M, Damoiseaux JS, Morgese C, Beckmann CF, Smith SM, Matthews PM*, et al.* Regional white matter integrity differentiates between vascular dementia and Alzheimer disease. Stroke 2009; 40(3): 773-9.
Zarei M, Patenaude B, Damoiseaux J, Morgese C, Smith S, Matthews PM*, et al.* Combining shape and connectivity analysis: an MRI study of thalamic degeneration in Alzheimer's disease. Neuroimage 2010; 49(1): 1-8.
Zhang Y, Brady M, Smith S. Segmentation of brain MR images through a hidden Markov random field model and the expectation-maximization algorithm. IEEE Trans Med Imaging 2001; 20(1): 45-57.